



Seventh Quarterly Report Phase II April 1, 2011

Prepared by
Prof. Nariman Farvardin
Principal Investigator and EERC Project Director

Prof. Bala Balachandran, Acting Chair
EERC Project Deputy Director

Dr. Azar Nazeri
EERC Research Manager



THE UNIVERSITY OF MARYLAND AND THE PETROLEUM INSTITUTE OF ABU DHABI, UAE

EERC Key Contributors

University of Maryland – College Park, MD, USA

Shapour Azarm
Balakumar Balachandran
Avram Bar-Cohen
David Bigio
Hugh A. Bruck
Kyu Young Choi
Nikil Chopra
Avram Bar-Cohen
Serguei Dessiatoun
Ashwani K. Gupta
Satyandra K. Gupta
Yunho Hwang
P.K. Kannan
Mohammad Modarres
Michael Ohadi
Reinhard Radermacher
Amir Shooshtari

Petroleum Institute – Abu Dhabi, UAE

Youssef Abdel-Majid
Ahmed Al Shoaibi
Saleh Al Hashimi
Ebrahim Al-Hajri, Returning ADNOC Scholar
Ali Almansoori
Mohamed Alshehhi
Sai Cheong Fok
Afshin Goharzadeh
Hamad Karki
Isoroku Kubo
Peter Rodgers
Abdennour Seibi

Table of Contents

EERC Key Contributors	2
Table of Contents	3
Executive Summary	5
Introduction	8
Individual Project Reports	19
Thrust 1: Energy Recovery and Conversion	20
Sulfur Recovery from Gas Stream using Flameless and Flame Combustion Reactor A.K. Gupta, A. Al Shoaibi	21
Separate Sensible and Latent Cooling with Solar Energy R. Radermacher, Y. Hwang, I. Kubo	35
Waste Heat Utilization in the Petroleum Industry R. Radermacher, Y. Hwang, S. Al Hashimi, P. Rodgers	42
Thrust 2: Energy-Efficient Transport Processes	51
Multidisciplinary Design and Characterization of Polymer Composite Seawater Heat Exchanger Module P. Rodgers, A. Bar-Cohen, S.K. Gupta, D. Bigio, H.A. Bruck	52
Microchannel-Based Absorber/Stripper and Electrostatic Precipitators for CO ₂ Separation Processes S. Dessiatoun, A. Shooshtari, M. Ohadi, A. Goharzadeh	72
Microreactors for Oil and Gas Processes Using Microchannel Technologies S. Dessiatoun, A. Shooshtari, K.Y. Choi, M. Ohadi, A. Goharzadeh	91
Thrust 3: Energy System Management	107
Integration of Engineering and Business Decisions for Robust Optimization of Petrochemical Systems S. Azarm, P.K. Kannan, A. Almansoori, S. Al Hashimi	108
Dynamics and Control of Drill Strings B. Balachandran, H. Karki, Y. Abdelmagid, S.C. Fok	120

Studies on Mobile Sensor Platforms B. Balachandran, N. Chopra, H. Karki	136
Development of a Probabilistic Model for Degradation Effects of Corrosion-Fatigue Cracking in Oil and Gas Pipelines M. Modarres, A. Seibi	146

Executive Summary

The following is a summary of the major project activities that have taken place over the completed quarter. For more detail, see the individual reports in the last section of this report.

Thrust 1: Energy Recovery and Conversion

Sulfur Recovery from Gas Stream using Flameless and Flame Combustion Reactor

A.K. Gupta, A. Al Shoaibi

- Examined hydrogen sulfide combustion in methane/air flame in a plug flow reactor at different equivalence ratios.
- Prepared laser-induced breakdown spectroscopy (LIBS) setup for sulfur deposits analysis as well as larger sulfur samples to be used in the analysis.
- Submitted two technical papers to The Journal of Applied Energy. Meanwhile, a rebuttal of a previously submitted journal paper, in 2009, was prepared. All three papers are accepted for publication.

Separate Sensible and Latent Cooling with Solar Energy

R. Radermacher, Y. Hwang, I. Kubo

- Calibrated the refrigerant and the water mass flow meters.
- Finished the hot water loop.
- Connected the instrumentation to the data acquisition system.
- Created a LabView program for the experiment.
- Wired the experimental power supply side and installed it in the power cabinet.

Waste Heat Utilization in the Petroleum Industry

R. Radermacher, Y. Hwang, S. Al Hashimi, P. Rodgers

- Modeled the open CO₂ liquefaction cycle.
- Verified the CO₂ liquefaction cycle model with EES.
- Modeled heat pump cycle with different refrigerants.
- Optimized two configurations of gas turbine combined cycle with double-pressure steam cycle.
- Optimized two configurations of gas turbine triple combined cycle with double-pressure steam cycle and absorption chillers.

Thrust 2: Energy-Efficient Transport Process Projects

Multidisciplinary Design and Characterization of Polymer Composite Seawater Heat Exchanger Module

P. Rodgers, A. Bar-Cohen, S.K. Gupta, D. Bigio, H.A. Bruck

- Revisited thermal anisotropy of polymer composite fins induced by fiber orientation.
- Developed and used thermomechanical finite element model to assess thermal and structural performance of polymer composite heat exchanger, and assessed feasibility of replacing metallic heat exchangers at the Das Island liquefied natural gas facility with polymer composite heat exchangers.
- Developed accurate mold-filling metamodel using advanced datapoint selection methodology.
- Developed new image processing methodology for identifying fibers in microscope images of sample heat exchanger geometry.
- Developed a technique for characterizing mixing of polymer composites in a Twin Screw Extruder.
- Submitted abstract and draft paper entitled “An Integrated Approach to Design of Enhanced Polymer Heat Exchangers” to DETC Conference to be held on August 29-31 2011 in Washington, DC.
- Submitted abstract entitled “Polymer Heat Exchangers – An Enabling Technology for Water and Energy Savings” to IMECE Conference to be held on November 11-17 2011 in Denver, Colorado.
- Submitted abstract for a technical paper entitled “Modeling and Validation of Prototype Thermally Enhanced Polymer Heat Exchanger” to the 2011 International Mechanical Engineering Congress & Exposition in Denver, Colorado. Paper has been accepted.

Microchannel-Based Absorber/Stripper and Electrostatic Precipitators for CO₂ Separation Processes

S. Dessiatoun, A. Shooshtari, M. Ohadi, A. Goharzadeh

- Improved experimental setup.
- Collected new set of data.
- Improved model.
- Experimental study of absorption of CO₂ in a single microchannel reactor.

Microreactors for Oil and Gas Processes Using Microchannel Technologies

S. Dessiatoun, A. Shooshtari, Kyu Young Choi, M. Ohadi, A. Goharzadeh, E. Al-Hairi

- Designed tubular polymerization microreactor.
- Conducted detailed theoretical modeling of polymerization in microreactor.

Thrust 3: Energy System Management

Integration of Engineering and Business Decisions for Robust Optimization of Petrochemical Systems

S. Azarm, P.K. Kannan, A. Almansoori, S. Al Hashimi

- Developed and under implementation is a new Kriging meta-model assisted optimization approach for Multi-Objective Robust Optimization (MORO) with both reducible and irreducible interval uncertainty.
- Proposed a decision support model with a dashboard-like interface for a notional refinery problem that can be used for adjusting/predicting critical parameters in a simulation model.
- Revised/implementing the HYSYS simulation model of an o-xylene oxidation process for producing phthalic anhydridex.
- Continued progress on joint publications.

Dynamics and Control of Drill Strings

B. Balachandran, H. Karki, Y. Abdelmagid

- Identified rotor movements and characteristic behaviors.
- Developed a distributed-parameter model that may be useful for describing horizontal drill string dynamics.
- Compared model to experimental data from the vertical string experiment.

Studies on Mobile Sensor Platforms

B. Balachandran, N. Chopra, H. Karki, S.C. Fok

- Completed analytical and numerical results obtained for the decentralized SLAM algorithm results presented in the previous report.
- Completed experimental setup.

Development of a Probabilistic Model for Degradation Effects of Corrosion-Fatigue Cracking in Oil and Gas Pipelines

M. Modarres, A. Seibi

- Compared empirical model with literature (application of Akaike relation).
- Applied model uncertainty approach (Bayesian approach) to compare the models with the experimental strain data.
- Performed creep experiments on Al 7075-T6 in support of corrosion and creep model development.

Introduction

The seventh quarter of the EERC has been particularly fruitful in terms of faculty visits and workshops between PI and UMD to share best practices for education and faculty development. Details of these visits are given below.

UMD-PI Visits

Dr. Nader Vahdati and Dr. Ebrahim Al Hajri Visit to UMD

Dr. Nader Vahdati, Associate Professor and Associate Chair of the Mechanical Engineering Department at the Petroleum Institute, and Dr. Ebrahim Al Hajri, Assistant Professor at PI, visited the University of Maryland January 25-28, 2011. This visit was aimed at interacting with EERC faculty and students, engaging with faculty conducting research in their respective fields of expertise and becoming familiar with the Society of Automotive Engineering (SAE) Mini-Baja activities at UMD.

During his visit Dr. Vahdati visited Dr. Balachandran and Dr. Nikhil Chopra and their laboratories and had an extensive tour and meeting with the graduate students in both labs. He also met with a few other EERC faculty members. Unfortunately, a larger gathering for the whole EERC group scheduled to meet with Dr. Vahdati and his seminar on his research interests on Thursday, January 25, was canceled due to inclement weather and the school closing.

One important goal of Dr. Vahdati and Dr. Al Hajri for this trip was to talk to Dr. Greg Schultz and visit the SAE Mini-Baja Lab. Dr. Vahdati will be spearheading an SAE Mini-Baja initiative at PI. Dr. Greg Schultz, who is heading the SAE efforts at UMD, gave a comprehensive presentation to both on this effort at UMD and arranged for a tour of the SAE lab. Dr. Vahdati and Dr. Schultz will be working closely to establish a similar program at PI.



Dr. Greg Schultz gives Dr. Vahdati a tour of the SAE lab and racing cars.

The University of Maryland participates in the SAE International Student Design Series, in which UMD's SAE chapter (known as Terps Racing) designs, fabricates, and competes a recreational off-road vehicle each year to enhance their engineering education. The Petroleum Institute intends to create a similar student program, and the University of Maryland's Department of Mechanical Engineering plans to transfer the 2007-built vehicle to the PI to foster their new program.

Mr. Amarildo DeMata Visit to PI

Mr. Amarildo DeMata, the Graduate Study Coordinator of the Mechanical Engineering Department, spent two weeks of the winter break at the Petroleum Institute to exchange experiences between his office and the Office of Graduate Studies at PI. This assignment was part of the collaborative activities between the two institutions to transfer best practices from UMD to PI in research, education and administrative matters.



From left, Dr. Ainane, Mr. DeMata, Dr. Ecomomu, Dr. Kim, and Mr. Paz.

During his assignment, Mr. DeMata worked directly with the Associate Provost of Graduate Studies at PI, Dr. Ioannis Economu, and Dr. Kim and Mr. Della Paz at the Graduate Studies Office. Mr. DeMata was able to review the PI policies and procedures pertaining to recruiting, admission, and orientation of new graduate students and give useful feedback for improving these processes. He also worked on standardizing letters and contracts for new research graduates and teaching assistants. Additionally, he recommended ways of improving the social activities and events for all students and conducted a quick opinion survey of the students regarding the graduate program at PI.

Mr. DeMata and Dr. Sami Ainane, Director of Student Affairs at PI and another assignee from UMD to PI, also worked on a proposal for a BS/MS program aiming to retain the PI's best undergraduate students for an MS program. This idea is based on a similar and successful program created more than ten years ago at the ME department at the University of Maryland.

Sami Ainane Visit to UMD

Dr. Sami Ainane, on assignment from UMD to the PI, visited his home campus on March 18, 2011 to promote the first study abroad program at the Petroleum Institute (PI) in Abu Dhabi this summer. Engineering classes are offered at PI in Chemical Engineering, Electrical Engineering, Materials Science, and Mechanical Engineering, and courses will be taught in English. This

program offers an exciting opportunity for UMD undergraduate/graduate students to experience a different culture and collaborate with their international counterparts. The information session was well attended and many questions from students about the program and the overall life and culture in Abu Dhabi were answered by Dr. Ainane.



Dr. Sami Ainane presenting the Abu Dhabi study abroad program to UMD students.

Design Workshop at PI

Dr. Linda Schmidt of the University of Maryland visited PI March 20–22, as part of the Memorandum of Understanding’s exchange of best practices. During her visit she conducted a series of workshops focused on Enhancing and Assessing Design Project Teamwork, Teaching Sketching, and Scoping Quality Design Projects. She also consulted with programs and faculty regarding meeting ABET Design Experience requirements. Dr. Schmidt was a guest lecturer in several sophomore level design (STEPS) classrooms, where she expanded on current approaches to brainstorming ideas and sketching by facilitating activities with students. Dr. Schmidt facilitated three workshops, one focused on teaching sketching, a second on enhancing and assessing teamwork in design classes, and a third on scoping out good projects. The workshops were well received and useful to the faculty and administrators who attended. An abstract for each workshop and further details are given below.

“Sketching to Improve Design” Presented Sunday, March 20

Sketching is a both physical and mental process. A well-used description of sketching from French is that a sketch is a designer’s “conversation with themselves.” Every engineer appreciates the value of a sketch to describe a physical object to a colleague or to record ideas when developing design options. However, most of today’s engineering students prefer the use of CAD programs to pencil and paper sketching. Many have never been trained in drawing skills and are reluctant to try to draw by hand. These students are not aware of the value of sketching to improve creativity and bring other benefits to the design process.

What happens physically during sketching is easy to see and understand. However, the mental (or cognitive) activities during sketching are impossible to observe in real time and challenging to record in any fashion. The cognitive processes involved in sketching have been explored by many researchers in various concentration areas, including engineering, architecture, art, education, and psychology. Research done at the University of Maryland demonstrates that students can be easily influenced to improve the content of their sketches regardless of their drawing skills. The capstone design course in Mechanical Engineering at Maryland has incorporated increased use of sketching with positive results. These developments were presented during this workshop.

This workshop was attended by 22 PI faculty members.

“Enhancing and Assessing Teamwork”
Presented Monday, March 21

The project team has become a well-established primary learning environment for engineering students. Engineering education accreditation reflects this in their required student learning outcome: the ability to function on multidisciplinary teams. However, the field of engineering education appears to have an ambivalent attitude toward this pedagogical approach. Many students and faculty dread team projects for reasons that include team conflicts, including how to handle “slackers,” logistical problems, and the difficulty of evaluating the work of individuals when the team grade is based on a completed project.

This workshop discussed and shared practices teams and team operation guidelines; establishing effective peer evaluation regimes; and assessing individual learning objectives. Many of these strategies were developed during research done under a National Science Foundation funded project called BESTEAMS: Building Engineering Student Team Effectiveness and Management Systems (1996 -2005). BESTEAMS conducted scholarly research to model the engineering student-project team environment and develop curriculum-enhancing standardized team skills training modules for delivery by engineering educators. Under the grant, BESTEAMS strategies were used to train over 4000 engineering students at a variety of courses and institutions. The workshop presented the strategy for enhancing team performance and introduced the BESTEAMS training process.

This session was attended by 11 PI faculty members.

The material presented, according to Brian Bielenberg of PI, “has already made an impact as several of the participants have shared the ideas presented with others in their department...the discussions begun in this session have spread, one of the primary intentions of having such sessions.”

“Capstone Design Projects: What Works for Students, Faculty & ABET”
Presented Tuesday, March 22

Design projects are a natural vehicle for demonstrating the acquisition of engineering knowledge and the development of engineering skills. No design course is as comprehensive and challenging for students as the capstone design experience. Therefore, it is not surprising that curriculum managers look to the capstone design course to provide evidence of the achievement of a significant number of the ABET Student Outcomes. ABET assessment is often associated with ten student outcomes that describe the results of an engineering education. The outcomes list begins with the broad outcome of "an ability to apply knowledge of mathematics, science, and engineering." Other outcomes are specific to design activities, functioning on teams, and forward-

looking, such as "a recognition of the need for, and an ability to engage in life-long learning." Design is such an integral part of engineering practice that a capstone design course will require students to use or develop all of the skills described in the learning outcomes.

The success of the engineering team capstone design project experience relies in a large part on the design project selected for the student team. Even when student teams are allowed to propose their own projects, course faculty must thoughtfully consider the appropriateness. Primary emphasis is given to the educational challenge of the proposed project and the fit the design activities have with the team's discipline. The increasing dependence of a department on capstone design for accreditation evidence adds another level of complexity to the project approval process.

This workshop was attended by 17 PI faculty members representing all of PI's engineering programs.

Strategies for managing these challenges in the identification and development of capstone design projects were discussed. The session consisted of lively discussion on identifying appropriate capstone projects, and how to assess Program/ABET outcomes within a capstone course. Dr. Schmidt presented the approach used by Maryland's Mechanical Engineering program, and participants commented on the usefulness of comparing a variety of approaches, helping to identify strengths in our own programs along with generating ideas of how they can be further improved. These discussions were extended throughout the visit during focus group meetings that Dr. Schmidt held with senior design faculty from each program.

Senior Design and ABET Faculty Consultations

For one-and-a-half hours each morning, Dr. Schmidt met with Senior Design faculty from the PI engineering departments to discuss approaches to the design experience, with particular emphasis on how to identify projects that satisfy ABET expectations and how to present senior design during ABET reporting and evaluation. These meetings involved ten PI senior design faculty: three from Mechanical Engineering, three from Petroleum Engineering, and two each from Chemical and Electrical Engineering. The value of these interactions is best summed up by the comments of one of the involved faculty, who, when asked, "Overall, was the session worthwhile?" enthusiastically replied, "Absolutely. I don't remember a similar meeting in the past from other schools on design and how others offer the course elsewhere. It was great to share ideas."

While participants provided overall positive feedback, many also recommended that future exchanges of best practices include more specific examples. For instance, one participant commented, "I would have liked to see some more specific examples and projects. A sample of good, bad and ugly such that we can set benchmarks for our students." Another suggested that it would have been helpful if "she share[d] with us some of the material she covers at Maryland and the forms she uses to evaluate the different requirements for the course (rubrics)." (Note: this was actually done in the third workshop). Overall, the sessions received extremely positive feedback, and PI faculty look forward to further exchanges of knowledge and experiences focused on specific practices and material.

Guest Lectures in STEPS Courses

In addition to the morning meetings with senior design faculty and noon seminars, Dr. Schmidt also served as a guest instructor in four STEPS I courses. STEPS I is a sophomore level multidisciplinary cornerstone design course at the PI. It is PI students' first formal exposure to engineering practice and the engineering design process. Dr. Schmidt took each of the four classes through a connected brainstorming and sketching activity that helped to reinforce the ideas behind, and the need for, structured brainstorming in the design process. Dr. Schmidt had

the students actively engaged in the brainstorming process. The modeling of the activity, while targeted at the students, had the additional benefit of providing PI faculty with new ideas: “Seeing another teacher working is always useful and allows us to reflect on our own practice.” Another added, “The brainstorming session using ‘sticky notes’ (‘Post-it notes’) was very interesting and seems very effective at extracting lots of ideas from the heads of all team members. I will encourage the use of this method in the future because this brainstorming process encourages students to share all their ideas openly and in an interactive and fun way.”

Summary

Overall, all three aspects of Dr. Schmidt’s visit received extremely positive feedback. PI faculty stated that they benefited from hearing about best practices at another institution, both in general terms and through sharing of specific materials and experiences. All encourage a continuation of these types of exchanges. The feedback from participants also indicates some general ideas regarding future activities.

Recommendations

- Future exchanges of this type should be encouraged.
- Exchanges should be two-way.
- Future exchanges should include specific examples of materials and activities.
- People involved in the exchange should be informed about the PI context before coming to PI.



Dr. Schmidt presents ideas regarding designing projects for capstone courses.



STEPS students expanding their design space through an extended brainstorming activity introduced by Dr. Schmidt.



Dr. Schmidt meets with PI STEPS faculty Dr. Sam Cubero and Dr. Jaby Mohammed.



Dr. Schmidt and Dr. Peter Rodgers proudly displaying the results of their thinking about Capstone Design issues

Paige Smith Visit to PI

Dr. Paige Smith, the Director of the Women in Engineering program (WIE) at UMD visited the Arzanah campus March 20-22, 2011 and conducted a three-day workshop. The focus of Dr. Smith's activities was twofold. First, she worked with AUP, WISE and Student Affairs representatives with regard to community outreach and recruiting initiatives. Her first morning session addressed these aspects from a broad perspective. The second afternoon session focused more on recruiting students from "minority" backgrounds, which in the PI context is interpreted as Emiratis, as they make up a small portion of the overall population (~15 %) and often have had fewer opportunities to develop their academic skills (they are, however, the majority of the PI's student population). She had a lunch meeting with the Recruiting Task Force Committee, presented a workshop on "Planning Strategies for Student Recruitment" (with Recruiting Task Force members), a workshop on "Student Recruitment and Retention" (with WISE students and WISE administration), and a workshop on how to plan, organize and implement summer camps for high school students focused on math, science and English skills (with the AUP Task Force).

The second component of Dr. Smith's contributions was in the area of faculty mentoring. She presented a workshop on establishing faculty mentoring programs at an institutional and departmental level. Dr. Youssef Abdel-Majid, the Dean of the Engineering School at PI, contributed to the workshop by discussing PI's efforts on this front; participants were the CELT Director, Dr. Brian Bielenberg, chairs of the engineering departments, and interested faculty. Dr. Smith also met with faculty to discuss preparing for promotion and supporting junior faculty planning to apply for promotion in Fall 2011 or 2012, who are in the process of putting together a promotion file.

The workshops conducted by Dr. Paige Smith on recruiting, mentoring and summer programs were very much appreciated by all the participants at PI.

The PI management communicated their desire for further involvement, possibly for an extended period of time, to further benefit from Dr. Smith's expertise. She will be invited to spend one or more weeks at the PI to provide further guidance to relevant programs.



Dr. Smith at the workshop with the WISE students.



Dr. Nadia al Hassani and Dr. Smith.



Dr. Smith and Dr. Nazari meeting with women faculty at PI, the Director of Student Affairs and the Director of AUP.

Second Annual Journey of Discovery

The second Journey of Discovery, the annual Spring Break visit of the women students from PI, Arzanah campus, along with their Director, took place March 25 - April 1. The trip was co-organized by the WISE Program Director and Arzanah Campus Director Dr. Nadia Alhasani and Dr. Azar Nazeri, Research Manager of the University of Maryland's Energy Education and Research Collaboration (EERC). One of the objectives of the trip was to provide an opportunity for women PI students to visit engineering programs at a partner institution, expose them to cutting-edge research and technology, and inspire and enhance their commitment to science and technology.

The major component of the itinerary was the visit to the University of Maryland, College Park campus, touring state-of-the-art research laboratories and attending presentations and workshops mostly conducted by female professors at University of Maryland. Among the laboratories visited were two chemical engineering laboratories, Dr. Raghavan's lab and Dr. Anisimov's light scattering lab, and the ME Microelectronics Interconnects Laboratory, Micro-Robotics Laboratory, Virtual Reality Laboratory, Nano-Fabrication Laboratory and the University Nuclear Reactor. The party also attended lectures given by leading scientists in the field of MEMS and nano-fabrication engineering.

The Arzanah students were also invited to attend a capstone design lab where the student groups were working on their senior projects.

The busy itinerary did allow for visits to Washington DC, Georgetown, Baltimore, and old-town Alexandria. Included in the trip were opportunities for students to visit several renowned museums, such as the Natural History Museum, the National Air and Space Museum, and the National Art Gallery – East Wing, and Air & Space Museum.

The professors giving tours to Arzanah students described as “curious, inquisitive and always with the best questions.”

Aside from supervising the trip, Dr. Nadia Al Hassani held many meetings during this trip with faculty and UMD management. She met with Dr. Balachandran, the Acting Chair of the Mechanical Engineering department; Dr. Smith, the Director of the WIE program; Dr. Nazeri, the

Research Manager of the EERC; and Dr. Al Skeikhly, the Director of the Nuclear Reactor at UMD. She also had a follow-up meeting on the “PI Strategic Plan” with Dr. Ali Mosleh, Professor of Mechanical Engineering, Dr. Balachandran and Dr. Nazeri.



Students visiting Prof. Amr Baz’s laboratory.



Individual Project Reports



Thrust 1
Energy Recovery and Conversion

Sulfur Recovery from Gas Stream using Flameless and Flame Combustion Reactor

UMD Investigators: Ashwani K. Gupta
GRA: Hatem Selim
PI Investigators: Ahmed Al Shoaibi
Start Date: October 2006

1. Objectives / Abstract

The main objective is to obtain fundamental information on thermal process of sulfur recovery from sour gas by conventional flame combustion as well as flameless combustion, using numerical and experimental studies. Our ultimate goal is to determine optimal operating conditions for enhanced sulfur conversion. Therefore, an experimental study of the flameless combustion processes of the Claus furnace is proposed so that the results can be used in the normal flame process for determining improved performance. In this study we will explore different operating conditions and perform in flame and exhaust gas analyses of both flame and flameless modes of reactor operation in order to gain a better understanding of the process with the goal to attain enhanced sulfur capture efficiency.

Specific objectives are to provide:

- A comprehensive literature review of the existing flame combustion process for sulfur removal with special reference to sulfur chemistry
- Near isothermal reactor conditions and how such conditions assist in the enhanced sulfur recovery process
- CFD simulation of the flame and flameless combustion in the furnace.
- Determination of the chemical kinetics and the major reaction pathways to seek high performance
- Design of a reactor for experimental verification of the numerical results
- Measurements and characterization of the combustion furnace under various conditions, including the conditions that utilize high temperature air combustion principles for flameless combustion
- Experiments with different sulfur content gas streams using the flame and flameless combustion furnace modes of operation.
- Installation of the appropriate diagnostics for quantification of stable and intermediate sulfur compounds in the process and exit stream
- Flow, thermal and chemical speciation characteristics of the reactor
- Product gas stream characteristics and evaluation of sulfur recovery and performance in the process

2. Deliverables

- Examination of hydrogen sulfide combustion in methane/air flame in a plug flow reactor at different equivalence ratios.

- Preparation for laser-induced breakdown spectroscopy (LIBS) setup for sulfur deposits analysis as well as the preparation of larger sulfur samples to be used in the analysis.
- Submission of two technical papers to The Journal of Applied Energy. Meanwhile, a rebuttal of a previously submitted journal paper, in 2009, was prepared. All three papers are accepted for publication.

3. Executive Summary

During the reported quarter, progress continued with major focus on the experimental part of the project. Change in the reactants injection configuration of the burner enabled us to examine H₂S combustion in CH₄/air flame at different equivalence ratios in a plug flow reactor. The reactants are premixed upstream of the reactor. Three equivalence ratios, ranging from rich conditions, $\Phi=3.0$ (Claus conditions), stoichiometric conditions, $\Phi=1.0$, and lean conditions, $\Phi=0.5$, were used for the examination. Gas sampling was conducted axially along the reactor at three radial locations. The results revealed the formation of higher hydrocarbons under Claus conditions. In addition, carbon disulfide was formed under Claus and stoichiometric conditions.

Laser induced breakdown spectroscopy (LIBS) setup was put together to be used for solid sulfur samples analysis. This setup will be used to analyze sulfur deposited on the reactor walls or in the gas sampling line. Large sulfur samples were prepared using H₂S/O₂ flame in order to facilitate preliminary tests of the setup.

Two technical papers were written and submitted to The Journal of Applied Energy. Both papers have been accepted. In addition, a rebuttal was prepared for another paper, submitted in 2009. That paper has been accepted for publication as well. All three papers are now available online.

4. Progress

4.1 Effect of H₂S/O₂ Equivalence Ratio on Combustion Products in CH₄/air flames in a plug flow reactor (PFR)

Experiments were conducted to investigate the combustion of hydrogen sulfide in methane/air flames at different equivalence ratios in a quasi-plug flow reactor. The reactor configuration has been manipulated in order to assure good mixing conditions for all reactants. The geometry shown in Figure 1 allows simulations of of practical importance and significance. Under certain conditions the burner configuration allows us to simulate plug flow reactor conditions.

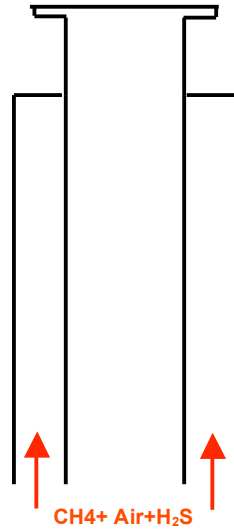


Figure 1. Burner configuration used to achieve PFR conditions.

Mean temperature measurement

Figure 2 shows the spatial distribution of reactor mean temperature under Claus conditions ($\Phi=3.0$). The reactor was assumed to be symmetrical so that mean temperature measurements were carried out for only one half section of the reactor. Dimensionless axial (W) and radial (R) distances were used to show the trends for temperature and combustion generated species in the flames. Jet diameter was used to transform the linear distances to dimensionless parameters, i.e., W = axial distance/ D_{jet} , and R = radial distance/ D_{jet} .

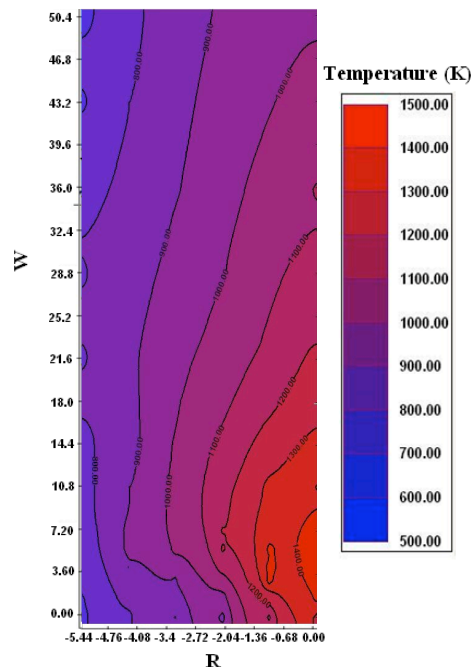


Figure 2. Spatial temperature distribution of the reactor under Claus conditions.

Experimental procedure

- Adjust methane/air equivalence ratio to slightly fuel-lean conditions.
- Calculate the excess oxygen flow rate and adjust the required H_2S flow rate accordingly to achieve the desired equivalence ratio.

- Take gas samples at different axial locations, normally at 0, 0.25, 0.5, 0.75, 1.0, 1.5, 2.0, 2.5, 3.0, 4.0, 5.0, 6.0, 7.0, and 7.5 inches along the centerline of the reactor.
- Change the radial location of the probe and repeat step 3.

Experimental test matrix

Equivalence ratio (Φ)	Air flow rate (lit/min)	CH ₄ flow rate (lit/min)	Excess oxygen (cm ³ /min)	H ₂ S flow rate (cm ³ /min)
$\Phi=3.0$	9.7	0.97	55	110
$\Phi=1.0$	9.5	0.975	90	60
$\Phi=0.5$	9.7	0.95	144	48

All experiments were repeated at least three times in order to assure repeatability of the data. The presented results are with the average values for each run.

Combustion products analysis

This study started with the examination of H₂S combustion in CH₄/air flames under Claus conditions according to the conditions given above. Figures 3, 4, and 5 describe the distribution of hydrogen mole fraction at different equivalence ratios along the reactor at three radial locations. At any equivalence ratio along the reactor centerline a constant decrease in H₂ mole fraction was observed. However, at radially outward locations, hydrogen mole fraction tended to peak to a maximum followed by a monotonic decrease. The peak of H₂ mole fraction is attributed to the configuration of the burner, which dictates that the reactants flow will spread radially outward. On the other hand, at $\Phi=1.0$ and $\Phi=0.5$, the H₂ peak at R= 1.77 exceeds the corresponding value of H₂ mole fraction at R=0.0. This is attributed to the availability of higher amounts of oxygen at R=1.77. This is translated to higher oxidation rates of hydrogen, which leads to lower amounts of hydrogen presented in the flow recirculation zone downstream of the bluff body. In addition, the lower amount of H₂S decreases the prohibiting oxidation effect¹ of hydrogen in the reaction pool at these stoichiometric and fuel lean equivalence ratios (i.e., at $\Phi=1.0$ and $\Phi=0.5$).

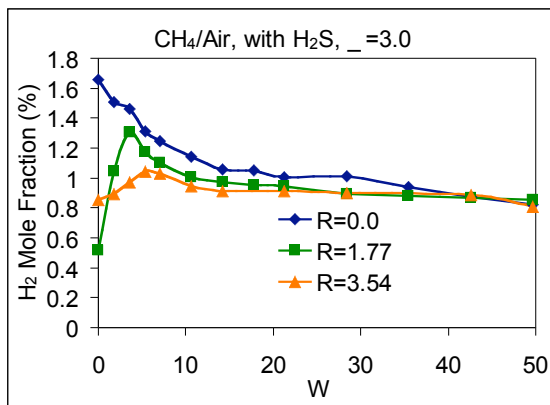


Figure 3. Hydrogen mole fraction. Flame conditions: CH₄/air with H₂S. $\Phi = 3.0$.

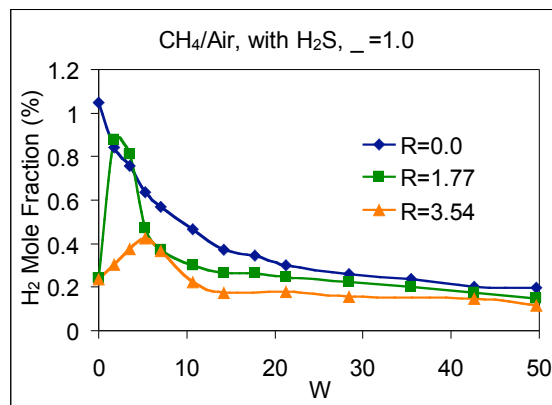


Figure 4. Hydrogen mole fraction. Flame conditions: CH₄/air with H₂S. $\Phi = 1.0$.

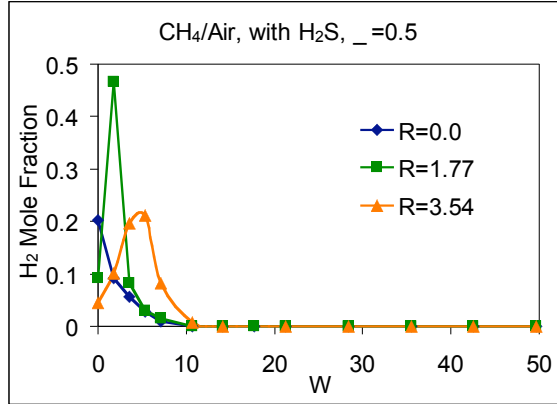


Figure 5. Hydrogen mole fraction. Flame conditions: CH₄/air with H₂S, $\Phi = 0.5$.

Figures 6, 7, and 8 represent the distribution of carbon monoxide mole fraction at different equivalence ratios along the reactor at three radial locations. The carbon monoxide decreases monotonically along the centerline of the reactor. However, at any axial location as one moves radially outwards, the carbon monoxide peaks to a maximum value and then decreases. At the reactor exit the mole fraction values of CO are almost equal for all three conditions. The crossover of CO mole fraction at R=0.0 and CO mole fraction R=1.77 is attributed to the same reasons mentioned above for the hydrogen mole fraction case.

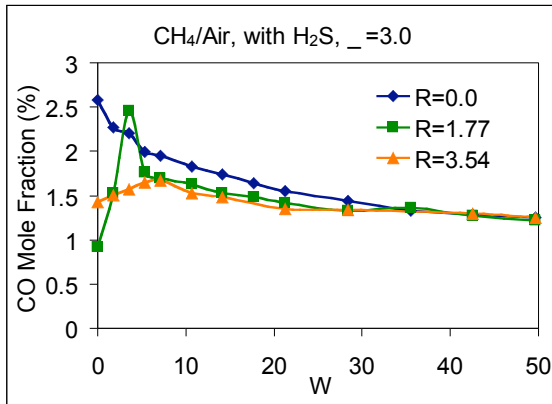


Figure 6. Carbon monoxide mole fraction. Flame conditions: CH₄/air with H₂S, $\Phi = 3.0$.

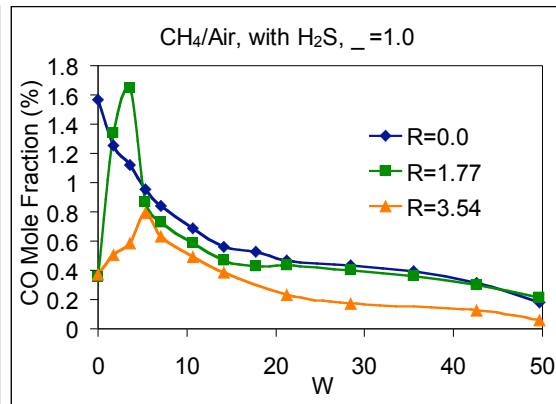


Figure 7. Carbon monoxide mole fraction. Flame conditions: CH₄/air with H₂S, $\Phi = 1.0$.

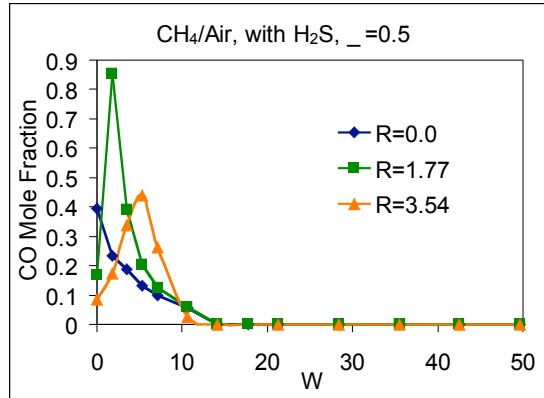


Figure 8. Carbon monoxide fraction. Flame conditions: CH₄/air with H₂S, $\Phi = 0.5$.

Figures 9 and 10 describe the formation of higher hydrocarbons (ethane and ethylene) in the reaction pool at R=1.77 and R=3.54 under Claus conditions. The formation of higher hydrocarbons is attributed to the coupling catalytic effect of sulfur dioxide. The absence of higher hydrocarbons at the centerline of the reactor is attributed to the higher local temperature. Moreover, SO₂ mole fraction at the centerline is minimal as compared to its concentration at R=1.77 and R=3.54, which reduces the coupling catalytic effect. On the other hand, the absence of higher hydrocarbons at stoichiometric and lean conditions is attributed to the low concentration of SO₂ in the reaction pool.

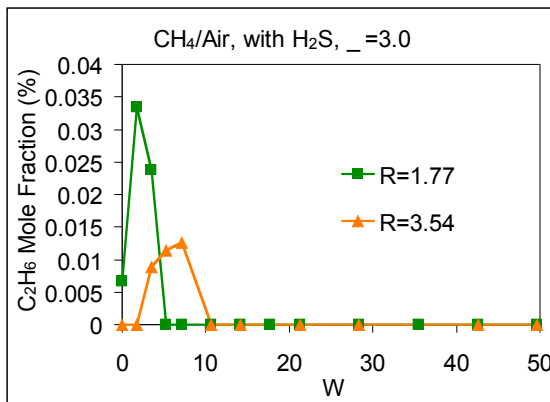


Figure 9. Ethane mole fraction. Flame conditions: CH₄/air with H₂S, $\Phi = 3.0$.

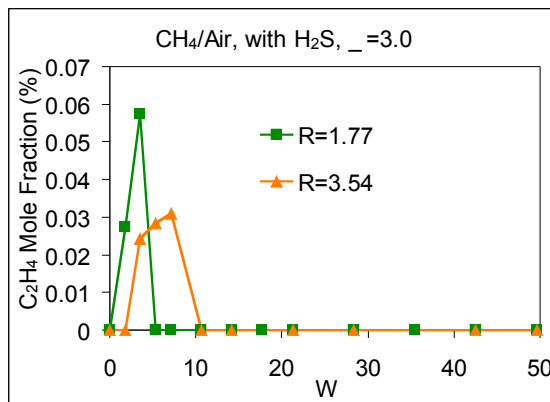


Figure 10. Ethylene mole fraction. Flame conditions: CH₄/air with H₂S, $\Phi = 3.0$.

Figure 11, 12, and 13 shows the mole fraction of hydrogen sulfide distribution at three specific radial locations along the reactor for three different equivalence ratios. At Claus conditions, H₂S peaks and then decreases in a consistent fashion. This is attributed to the lack of oxygen, which prevents the rapid combustion of H₂S. On the other hand, hydrogen sulfide mole fraction reaches its maximum at R=1.77 at any equivalence ratio. This is attributed to the fact that at R=1.77 the sampling probe is close to the path lines of injected reactants.

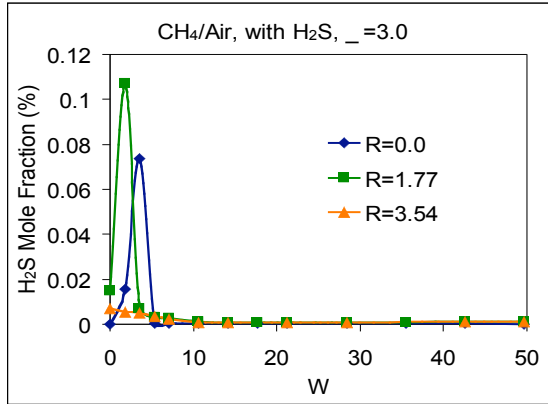


Figure 11. Hydrogen sulfide mole fraction. Flame conditions: CH₄/air with H₂S, $\Phi = 3.0$.

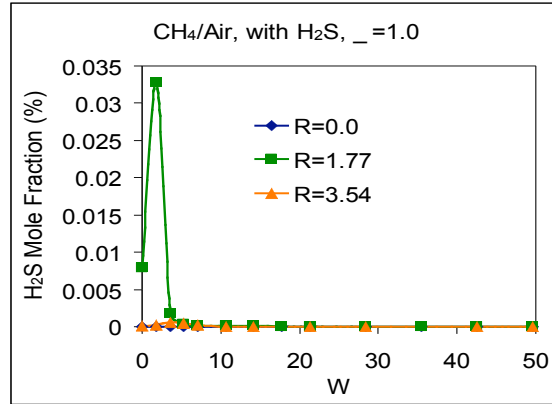


Figure 12. Hydrogen sulfide mole fraction. Flame conditions: CH₄/air with H₂S, $\Phi = 1.0$.

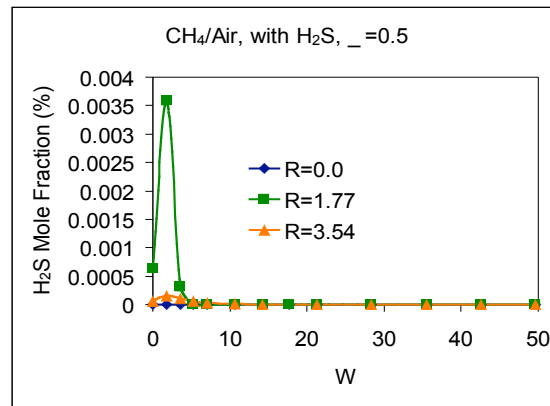


Figure 13. Hydrogen sulfide fraction. Flame conditions: CH₄/air with H₂S, $\Phi = 0.5$.

Figures 14, 15, and 16 show the distribution of sulfur dioxide mole fraction at different equivalence ratios along the reactor at three radial locations. At Claus conditions, SO₂ mole fraction increases until it reaches a maximum value and then decreases slightly with further increase in distance downstream of the burner exit. However, under stoichiometric and lean conditions SO₂ mole fraction increases along the reactor. At the reactor exit SO₂ mole fraction does not change significantly in the radial direction.

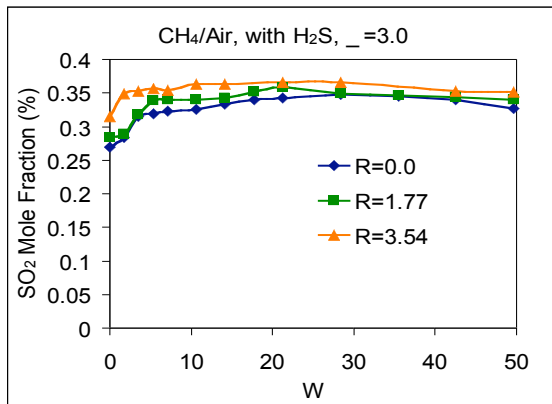


Figure 14. Sulfur dioxide mole fraction.
Flame conditions: CH₄/air with H₂S, $\Phi = 3.0$.

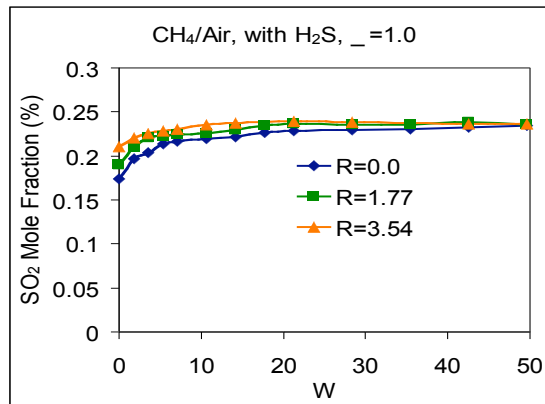


Figure 15. Sulfur dioxide mole fraction.
Flame conditions: CH₄/air with H₂S, $\Phi = 1.0$.

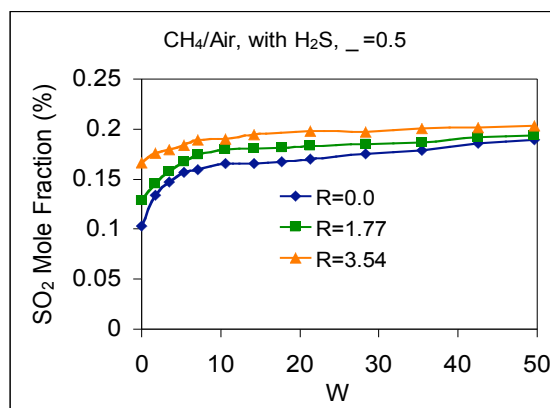


Figure 16. Hydrogen sulfide fraction. Flame conditions: CH₄/air with H₂S, $\Phi = 0.5$.

Figures 17 and 18 represent the distribution of carbon disulfide (CS₂) mole fraction at $\Phi = 3.0$ and $\Phi = 1.0$ where CS₂ was not observed under fuel lean conditions. Under Claus conditions, CS₂ mole fraction increases until it reaches a peak then decreases. However, under stoichiometric conditions CS₂ increases monotonically downstream of the reactor. The cause of CS₂ formation and its behavior from a chemical kinetics standpoint is an issue that requires further detailed investigation.

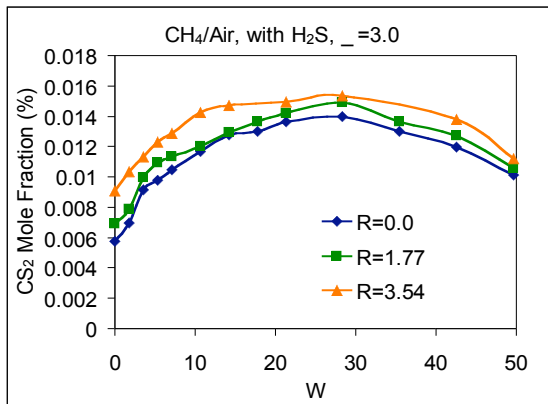


Figure 17. Carbon disulfide mole fraction. Flame conditions: CH₄/air with H₂S, $\Phi = 3.0$.

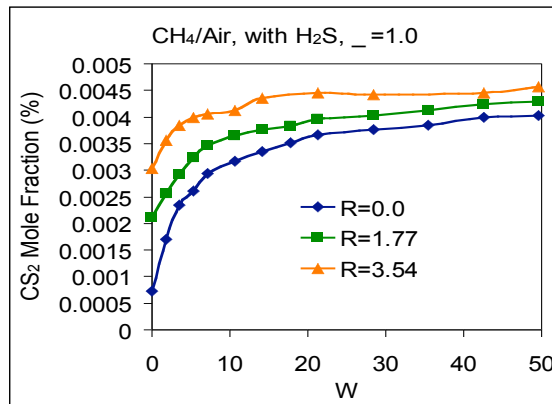


Figure 18. Carbon disulfide mole fraction. Flame conditions: CH₄/air with H₂S, $\Phi = 1.0$.

4.2 Prepare LIBS setup and sulfur samples for analysis

The laser-induced breakdown spectroscopy (LIBS) setup was put together to enable us to analyze the sulfur deposits. The LIBS setup introduces a powerful laser beam into a solid sample where the beam breaks the sample down to its elemental components. A 7-channel spectrometer will be used for the analysis of emission from excited elements. This will enable us to know whether other elements (such as carbon, nitrogen, or hydrogen) exist in the solid sulfur deposits. We have also prepared large sulfur samples for further testing and analysis. We have not been able to analyze them due to limited funds for their chemical analysis. The samples were formed using H₂S/O₂ flame. The high temperature of the flame allowed the condensed liquid sulfur to drip down the reactor walls and collect in the burner housing. A schematic of the reactor with the flame and sulfur samples collected are shown in Figure 19. A photograph of the 7-channel LIBS system as well as the appropriate laser, sample container, and lens to focus the laser beam is shown in Fig. 20.



Figure 19. Large sulfur chunks (left) formed in the burner steel housing (right).

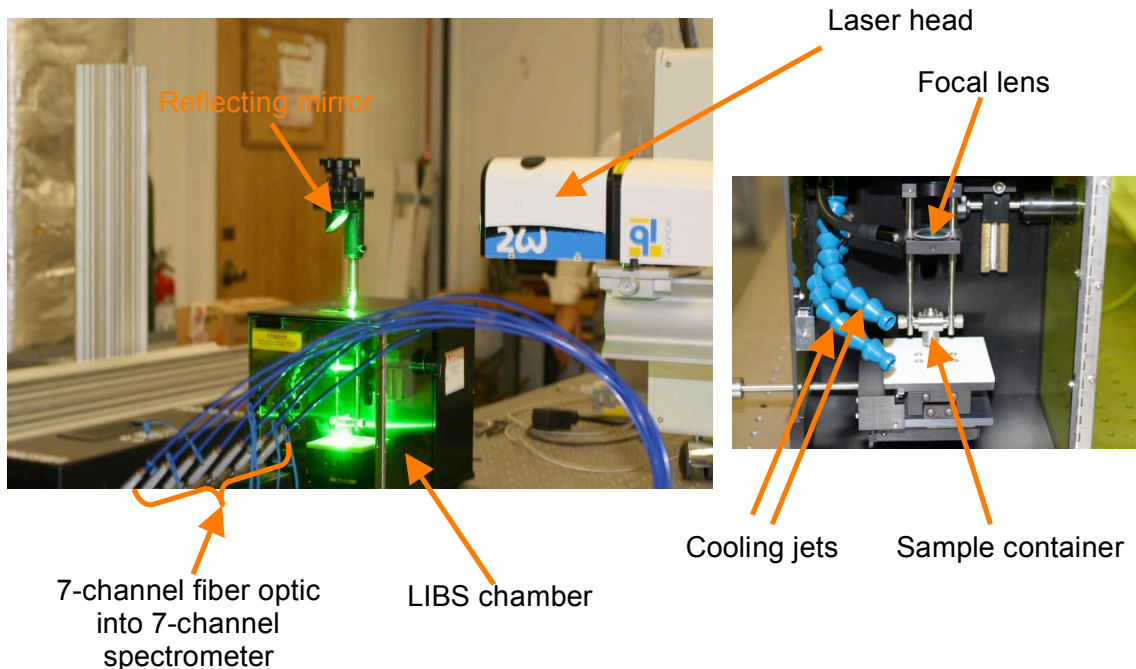


Figure 20. Laser-induced breakdown spectroscopy (LIBS) setup.

4.3 Write technical papers

During the past quarter we wrote two technical papers submitted to The Journal of Applied Energy. Both of these papers were accepted and are now available in the journal of high impact factor (J. Applied Energy). Moreover, the paper submitted from the Energy 2030 conference held in 2008 was revised and submitted to the J. Applied Energy in 2009. The reviewer's comments received during the last quarter were addressed and sent to the journal publication office. This paper has also been accepted for publication as well. All of the three journal papers are now available online. The citations for these three papers are given below.

- 1-Selim H et al. Experimental examination of flame chemistry in hydrogen sulfide-based flames. Appl Energy, Vol. 88, 2011, pp. 2601–2611, doi:10.1016/j.apenergy.2011.02.029.
- 2-Selim H et al. Effect of H₂S in methane/air flames on sulfur chemistry and products speciation. Appl Energy Vol. 88, 2011, pp. 2593–2600, doi:10.1016/j.apenergy.2011.02.032.
- 3-Selim H et al. Novel error propagation approach for reducing H₂S/O₂ reaction mechanism. Appl Energy (2011), doi:10.1016/j.apenergy.2011.01.047.

5. Summary

Examination of hydrogen sulfide combustion was conducted in methane/air flames at different equivalence ratios in a plug flow reactor. The burner injection configuration was changed in order to assure the best mixing conditions for the reactants. Gas sampling was performed axially along the reactor at three radial locations. The results emphasized the formation of higher hydrocarbons under Claus conditions. This is attributed to the coupling catalytic effect of sulfur dioxide. However, no observation of higher hydrocarbons was found at stoichiometric or lean conditions. Formation of carbon disulfide was observed under Claus and stoichiometric conditions. The cause of the formation of carbon disulfide from the chemical kinetics perspective requires further investigation. The laser-induced breakdown spectroscopy (LIBS) setup was prepared to facilitate

the analysis of sulfur deposits. Large sulfur samples were prepared using H₂S/O₂ flame for further detailed examination of the formed sulfur. Finally, two journal papers were written and submitted to The Journal of Applied Energy. Both papers have been accepted and are now published in the Journal of Applied Energy. This is a relatively high-impact journal. A third paper based on the conference paper presented at the Energy 2030 conference held in 2008 was modified and submitted to the Journal of Applied Energy. All the comments received on this paper were incorporated into the manuscript and the paper was resubmitted to the journal office. This paper is now also accepted and is now available online at the journal publication site.

6. References

- [1] Selim H et al. Effect of H₂S in methane/air flames on sulfur chemistry and products speciation. Appl Energy (2011), doi:10.1016/j.apenergy.2011.02.032.

7. Difficulties Encountered/Overcome

None.

8. Deliverables for the Next Quarter

- Further investigation of the formation of carbon disulfide from the chemical kinetics point of view.
- Examine H₂S/O₂ flame in presence of additional gases such as carbon dioxide with specific focus on the formation of COS and CS₂.
- Use the laser-induced breakdown spectroscopy (LIBS) setup in sulfur deposits analysis.
- Write technical paper for journal and conference publication.

9. Publications

Conference Publications

1. Gupta, A. K. and Sassi, M. "Sulfur Recovery from Acid Gas Using the Claus Process and High Temperature Air Combustion Technology," American J. of Environmental Sciences, Vol. 4, No. 5, 2008, pp. 502-511.
2. Selim, H., Gupta, A. K. and Sassi, M. "Variation of Optimum Claus Reactor temperature with Acid Gas Composition," IECEC Conference, Cleveland, OH, July 28-30, 2008, Paper No. AIAA-2008-5797.
3. Selim, H., Gupta, A. K. and Sassi, M. "Reduced Mechanism for Hydrogen Sulfide Oxidation," 47th AIAA Aerospace Sciences Conference, Orlando, FL, January 5-8, 2009, Paper No. AIAA-2009-1392.
4. Selim, H. and Gupta, A. K. "Nonreactive Study for the Reactants Mixing in Claus Reactions," 7th Intl. Energy Conversion Engineering Conference (7th IECEC), Denver, CO, August 2-5, 2009, Paper No. AIAA-2009-4506.
5. Selim, H, Gupta, A. K. and Sassi, M. "Reduction and Validation of Detailed Kinetic Reactions in Thermal Stage of Claus Process," 48th AIAA Aerospace Sciences Conference, Orlando, FL, (accepted for presentation and Publication), January 3-7, 2010, Paper AIAA-2010-1355.
6. Al Amoodi, N., Selim, H., Gupta, A. K., Sassi, M. and Al Shoaibi, A. "Numerical Simulations of the Thermal Stage in Claus Process: Equilibrium and Kinetic Investigation," 48th AIAA Aerospace Sciences Conference, Orlando, FL, January 3-7, 2010, AIAA-2010-1356.
7. Selim, H. Vijayan, V., Al Shoaibi, A., and Gupta, A. K., "Numerical and Experimental Studies on Mixing and Product Species Distribution in a Claus Reactor," 8th Intl. Energy Conversion Engineering Conference (8th IECEC), Nashville, TN, August 2-5, 2010, Paper No. AIAA-2010-7183.

8. Selim, H, Al Shoaibi, A., and Gupta, A. K., "Examination of Emission Spectra from Hydrogen Sulfide Flames," 49th AIAA Aerospace Sciences Conference, Orlando, FL, January 4-7, 2011, AIAA-2011-440.

Journal Publications

1. Selim H et al. Novel error propagation approach for reducing H₂S/O₂ reaction mechanism. Appl Energy (2011), doi:10.1016/j.apenergy. 2011.01.047.
2. Selim H et al. Experimental examination of flame chemistry in hydrogen sulfide-based flames. Appl Energy, Vol. 88, 2011, pp. 2601–2611, doi:10.1016/j.apenergy. 2011.02.029.
3. Selim H et al. Effect of H₂S in methane/air flames on sulfur chemistry and products speciation. Appl Energy, Vol. 88, 2011, pp. 2593–2600, doi:10.1016/j.apenergy. 2011.02.032.

Appendix

Justification and Background

Hydrogen sulfide is present in numerous gaseous waste streams from natural gas plants, oil refineries, and wastewater treatment plants, among other processes. These streams usually also contain carbon dioxide, water vapor, trace quantities of hydrocarbons, sulfur, and ammonia. Waste gases with ammonia are called sour gases, while those without ammonia are called acid gases. Sulfur must be recovered from these waste streams before flaring them. Sulfur recovery from sour or acid gas typically involves application of the well-known Claus process, using the reaction between hydrogen sulfide and sulfur dioxide (produced at the Claus process furnace from the combustion of H₂S with air and/or oxygen), yielding elemental sulfur and water vapor: $2\text{H}_2\text{S}(\text{g}) + \text{SO}_2(\text{g}) = (3/n) \text{S}_n(\text{g}) + 2\text{H}_2\text{O}(\text{g})$ with $\Delta H_r = -108 \text{ kJ/mol}$. Therefore, higher conversions for this exothermic, equilibrium-limited reaction call for low temperatures, which lead to low reaction rates that dictate the use of a catalyst. The catalytic conversion is usually carried out in a multistage, fixed-bed, adsorptive reactor process, which counteracts the severe equilibrium limitations at high conversions. This technology process can convert about 96% to 97% of the influent sulfur in H₂S to S. However, higher removal requires critical examination of the process and use of a near isothermal reactor, since the conversion is critically dependent upon the exothermic and endothermic conditions of the reactions.

Flameless combustion has been shown to provide uniform thermal field in the reactor so that the reactor temperature is near uniform. Reactor size can also be reduced and combustion-generated pollutants emissions can be reduced by up to 50%. Energy efficiency can be increased by up to 30%. The application of this technology appears to offer great advantages for the processes under consideration. The UAE, which pumps about 2.4 million bpd of crude oil, is also home to the world's fifth biggest gas reserves at about 200 trillion cubic feet. Abu Dhabi Gas Industries (GASCO), an operating company of the Abu Dhabi National Oil Company (ADNOC), is leading a drive to boost gas production in the UAE from five to seven billion cubic feet per day. This calls for sulfur recovery capacity of over 3,000 metric tons per day with the associated SO_x and NO_x emissions. Therefore, the adoption and further development of flameless combustion technology for sulfur recovery among other commercial and industrial heating processes is expected to be crucial and beneficial, both economically and environmentally.

The conventional sulfur recovery process is based upon the withdrawal of sulfur by in situ condensation within the reactor. The selective removal of water should, however, be a far more effective technique, as its effect on the equilibrium composition in the mass action equation is much greater. The in situ combination of the heterogeneously catalyzed Claus reaction and an adsorptive water separation seems especially promising, as both reaction and adsorption exhibit similar kinetics, and pressure can be adapted to the needs of the adsorptive separation. Such an adsorptive reactor will lead to almost complete conversion as long as the adsorption capacity is not exhausted. There are numerous possibilities for implementing these two functions, ranging from fixed-beds with homogeneous catalyst/adsorbent mixtures to spatially structured distributions or even fluidized beds. Most of the previous studies have concentrated on the Claus catalytic conversion reactors and the TGTU. However, some previous studies have identified the Claus furnace as one of the most important yet least understood parts of the modified Claus process. The furnace is where the combustion reaction and the initial sulfur conversion (through an endothermic gaseous reaction) take place. It is also where the SO₂ required by the downstream catalytic stages is produced and the contaminants (such as ammonia and BTX (benzene, toluene, xylene) are supposedly destroyed. The main two reactions in the Claus furnace are: $\text{H}_2\text{S} + 3/2 \text{O}_2 = \text{SO}_2 + \text{H}_2\text{O}$, with $\Delta H_r = -518 \text{ kJ/mol}$, and $2\text{H}_2\text{S} + \text{SO}_2 = 3/2 \text{S}_2 + 2\text{H}_2\text{O}$, with $\Delta H_r = +47 \text{ kJ/mol}$. This last endothermic reaction is responsible for up to 67% conversion of the sulfur at about 1200 °C. Moreover, many side reactions take place in the furnace; these side reactions reduce sulfur recovery and/or produce unwanted components that end up as ambient

pollutant emissions. Therefore, it would be useful to combine the endothermic and exothermic process using an isothermal reactor offered by flameless oxidation combustion.

Approach

Critical review

We propose to conduct a critical review of the various approaches used for sulfur removal from the sour gas. The emphasis here will be on sulfur chemistry with due consideration to the fate of ammonia. Following the review, an experimental and a CFD numerical study of the flameless oxidation of the fuel will be conducted as follows:

CFD simulation

A numerical simulation study of the flame under normal and flameless oxidation of fuels in the furnace will be conducted using the available codes. Global features of the flow and thermal behavior will be obtained using the Fluent CFD and Chemkin computer codes. These codes provide detailed simulation of the flow, thermal and chemical behaviors (i.e., detailed chemistry) in the reactor flow using gas-phase reactants. The sulfur in the fuel is in gas phase, so we will be able to simulate and monitor the fate of sulfur during various stages of endothermic and exothermic reactions and over a range of temperature regimes, including those covered in the Claus furnace process. The simulation results will also guide the final design of the flameless furnace. The simulations will also help assist in the experimental program for data validation with the eventual goal of implementing the process for sulfur removal.

Experimental study

An experimental study of the flameless vs. normal flame combustion process for the conditions examined in the theoretical study, including that of Claus furnace, will be conducted. We will explore the operating conditions and the exhaust gas analysis under conditions of both flame and flameless modes to determine the extent of sulfur conversion under the two conditions over the temperatures that can simulate endothermic and exothermic conditions in the Claus furnace. The goal is to seek conditions that yield the highest sulfur recovery from a process. To some extent, these conditions will be based on the composition of the acid/sour gas, from sulfur-rich (> 50% H₂S) to lean (< 20% H₂S). It is expected that our fundamental information will contribute to the eventual design guidelines of an advanced sulfur recovery process furnace operating under flameless combustion mode.

Separate Sensible and Latent Cooling with Solar Energy

UMD Investigators: Reinhard Radermacher, Yunho Hwang

GRA: Ali Al-Alili

PI Investigator: Isoroku Kubo

Start Date: August 2007

1. Objective/Abstract

The main objective of this project is to design, fabricate and test a solar cooling system with the highest possible cooling COP measured to date. The approach involves combining a very efficient concentrating PV-T collector with the separate sensible and latent cooling approach developed at CEEE. This solar cooling system is expected to operate under the UAE's harsh climate conditions.

2. Deliverables for the Completed Quarter

These are the accomplished tasks:

- Calibrated the refrigerant and the water mass flow meters
- Finished the hot water loop
- Connected the instrumentation to the data acquisition system
- Created a LabView program for the experiment
- Wired the experimental power supply side and installed it in the power cabinet

3. Summary of Project Activities for the Completed Quarter

The focus of this quarter was to finalize the construction of the experiment setup. Once the duct construction was completed, the focus shifted to the water and refrigerant loops. Two mass flow meters were calibrated for use in these two loops. In addition, the instruments were connected to the data acquisition system and a lab view program was created to read, analysis and save the data.

Mass flow meter calibration

There are two mass flow meters used in this experiment, one each for the refrigerant loop and the hot water loop. These two mass flow meters were calibrated using a bucket and stopwatch method. Basically, the mass of water was run through the flow meter for a certain period of time and collected in a bucket. Then, the mass of water only was measured and recorded. After that, the mass flow rate would be calculated, by dividing the mass by the time, and plotted as a function of the flow meter current output, as shown in Figures 1 and 2.

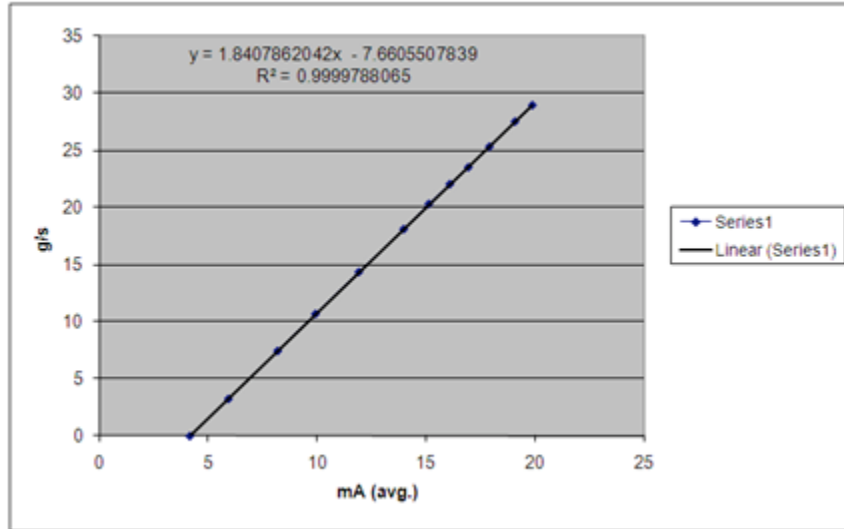


Figure 1. Calibration curve for the refrigerant loop.

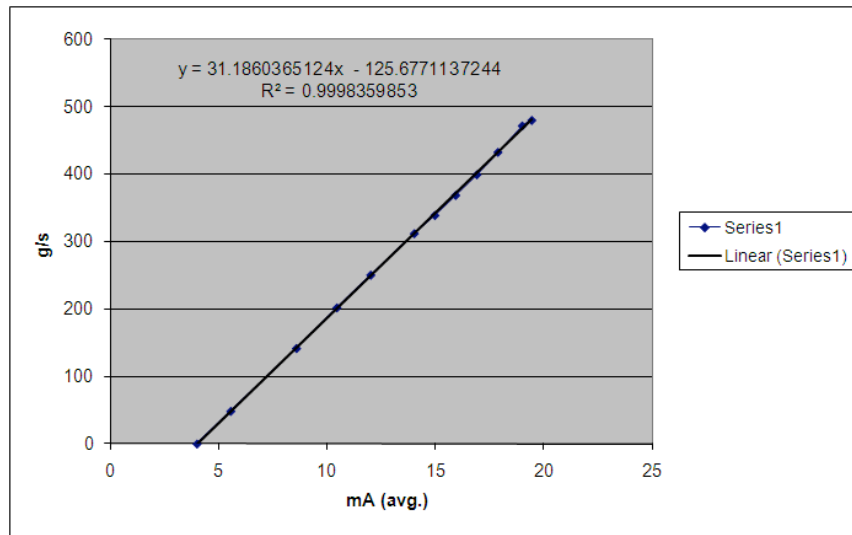


Figure 2. Calibration curve for the water loop.

Hot water loop

The hot water loop includes a storage tank, pump, mass flow meter (shown in Figure 4) and a water-air heat exchanger. The storage tank, shown in Figure 3, is insulated in order to minimize the heat lost to the environment. There is also a T-type thermocouple installed in the middle of the tank. The tank has two heating elements with a capacity of 1,500 W each.



Figure 3. Hot water storage tank.



Figure 4. Water loop mass flow meter.

Data acquisition

All the measurements, temperature, relative humidity and differential pressures, were connected to the data acquisition system, as shown in Figure 5. A lab view program was expanded to record the measurements, as shown in Figure 6.

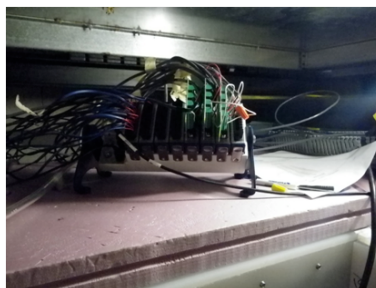


Figure 5. Data acquisition.

Measurement	Sensor Signal		Sensor Range		Unit	Use	Data
	min signal	max signal	min range	max range			
20.256	0	1	0	1	°C	✓	20.25
20.4813	0	1	0	1	°C	✓	20.48
20.4603	0	1	0	1	°C	✓	20.46
20.5773	0	1	0	1	°C	✓	20.58
20.5463	0	1	0	1	°C	✓	20.54
20.3623	0	1	0	1	°C	✓	20.36
20.0803	0	1	0	1	°C	✓	20.1
19.4122	0	1	0	1	°C	✓	19.41
19.5227	0	1	0	1	°C	✓	19.52
19.4823	0	1	0	1	°C	✓	19.48
19.4578	0	1	0	1	°C	✓	19.46
19.5623	0	1	0	1	°C	✓	19.56
19.5623	0	1	0	1	°C	✓	19.56
19.576	0	1	0	1	°C	✓	19.58
0.0006247	0.004	0.02	0	0.05	MPa	✓	0.0044
0.0008872	0.004	0.02	0	0.05	MPa	✓	0.0052
0.0007039	0.004	0.02	0	0.05	MPa	✓	0.0051
0.0008946	0.004	0.02	0	0.05	MPa	✓	0.0057
0.0007232	0.004	0.02	0	0.05	MPa	✓	0.0053
0.0009439	0.004	0.02	0	0.05	MPa	✓	0.0054
0.0009079	0.004	0.02	0	0.05	MPa	✓	0.0054
0.0009172	0.004	0.02	0	0.05	MPa	✓	0.0048
0.0009207	0.004	0.02	0	0.05	MPa	✓	0.0044
0.0009046	0.004	0.02	0	0.05	MPa	✓	0.0034
0.0009103	0.004	0.02	0	0.05	MPa	✓	0.0038
0.0008824	0.004	0.02	0	0.05	MPa	✓	0.0039
0.0007086	0.004	0.02	0	0.05	MPa	✓	0.0038
0.0009426	0.004	0.02	0	0.05	MPa	✓	0.0037
0.0009067	0.004	0.02	0	0.05	MPa	✓	0.0032
0.0009402	0.004	0.02	0	0.05	MPa	✓	0.0033
0.00095	0.004	0.02	0	0.05	MPa	✓	0.0039
0.00095	0.004	0.02	0	0.05	MPa	✓	0.0039

Figure 6. Screen shot of Labview.

Vapor compression cycle

Four modules to record the temperature and pressure at each refrigerant state point were built, as shown in Figure 7. A plastic panel was used to mount the refrigerant mass flow meter and its transducer.



Figure 7. Temperature and pressure modules.

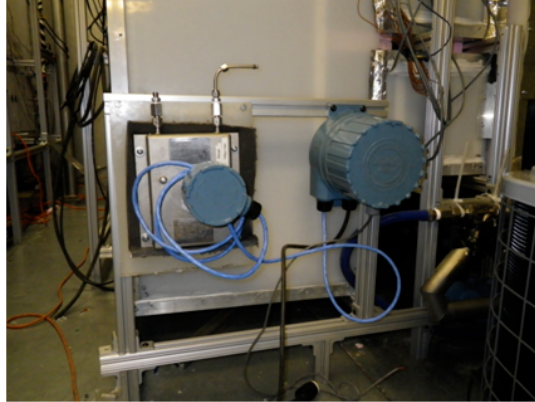


Figure 8. Ducts connected together.

Power supply

Due to the size of the experiment and different electrical requirements of its components, different power voltages and various electrical components were required, as shown in Figure 9. Solid state relays were used to connect and discount the components that were not required to be controlled. The on/off switching was done with Labview. Variable frequency controllers were used to control the fans' speeds. All the power lines were equipped with fuses for safety purposes.

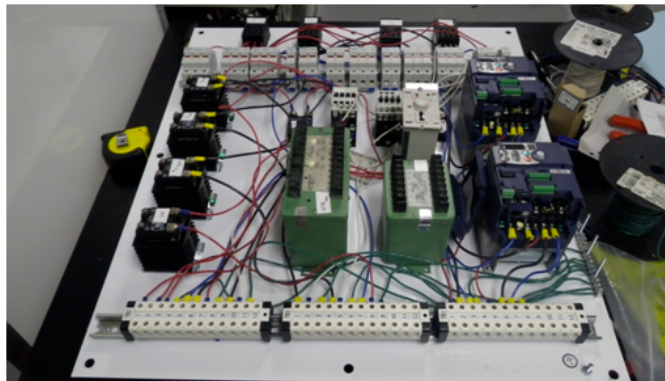


Figure 9. Power supply panel.



Figure 10. Power supply cabinet.

4. Difficulties Encountered/Overcome

- Connecting the different measurements to the DAQ
- Configuring Labview

5. Planned Project Activities for the Next Quarter

The following activities are to be conducted in the next quarter:

- Finish the refrigerant loop
- Run a shakedown test of the desiccant wheel

Appendix

References

- [1] Stine, W.B., Geyer, W.B., 2001, Power from the sun, www.powerfromthesun.net.
- [2] Threlkeld, J., Kuehn, T., Ramsy, J., 1998, Thermal Environmental Engineering, Prentice-Hall, Inc, USA
- [3] http://www.nrel.gov/rredc/solar_data.html
- [4] http://rredc.nrel.gov/solar/old_data/nsrdb/tmy2/State.html
- [5] Nottton, G., Poggi, P., Cristofari, C., 2006, Predicting hourly solar irradiations on inclined surfaces based on the horizontal measurements: Performances of the association of well-known mathematical models, *Energy Conversion and Management*, 47 1816–1829
- [6] http://rredc.nrel.gov/solar/old_data/nsrdb/1991-2005/siteonthefly.cgi?id=724060
- [7] ASHRAE, 1999, Applications Handbook, CH.32
- [8] Kreith, F. and Kreider, J.F., 1978, Principles of solar engineering, *Hemisphere publishing corporation* Washington USA
- [9] Kalogirou, S., 2004, Solar thermal collectors and applications, *Progress in Energy and Combustion Science* 30 pp. 231–295
- [10] Goswami, Y., Kreith, F. and Kreider, J.F., 2000, Principles of solar engineering, *Taylor and Francis*, PA, USA,
- [11] Duffie, J.A., Beckman, W.A., 1991, *Solar engineering of thermal processes*, Second edition, John Wiley & Sons, Inc., New York, ISBN: 0-471-51056-4.
- [12] Pasupathy, A., Velraj, R., Seeniraj, R.V., 2008, Phase change material-based building architecture for thermal management in residential and commercial establishments, *Renewable and Sustainable Energy Reviews*, pp.39–64
- [13] Dieng, A., Wang, R., 2001 Literature Review on Solar Adsorption Technologies of Ice-making and Air Conditioning Purposes and Recent Developments in Solar Technology, *Renewable and Sustainable Energy Reviews* 5 pp.313–342
- [14] Sumathy, K., Yeung, K, Yong, L., 2003, Technology Development in the Solar Adsorption Refrigeration Systems, *Progress in Energy and Combustion Science* 29 pp 301–327
- [15] Roger, A. Messenger, J. V., 2005, Photovoltaic Systems Engineering, 2nd ed. Taylor & Francis
- [16] <http://www.nfpa.org/>
- [17] <http://ieeexplore.ieee.org/iel5/7946/21930/01019771.pdf?arnumber=1019771>
- [18] TRANE, "Product Data: 4DCZ6036A through 4DCZ6060A" (2008), 22-1815-03
- [19] METEONORM, "Global Meteorological Database for Engineers, Planners and Education,"(2007)

Waste Heat Utilization in the Petroleum Industry

UMD Investigators: Reinhard Radermacher, Yunho Hwang

GRAs: Amir Mortazavi, Abdullah Alabdulkarem

PI Investigators: Saleh Al Hashimi, Peter Rodgers

Start Date: October 2006

1. Objective/Abstract

The main objective of this project is to minimize overall energy consumption of gas or oil processing plants with CO₂ capture and sequestration by utilizing waste heat and/or improving cycle design. Consideration will include the use of absorption chillers and steam cycles, among other options.

2. Deliverables for the Completed Quarter

The following were modeled using HYSYS:

- Modeled the open CO₂ liquefaction cycle
- Verified the CO₂ liquefaction cycle model with EES
- Modeled heat pump cycle with different refrigerants
- Optimization of two configurations of gas turbine combined cycle with double-pressure steam cycle
- Optimization of two configurations of gas turbine triple combined cycle with double-pressure steam cycle and absorption chillers.

3. Summary of Project Activities for the Completed Quarter

HYSYS was used to model the open CO₂ liquefaction cycle that is captured from a flue gas of gas-turbine-based power plant. The open CO₂ liquefaction cycle was compared with the developed vapor compression cycles for CO₂ liquefaction, which was developed in our previous work. Further, the heat pump cycle was also modeled in HYSYS.

Two configurations of both gas turbine combined cycles, double-pressure steam-cycle and gas turbine triple-combined cycle with double-pressure steam cycle and absorption chillers, were optimized as an APCI LNG plant driver cycle. The best option, according to our models, consumes 38.2% less fuel than the base line cycle.

3.1 Heat pump model

A heat pump model was developed using HYSYS software as shown in Figure 1. The refrigerant was compressed to high temperature, e.g., 130 °C, and then cooled in three heat exchangers. The first heat exchanger represents a high-temperature heat exchanger with an outlet temperature of 100 °C. The second heat exchanger cools the refrigerant to 80 °C. The third heat exchanger cools the refrigerant to the environment temperature, e.g. 40 °C. Different refrigerants were explored and tabulated in Table 1.

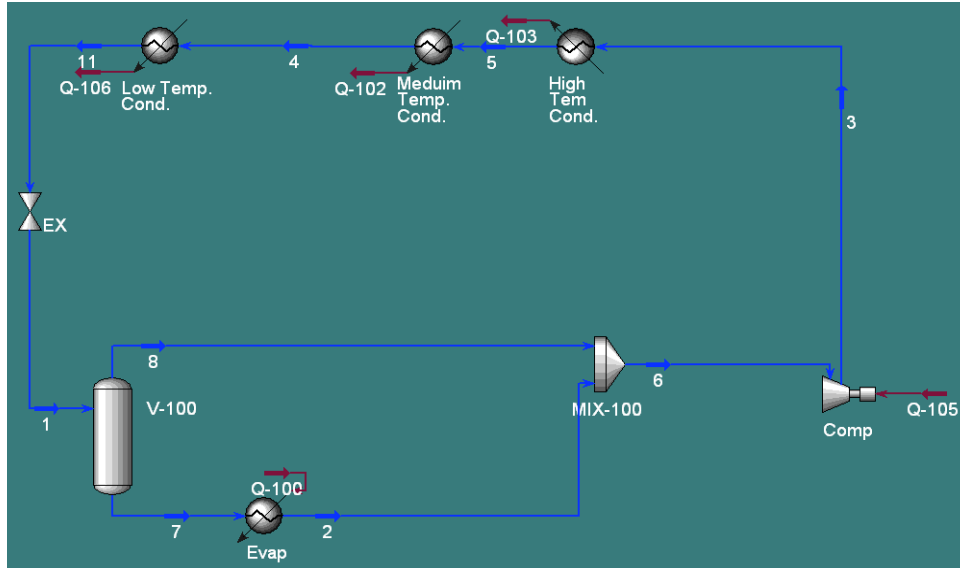


Figure 1. HYSYS heat pump model.

Table 1. Performance of the heat pump

Refrigerant	Compressor Power (MW)	Evaporator Capacity (MW)	Cooling COP
R141b	23.64	77.77	3.29
R123	26.31	82.47	3.13
R115	62.61	201.42	3.22
R134a	63.01	221.92	3.52
R404A	63.16	210.77	3.34
Propane	55.15	187.17	3.39
R420A	66.93	233.35	3.49
R22	124.73	488.20	3.91
R125	67.27	211.82	3.15
Isobutane	32.29	104.23	3.23

3.2 Open CO₂ Liquefaction Cycle

In order to inject CO₂ into a gas or oil reservoir, it needs to be pressurized to above the supercritical pressure. One way to pressurize CO₂ is to liquefy it and then pump it to the desired pressure. The open CO₂ liquefaction cycle is a patented cycle for liquefying the CO₂ from a stationary source by Aspelund *et al.* (Patent No. US20080156035). The working principle of the cycle is that it uses the CO₂ to liquefy itself. The cycle consists of three compression stages and two multi-stream heat exchangers. A portion of the compressed CO₂ is re-circulated and expanded in an expansion valve. Due to expansion, the CO₂ will be used to cool another incoming CO₂ stream. Then the heated CO₂ will be sent back in a vapor state to an intermediate stage compressor. A final expansion valve is used to expand the compressed and cooled CO₂ to a low pressure at a saturation state where the vapor and liquid are separated. The vapor is used in cooling the incoming stream, while the liquid is sent to storage or pumping.

A HYSYS model for the open CO₂ liquefaction cycle was developed (Figure 2). The equation of state used in this model is also the Peng-Robinson equation of state. The resulting power consumption for liquefying the CO₂ at 40°C condensing temperature and 50 bar compression pressure was calculated as 28.7 MW. In comparison, the developed ammonia cycle power consumption was only 5.93 MW. Different power consumption levels for the open CO₂ liquefaction cycle will be calculated at different condensing temperatures and pressures.

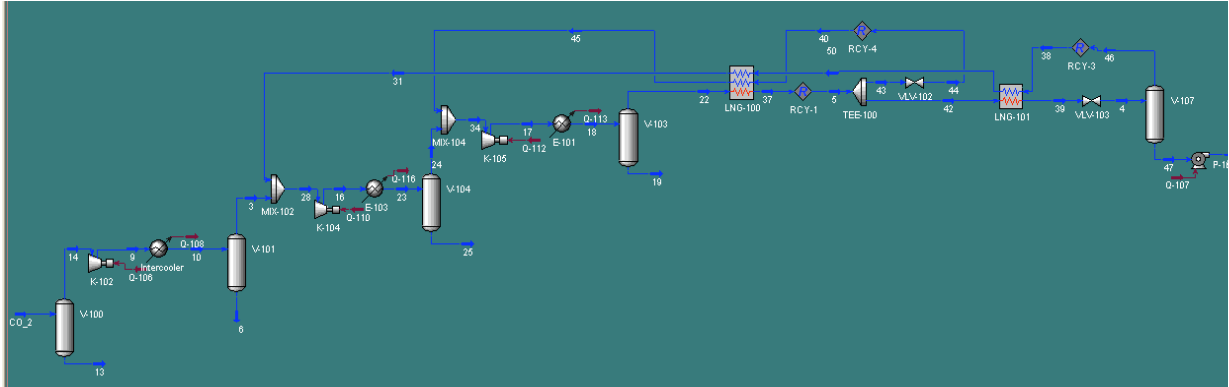


Figure 2. Open CO₂ liquefaction cycle HYSYS model.

To verify the HYSYS open CO₂ liquefaction cycle model, an EES model was developed. The calculated power consumption from the EES model was 28.38 MW, which resulted in only 1.12% discrepancy. The P-h diagram from the EES model is shown in Figure 3.

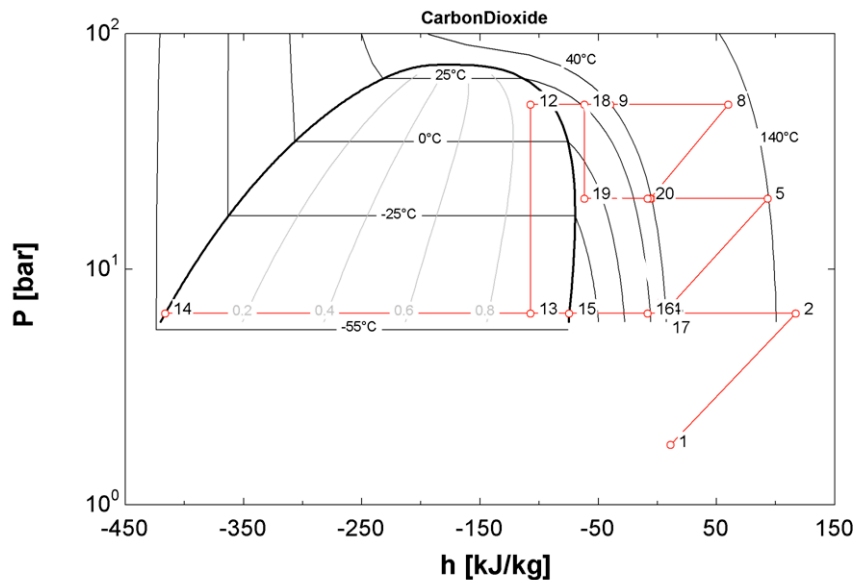


Figure 3. P-h diagram of the open CO₂ liquefaction cycle.

3.3 Optimization of different gas turbine triple combined cycle configurations

In order to investigate the potential of gas turbine, steam and absorption chiller combined cycles as an APCI LNG plant driver, the performance of the driver system should be optimized. Moreover, to fully appreciate the benefits of this system it should be compared to the optimized conventional technologies. Matlab software was used as an optimization tool. It was connected to HYSYS, which was used to model the driver cycles. Double-pressure combined cycles with reheat and without reheat were optimized. Moreover, two different configurations of the triple combined cycle were considered: triple-cycle gas turbine double-pressure steam with double-effect absorption chiller with reheat combined cycle, and triple-cycle gas turbine double-pressure

steam with single-effect absorption chiller with reheat combined cycle. The HYSYS model of the double-pressure combined cycle and double-pressure combined cycle with reheat are shown in Figures 4 and 5, respectively. The comparison of different driver technologies is shown in Table 3. As shown in Table 3, the most efficient driver configuration is the gas turbine double-pressure steam and single-effect water Li/Br absorption chiller triple combined cycle. This configuration has the lowest fuel consumption. Moreover, it maintains its advantages by varying the steam turbine efficiency and minimum exhaust temperature. Its efficiency is 38.2% and 2% higher than conventional gas turbines and the gas turbine and double-pressure steam combined cycle with reheat drivers, respectively. Moreover, as shown in Table 3, the cycles with auxiliary burner are not more efficient than the normal cycles, since optimization results showed zero fuel mass flow rate to the burner. Therefore, they were not considered for double pressure cycles.

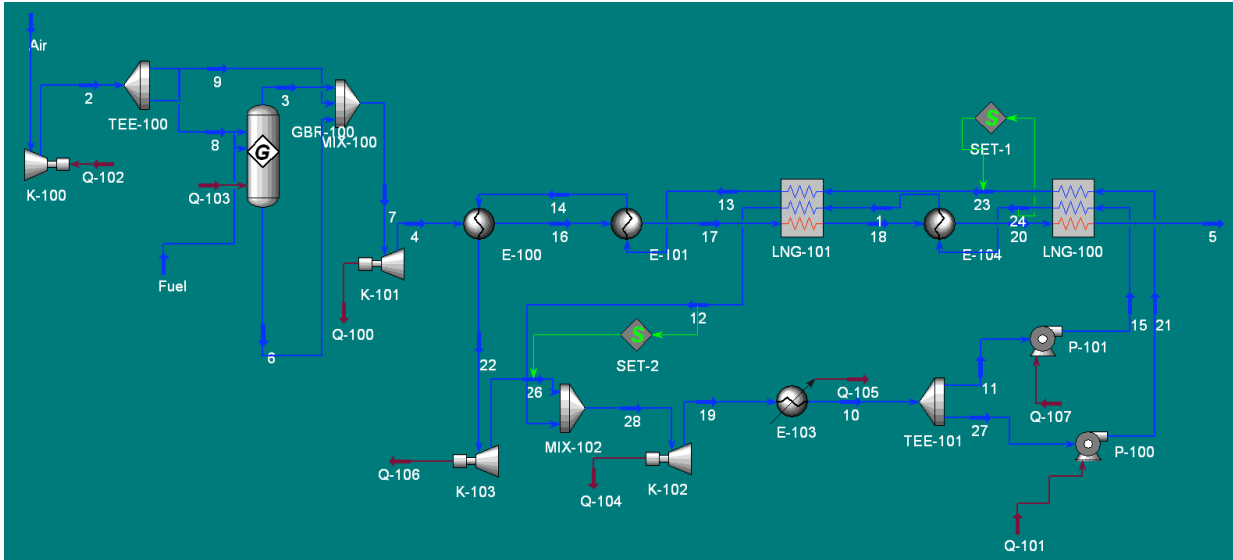


Figure 4. HYSYS model of double pressure combined cycle.

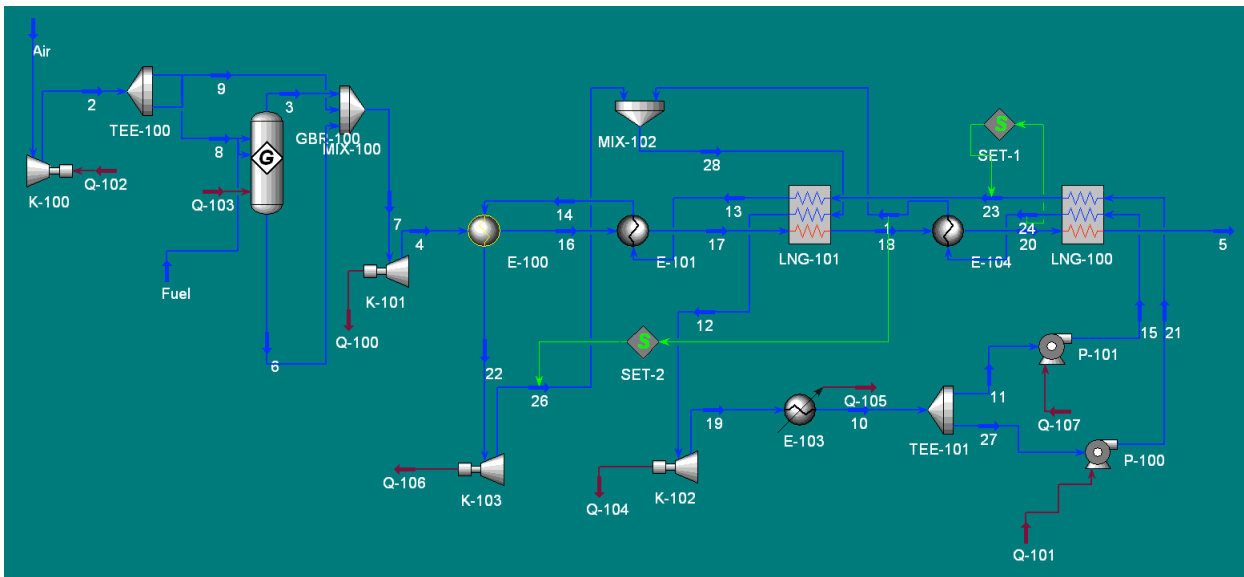


Figure 5. HYSYS model of double pressure combined cycle with reheat.

Table 3. Comparison of different driver cycle technologies

Steam Turbine Efficiency (%)	86	90	90	86	90	90	86	90	90
Exhaust Temperature (°C)	180	180	110	180	180	110	180	180	110
Cycle	Fuel Consumption (kg/s)			Efficiency (%)			Efficiency Enhancement (%)		
Base cycle with gas turbine as a driver	6.575	6.575	6.575	33.52	33.52	33.52	---	---	---
Combined gas turbine and double-effect absorption chiller	5.174	5.174	5.174	42.59	42.59	42.59	21.31	21.31	21.31
Combined gas turbine and single-pressure steam cycle	4.571	4.541	4.407	48.21	48.53	50.00	30.48	30.93	32.98
Triple-cycle with double-effect absorption chiller	4.704	4.641	4.641	46.85	47.48	47.48	28.46	29.41	29.41
Triple-cycle with single-effect absorption chiller	4.251	4.235	4.219	51.84	52.03	52.23	35.35	35.59	35.84
Split-design triple-cycle with double-effect absorption chiller	4.581	4.556	4.556	48.10	48.37	48.37	30.33	30.71	30.71
Split-design triple-cycle with single-effect absorption chiller	4.594	4.585	4.556	47.97	48.06	48.37	30.13	30.27	30.71
Triple-cycle with double-effect absorption	4.704	4.641	4.641	46.85	47.48	47.48	28.46	29.41	29.41

chiller with auxiliary burner									
Triple-cycle with single-effect absorption chiller auxiliary burner	4.251	4.235	4.219	51.84	52.03	52.23	35.35	35.59	35.84
Combined gas turbine and double-pressure steam cycle W R	4.438	4.367	4.140	49.65	50.46	53.22	32.5	33.58	37.03
Triple-cycle with double - pressure steam double-effect absorption chiller W R	4.791	4.707	4.707	46	46.82	46.82	27.13	28.41	28.41
Triple-cycle with double-pressure steam single-effect absorption chiller W R	4.241	4.195	4.066	51.96	52.53	54.20	35.50	36.20	38.16
Split-design triple-cycle with double-pressure steam double-effect absorption chiller W R	Not Complete								
Split-design triple-cycle with double-pressure steam single-effect absorption chiller W R	Not Complete								
Combined gas turbine and double-pressure steam cycle W O R	4.571	4.541	4.407	48.21	48.53	50.00	30.48	30.93	32.98

4. Difficulties Encountered/Overcome

None.

5. Planned Project Activities for the Next Quarter

The following activities are to be conducted in the next quarter:

- Model organic Rankine cycle and integrate it with the rest of the models.
- Optimize the gas turbine, dual-pressure steam and absorption chiller triple-combined cycle split designs
- Optimize mobile LNG plants using robust optimization

Appendix

Justification and Background

Waste heat utilization opportunities are abundant in the oil and gas industry. Proper use of waste heat could result in improved cycle efficiency, reduced energy usage, reduction in CO₂ emissions, and increased production capacity.

CEEE at the University of Maryland has extensive experience in the design and implementation of integrated combined cooling, heating, and power (CCHP) projects. The faculty at PI has experience in the design and operation of petroleum processing plants. Jointly the team is well equipped to address the challenge posed by this project.

References

- [1] Dopazo J. A., and Fernández-Seara J., 2010, "Experimental evaluation of a cascade refrigeration system prototype with CO₂ and NH₃ for freezing process applications," *International Journal of Refrigeration*, pp. 1-11.
- [2] Venkatarathnam G., 2008, *Cryogenic Mixed Refrigerant Processes*, Springer-Verlag New York, LLC,.
- [3] Paradowski H., Bamba M. O., and Bladanet C., 2004, "Propane Precooling Cycles for Increased LNG Train Capacity," 14th International Conference and Exhibition on Liquefied Natural Gas, pp. 1-18.
- [4] Alefeld, G., Radermacher, R., 1994, "Heat conversion systems," CRC Press, Boca Raton.
- [5] Al-Hamdan, Q.Z., Ebaid, M.S.Y., 2006, "Modeling and simulation of a gas turbine engine for power generation," *ASME Journal of Engineering for Gas Turbines and Power*, Vol. 128, pp. 302-311.
- [6] LNG technology selection,
- [7] http://www.fwc.com/publications/tech_papers/files/TariqLNG.pdf, Last access, June, 2008
- [8] Haring, H., 2008, "Industrial Gas Processing," Wiley-VCH, Weinheim
- [9] ASHRAE, 2002, "ASHRAE Refrigeration Handbook," American Society of Heating, Refrigeration and Air-Conditioning Engineers, Atlanta, GA, USA.
- [10] ASHRAE, 2005, "ASHRAE Fundamentals Handbook," American Society of Heating, Refrigeration and Air-Conditioning Engineers, Atlanta, GA, USA.
- [11] Brant, B., Brueske, S., Erickson, D.C., Papar, R., 1998, "New waste-heat refrigeration unit cuts flaring, reduces pollution," *Oil & Gas Journal*, May 18, pp.61-64.
- [12] Brooks, F.,J., 2000 "GE gas turbine performance characteristics," GE Power Systems Schenectady, NY, GER-3567H.
- [13] Cohen, H., Rogers, G.F.C., Saravanamuttoo, H.I.H., 1996, "Gas turbine theory," 4th edition, Longman Scientific & Technical, Singapore.
- [14] Erickson, D.C., 2000 "LPG recovery from reformer treat gas," US Patent 6,158,241.
- [15] Erickson, D.C., Anand, G., Papar, R.A., Tang, J., 1998, "Refinery waste heat powered absorption refrigeration – cycle specification and design," *Proceeding of the ASME Advanced Energy System Division*, AES-Vol. 38, pp.391-402.
- [16] Erickson, D.C., Kelly, F., 1998, "LPG recovery from refinery by waste heat powered absorption refrigeration," *IECEC-98-079*, 33rd Intersociety Engineering Conference on Energy Conversion, Colorado Springs, CO.
- [17] Giampaolo, T., 2003, "The gas turbine handbook: principles and practices," 2nd edition, The Fairmont Press, Lilburn, GA.
- [18] Herold, K.E.; Radermacher, R., Klein, S, 1996, "Absorption chillers and heat pumps," CRC Press, Boca Raton.
- [19] Kim, T.S., Hwang, S.H., 2006, "Part load performance analysis of recuperated gas turbine considering engine configuration and operation strategy," *Energy*, Vol. 31, pp., 260-277.
- [20] Klein, S.A., 2005, "Engineering Equation Solver" F-Chart Software.

- [21] Kurz, R., 2005, "Gas turbine performance," 44th Turbomachinery Symposium, pp.131-146.
- [22] Kurzke, J., 2003, "Model based gas turbine parameter corrections," GT2003-38234, Proceedings of 2003 ASME TURBO EXPO: Power for Land, Sea, & Air, Atlanta, GA, USA.
- [23] Li, Y.G., Pilidis, P., Newby, M.A., 2006, "An adaptation approach for gas turbine design-point performance simulation," Journal of Engineering for Gas Turbines and Power, Vol. 128, pp. 789-795.
- [24] Orlando, J. A., 1996, "Cogeneration design guide," American Society of Heating, Refrigeration and Air-Conditioning Engineers, Atlanta, GA.
- [25] Pande, M., 1996, "Tools for fractionator design in ammonia-water absorption machines," Master Thesis, University of Maryland, College Park.
- [26] Walsh, P.P., Fletcher, P., 1998, "Gas turbine performance," Blackwell Science, Oxford.



Thrust 2
Energy-Efficient Transport Processes

Multidisciplinary Design and Characterization of Polymer Composite Seawater Heat Exchanger Module

PI Investigator: Peter Rodgers

UMD Investigators: Avram Bar-Cohen, Satyandra K. Gupta, David Bigio, H.A. Bruck

GRAs: Juan Cevallos, F. Robinson, T. Hall, W. Pappas

Start Date: Oct 2006

1. Introduction

Heat exchangers are extensively used in all oil and gas processing operations with seawater as the preferred coolant in near-shore operations. The performance and cost effectiveness of conventional metallic heat exchangers in such environments are severely constrained by corrosion and scale deposits. Polymer heat exchangers, currently under investigation by the EERC team, offer a promising alternative to metallic heat exchangers for the fossil fuel industry. Recent advances in carbon-fiber polymer composites, yielding polymer materials with thermal conductivities equal to or higher than titanium, can be applied to the development of low-cost and low-weight compact heat exchangers for corrosive fluids. These attributes, combined with the low energy investment in the formation and fabrication of these polymer heat exchangers and their ease of manufacturing, appear to make near-term applications of seawater polymer heat exchangers viable. Numerical simulations and laboratory experiments, performed by the UMD/PI EERC team in the first phase of this research, strongly support these conclusions.

2. Milestones/Deliverables for the Completed Quarter

- I. Revisited thermal anisotropy of polymer composite fins induced by fiber orientation (Task A2)
- II. Developed and used thermomechanical finite element model to assess thermal and structural performance of polymer composite heat exchanger, and assessed feasibility of replacing metallic heat exchangers at the Das Island liquefied natural gas facility with polymer composite heat exchangers (Task A2)
- III. Developed accurate mold-filling metamodel using advanced datapoint selection methodology
- IV. Developed new image processing methodology for identifying fibers in microscope images of sample heat exchanger geometry
- V. Developed a technique for characterizing mixing of polymer composites in a Twin Screw Extruder (Task C1)
- VI. Submitted abstract and draft paper entitled "An Integrated Approach to Design of Enhanced Polymer Heat Exchangers" to DETC Conference to be held on August 29-31 2011 in Washington, DC (Task A2)
- VII. Submitted abstract entitled "Polymer Heat Exchangers – An Enabling Technology for Water and Energy Savings" to IMECE Conference to be held on November 11-17 2011 in Denver, Colorado (Task A2)
- VIII. Submitted abstract for a technical paper entitled "Modeling and Validation of Prototype Thermally Enhanced Polymer Heat Exchanger" to the 2011 International Mechanical

Engineering Congress & Exposition in Denver, Colorado (Task A2). Paper has been accepted.

3. Summary of Project Activities

I. Revisit thermal anisotropy of polymer composite fins induced by fiber orientation

Previous work reported in the first quarterly report of Phase II (July 1st, 2009) was revisited to include a more refined map of the process-induced fiber orientation in a polymer composite fin.

Originally, fiber orientation results had been sampled at only 15 locations in a 2.5 mm-thick, 5 mm-high fin. Now, a 190-point orientation 2D tensor map has been successfully exported from Moldflow into MATLAB (see Figure 1).

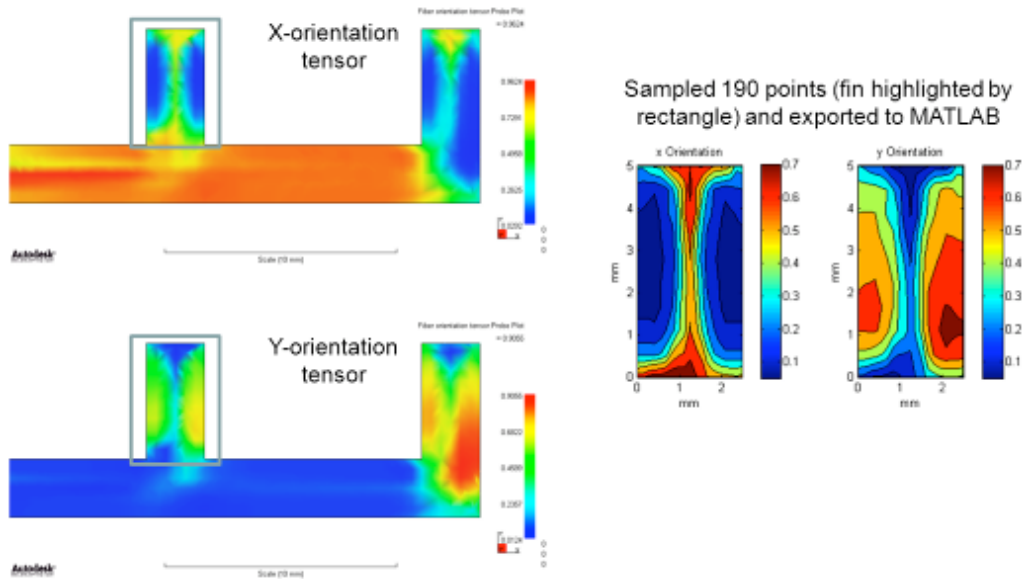


Figure 1. X- and Y-orientation tensor (Moldflow nodal values shown on left, sampled points shown on right).

The x- and y-tensor values were again translated into thermal conductivity using Nielsen's model. The new thermal conductivity maps conserve the trends observed in the tensor maps, with high y-values (orientation tensor or thermal conductivity) close to the vertical walls, and low y-values in the core (away from the walls), as shown in Figure 2. The converse is true for the x-values of orientation tensor or thermal conductivity.

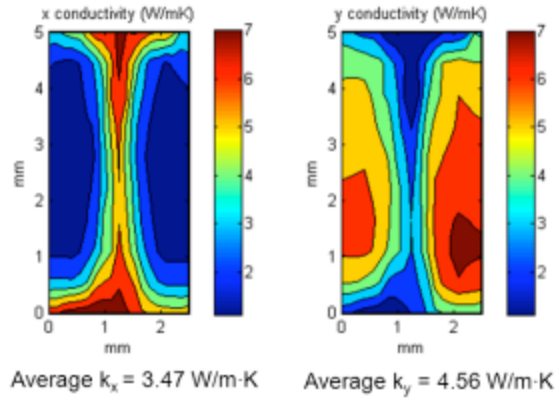


Figure 2. X- and Y- thermal conductivity maps (average of all values shown below each plot).

These refined maps of thermal conductivity were used in ANSYS to perform thermal simulations in a 2D fin with a constant temperature condition at the base and convective boundary conditions at the walls and tip. The nodal temperature results confirmed the strong two-dimensional character that was previously noted, especially in the thru-thickness temperature variations. For a low heat transfer coefficient of 50 W/m²K, the fin temperature varied by 1 to 2 K through the thickness of the fin, while for a higher heat transfer coefficient of 1000 W/m²K, the temperature varied by 8 to 9 K.

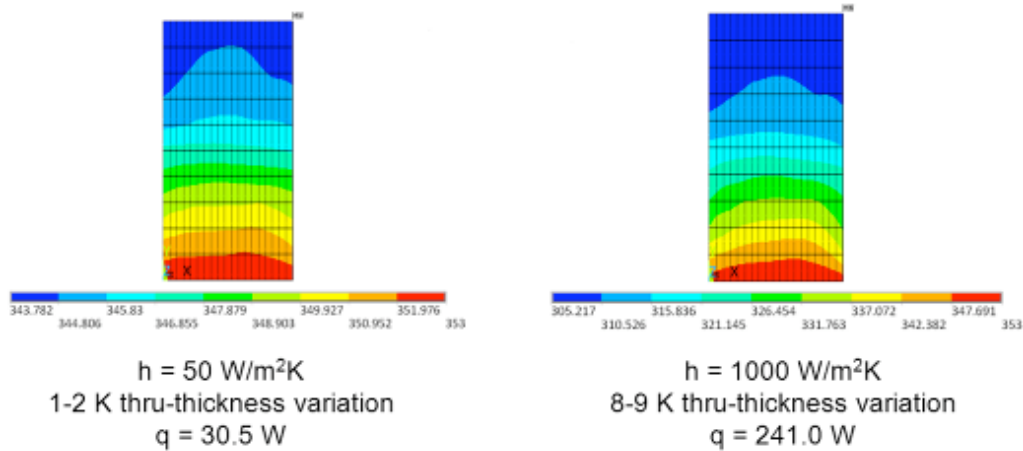


Figure 3. Temperature distribution for anisotropic fin ($t_f=2.5\text{mm}$, $H=5\text{mm}$, $\theta_b=55\text{K}$, $T_{\text{amb}}=298\text{K}$).

The heat transfer rate through the base of the fin was also calculated in ANSYS for varying convective boundary conditions. The heat transfer coefficient was varied from 50 to 1000 W/mK. These results were used in the one-dimensional fin equation in order to extract an effective thermal conductivity (see Table 1), one with which a fin would provide the same heat transfer rate under the same boundary conditions. The results revealed that an average effective conductivity of 3.91 W/m-K would predict the heat transfer rate in the range of heat transfer coefficients studied with errors of less than 0.5%.

Table 1. Effective thermal conductivity (calculated from 1D fin equation)

h (W/m²K)	q ANSYS (W)	k from fin eq. (W/m·K)
50	30.5	3.88
100	55	3.91
200	93.1	3.93
300	122.4	3.94
400	146.3	3.94
500	166.7	3.93
600	184.5	3.93
700	200.6	3.92
800	215.1	3.9
900	228.5	3.89
1000	241	3.88
	Average	3.91
	Std. Dev.	0.023

It was also observed that the averages of the x- and y- conductivities could be combined into a single average that is very close in value to the extracted effective conductivity (3.91 W/m·K) from the ANSYS results, especially the harmonic mean of the average conductivities, as shown in Table 2 below.

Table 2. Mean thermal conductivity (calculated using $k_x=3.47$ W/m·K and $k_y=4.56$ W/m·K)

	(W/m·K)
Arithmetic mean	4.02
Geometric mean	3.98
RMS	4.05
Harmonic mean	3.94

Even though the fin under study had marked variations in thermal conductivity across its area, the x- and y- averages were very close to each other ($k_x=3.47$ W/m·K, $k_y=4.56$ W/m·K). A case in which these averages are further apart in value will be useful to determine the effectiveness of using an average thermal conductivity to calculate the thermal performance of a composite fin.

II. Develop and use thermomechanical finite element model to assess thermal and structural performance of polymer composite heat exchanger, and assessed feasibility of replacing metallic heat exchangers at the Das Island liquefied natural gas facility with polymer composite heat exchangers

Purpose

Modeling of fiber-reinforced polymers is more challenging than modeling metals due to the inherent anisotropy that results from fiber orientation in the matrix. Elastic modulus, yield strength and thermal conductivity are as much as two orders of magnitude higher in the direction of fiber alignment. Thus, finite element models must be very refined to capture the effects of the anisotropy.

The mechanical finite element model was refined to capture anisotropic effects resulting from structural loading. The ability to apply thermal loads and quantify the resultant stress and temperature distributions was incorporated into the enhanced thermomechanical finite element model.

Verification of thermal modeling based on laboratory prototype polymer composite heat exchanger

The thermomechanical model was designed to emulate the laboratory prototype polymer composite heat exchanger because empirical data was available to calibrate from the laboratory prototype. The empirical data allowed for the calibration of the thermomechanical finite element model.

The heat transfer rate of the thermomechanical finite element model using various heat transfer correlation and fluid temperature profile methods was compared with the heat transfer rate of the laboratory prototype polymer composite heat exchanger to ensure similarity. It was found that modeling the local heat transfer coefficient and local fluid temperature profile resulted in the greatest finite element model accuracy. Empirical and numerical heat transfer rates agreed within the uncertainty of the empirical values, which was 13.2%. The air and water heat transfer coefficients and temperatures can be found in Figures 4 and 5, respectively.

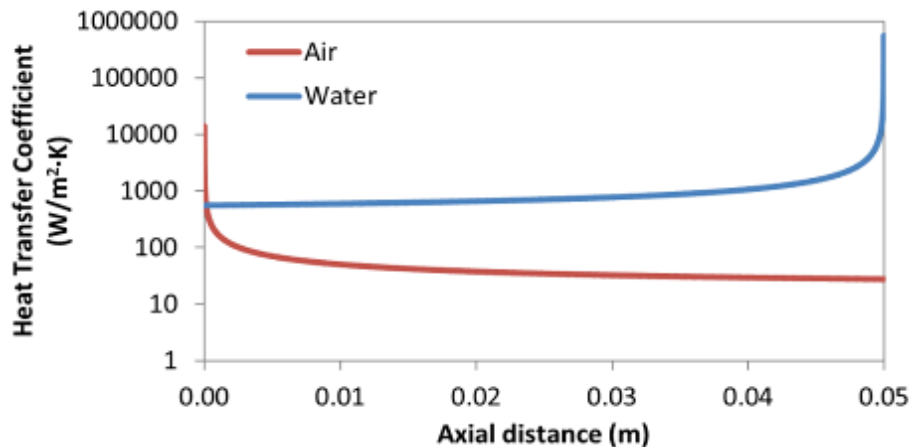


Figure 4. Fluid heat transfer coefficients in thermomechanical model.

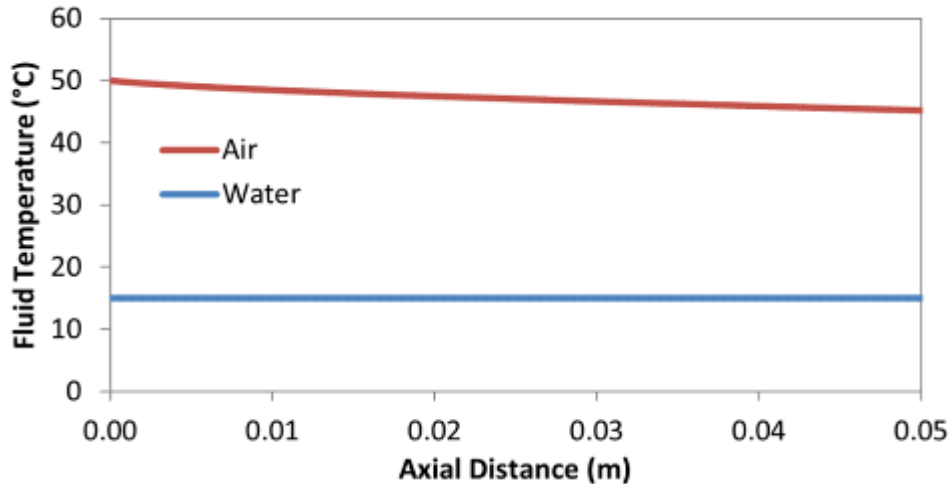


Figure 5. Fluid temperatures in thermomechanical model.

Comparison of thermal performance of composite heat exchanger with heat exchangers made from conventional corrosion resistant materials

The heat transfer rate was predicted for heat exchangers made from a polymer composite, titanium and polytetrafluorethylene, three corrosion-resistant heat exchanger materials. The results are shown in Figure 6. It was found that at ambient pressure, the airside convection thermal resistance dominated the total thermal resistance, but at higher fluid pressures with the same fluid velocity, the airside thermal resistance became less dominant, limiting the performance of the composite heat exchanger relative to the titanium one. At an airside pressure of 100 kPa, titanium outperformed the composite by 43%; at an airside pressure of 500 kPa, titanium was 103% better and at an airside pressure of 5000 kPa, titanium was 256% better in terms of heat transfer rate. The air inlet temperature had less effect on relative performance of the heat exchanger materials.

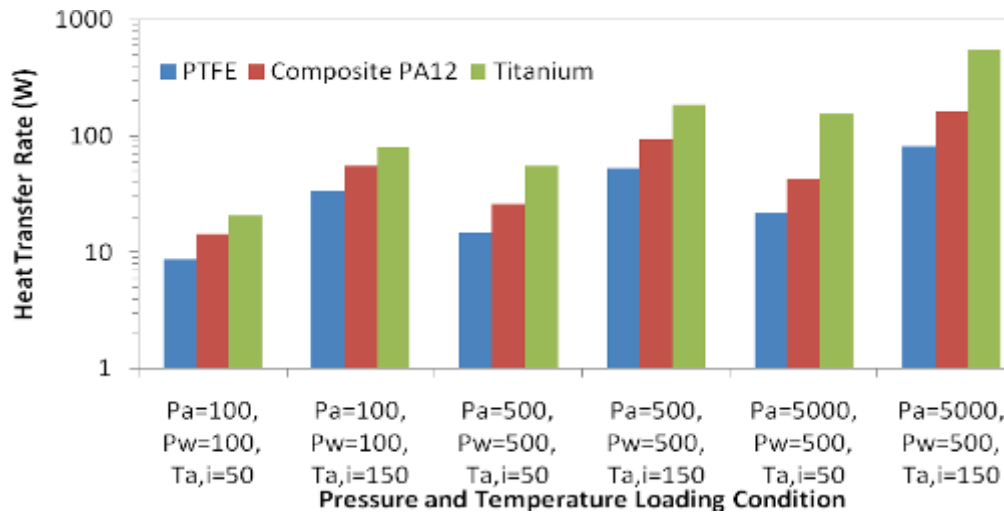


Figure 6. Heat transfer rate as a function of fluid parameters and heat exchanger material (Units: kPa, °C).

It is noteworthy that although the titanium heat exchanger outperformed the composite heat exchanger, the low-cost, low-weight and low embodied energy of the composite remained

attractive. Furthermore, the current calculations assume a through-wall conductivity of only 0.65 W/m-K, which is the minimum conductivity according to the Nielson equation. In reality, the through-wall conductivity will be higher, and thus higher heat transfer rates will be achieved.

The enhanced heat transfer performance of the titanium heat exchanger relative to the polymer composite one can be partially attributed to better spreading. In the titanium heat exchanger, the high z-direction conductivity allows for spreading, whereas the low z-conductivity in the polymer composite limits performance (the z-direction experiences little conductivity enhancement due to the fibers not being aligned in this direction). The temperature profiles of each heat exchanger are shown in Figure 7.

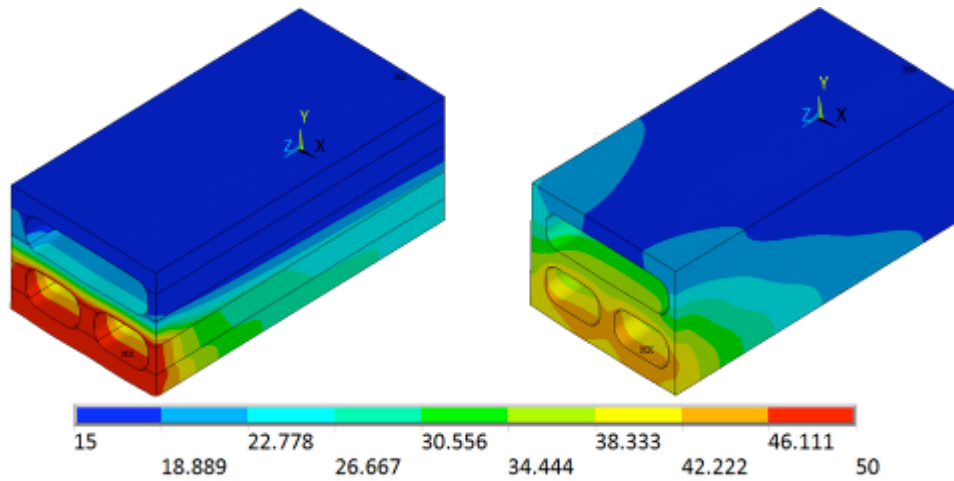


Figure 7. Temperature distributions of polymer composite (left) and titanium (right) heat exchangers (Units: °C).

Analysis of combined thermomechanical stresses in polymer composite heat exchangers

The directional stresses resulting from the combined thermomechanical loading of polymer composite heat exchangers were found to be highly temperature dependent. The directional stresses resulting from six loading scenarios are shown in Figure 8.

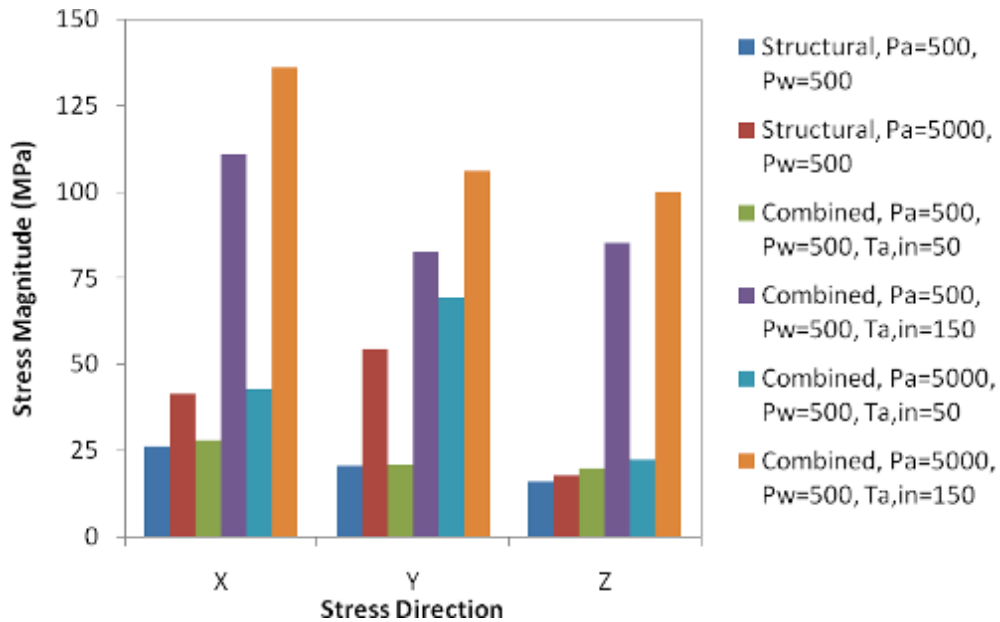


Figure 8. Direction stress magnitudes resulting from various thermomechanical loadings (Units: kPa, °C).

The directional stress results show that stress magnitude is a function of the airside inlet temperature assuming the waterside inlet temperature remains 15°C. Although the stress magnitudes increase when the airside pressure increases from 500 kPa to 5000 kPa, the increases are much smaller than those seen when increasing the airside fluid temperature from 50°C to 150°C at constant pressure. These results show that while stresses resulting from pressure loading are largely a function of geometry, stresses resulting from thermomechanical loading are largely a function of discontinuity in material properties.

Figure 9 shows the x-direction stresses resulting from airside and waterside pressures of 500 kPa and an airside inlet temperature of 150°C. Stress concentrations occur at the interface between the fins and plates due to the discontinuity in material properties at these interfaces. It is noteworthy that injection molding will result in a gradual transition in material properties, which means that the stress concentrations shown will be much lower in magnitude in reality.

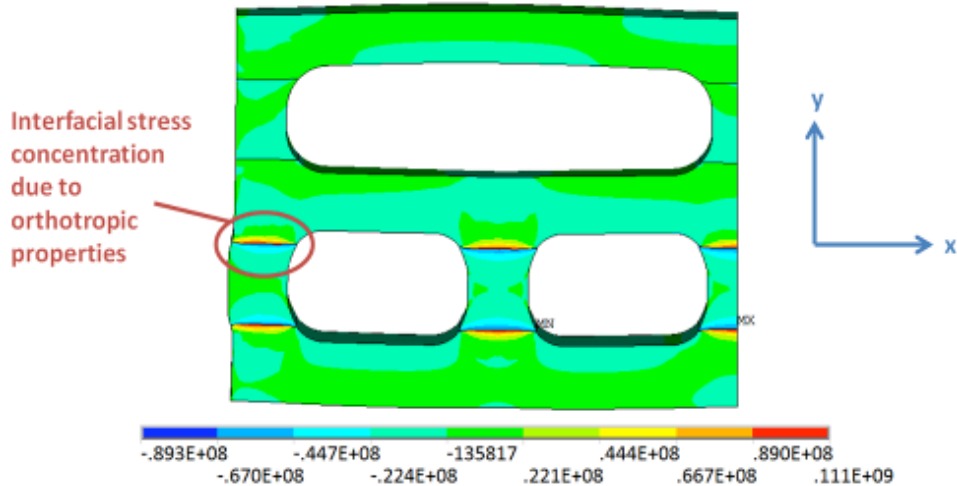


Figure 9. X-direction stress distribution resulting from orthotropic material properties (Units: Pa).

III. *Develop accurate mold-filling metamodel using advanced datapoint selection methodology*

- a. **Motivation:** The development of a mold-filling metamodel is important to the processes of design exploration and optimization of thermally-enhanced polymer heat exchangers. The computationally expensive nature of mold-filling simulation necessitates the development of a mold-filling metamodel, but using traditional methods to design the experiments to develop an accurate model would require an extensive collection of simulations and is therefore infeasible.
- b. **Action Plan:** An advanced datapoint selection methodology is used to create a mold-filling metamodel with minimal simulations
- c. **Findings:** The design space is divided into two regions: feasible and infeasible designs. If the feasibility boundary that divides these two regions can be accurately identified, a model can be developed that accurately classifies candidate designs as feasible or infeasible. An algorithm known as the feasibility boundary search algorithm was developed for locating this boundary with a defined level of accuracy while using minimal simulations. An overview of the steps making up the algorithm is presented below and shown in Figure 10.
 1. Define transition response value for which the design space will be divided into feasible and infeasible subspaces.
 2. For a problem of n variables, construct a grid of $n-1$ dimensions for which the algorithm will then find the location of the feasibility boundary in the remaining dimension at each grid location.
 3. Find seed point on feasibility boundary at initial grid location. The search process used to find this point and all points on the feasibility boundary is called the transition point search algorithm and is shown below.
 4. Using adaptive search methods, predict the location of the next transition points and the ideal search parameters to find them based on previously found transition points.

Adaptive proportional control is used to determine the search control parameters that would have led to immediate convergence in order to improve the search efficiency at the next set of transition points. A more precise initial guess is determined using extrapolation from previously found points in order to further improve convergence speed at the next transition points.

These methods reduce the amount of search iterations required to find points on the feasibility boundary and therefore reduce the overall number of simulations needed to create the metamodel.

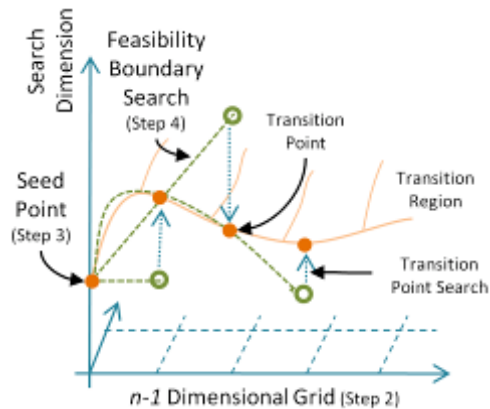


Figure 10. Overview of feasibility boundary search algorithm.

Transition Point Search Algorithm: Shown in Figure 11, the transition point search algorithm is used to find the transition point in minimally computationally expensive simulations with a defined level of accuracy. The algorithm begins with an initial guess and then applies proportional control based on the error relative to the feasibility transition value. Then linear interpolation is applied, followed by quadratic interpolation until the transition point is found. In order to improve the efficiency of the search process, the initial guess and proportional control constant are supplied by the feasibility boundary search algorithm based on previous transition point searches and their resulting transition points.

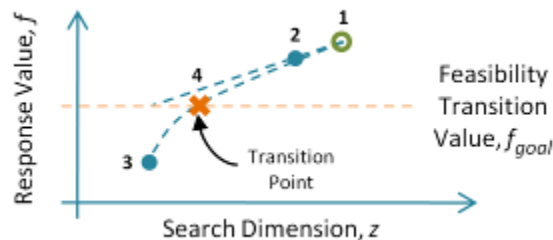


Figure 11. Transition point search algorithm.

The plate-fin heat exchanger design, the cross-section of which is shown in Figure 12, was used for this experiment. The design dimensions are shown in Table 3, and the material investigated is shown in Table 4.

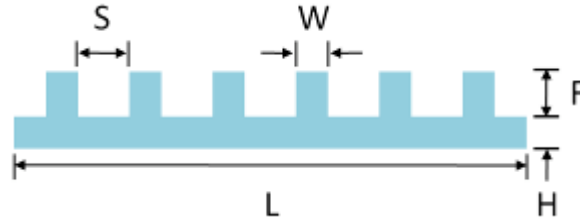


Figure 12. Plate fin design.

Table 3. Design dimensions

Design Variable		Min	Max	Grid Spacing
Base Length	L, mm	200	700	100
Base Thickness	T, mm	1	5	Varying
Fin Width	W, mm	1	5	1
Fin Height	H, mm	10	10	Fixed
Fin Spacing	S, mm	3	15	3

Table 4. Material properties for selected material

Material	Resin	Thermal Conductivity, W/m-K	Tensile Strength, MPa
PolyOne NJ-6000 TC Black	PA 12	10	110

Based on the above described feasibility boundary algorithm, a set of simulations was conducted to create a mold-filling metamodel. A feasibility transition value of 90% filled and a desired accuracy defined as $\pm 1\%$ filled were used as the goal of the feasibility boundary search algorithm. Over the design space of 150 grid locations, 804 simulations were required to define the transition region, with an average of 5.4 search iterations per transition point, as shown in Table 5. In order to match the achieved level of accuracy with alternative methods using either exhaustive search or binary search in order to find the transition points, it would have required 300,000 or 1,645 simulations, respectively.

Table 5. Comparison of developed method and exhaustive and binary search methods

Method	Avg. Search Iterations Per Transition Point	Total Function Evaluations	Factor Relative to Developed Method
Exhaustive Search	2000	300,000	373.13
Binary Search	10.97	1,645	2.05
Developed Method	5.4	804	

A series of randomly selected test heat exchanger designs was used to test the accuracy and robustness of the developed model. The developed model successfully classified all 50 test designs into their respective feasible or infeasible subspaces. The developed algorithm was therefore successful in creating an accurate mold-filling metamodel while collecting minimal simulations.

This work was submitted to the 2011 ASME International Design Engineering Technical Conference.

IV. Develop new image processing methodology for identifying fibers in microscope images of sample heat exchanger geometry

Motivation: While the previously developed image processing methods provided some understanding of the fiber orientation present in microscope images, more detailed information was required in order to develop an accurate representation of the fiber orientation in sample geometries.

Action Plan: Develop an image processing method that accurately identifies fibers in microscope images of sample geometry and provides more detailed information on the fiber orientation of the identified fibers.

Findings: Using the advanced image processing framework OpenCV, an image processing program was constructed with C++ for analyzing collected microscope images. This program uses threshold and morphological operations to isolate fibers from the surrounding polymer matrix. Geometric methods are then used to identify individual fibers in the image. Orientation and fiber length are then extracted from the geometric features and overall features such as fiber density can be determined.

The previous image processing method used statistical information to estimate the distribution of fiber orientation in the sample. The new method identifies individual fibers in the sample and therefore provides an exact representation of the distribution of fiber orientation. This dramatically improves the accuracy of the measured fiber orientation values and therefore provides a better comparison to estimated values.

V. Develop a technique for characterizing mixing of polymer composites in a TSE

During mixing processes for creating polymer composites by combining fiber fillers in polymers, such as Twin Screw Extrusion (TSE), the distribution of fiber fillers depends on the shear forces associated with the mixing process. In this task, we use Calibrated Microencapsulated Sensors (CAMES) beads to trace the shear forces generated in the mixing process. CAMES beads are designed to measure shear stress during mixing by breaking at a specific critical stress level, which is dependent on the bead diameter, and releasing a dye (Red B Disazo) that can be optically measured. The selected range of diameters for the experiment was 53 - 63 μ m.

As a model polymer for the polymer composites being used for PHXs, a high-density polyethylene (HDPE) Alathon H6018 in pellet form from Equistar Chemicals was used in this investigation to calibrate the technique. The HDPE used in this study had a density of 0.960 g/cc and a melt index of 18.0 g/10 min.

In order to ensure that the stress beads would break in the designed operating region, viscosity data were generated using a Rheometrics RDA-III rheometer and the results plotted in Figure 13.

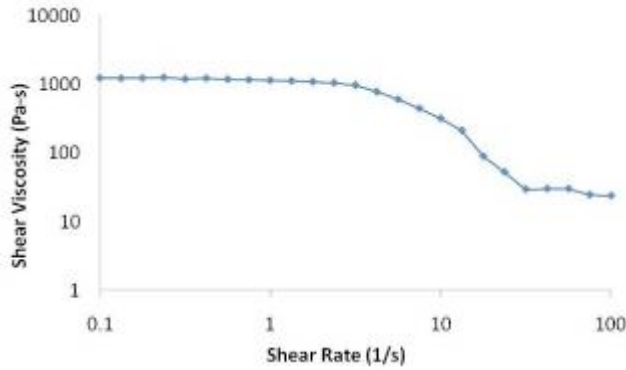


Figure 13. Shear viscosity for HDPE at 160°C.

Furthermore, the slope of this graph was used to calculate the shear stress by using the equation:

$$\tau = \eta \dot{\gamma}^{(n+1)/n} \quad (1)$$

where τ is shear stress (Pa), η is viscosity of the polymer (Pa-s), $\dot{\gamma}$ is shear rate (1/s), and n is the slope. The shear rate is defined as:

$$\dot{\gamma} = \frac{\pi ND}{h} \quad (2)$$

where N is screw speed (rpm), D is the screw diameter (mm), and h is the channel height (mm).

Using the dimensions of the 28-mm conveying element that has a channel height of 4-mm, the stresses induced at each operating screw speed were evaluated and are displayed in Table 6.

Table 6. Calculated shear stress

Screw Speed, N (rpm)	Shear Stress, τ (Pa)
40	101.9
75	123.7
110	148.4
145	181.6
180	193.3

The approximate critical stress value at which the CAMES beads break at was 120 Pa, using data obtained from MACH I. Table 6 shows that, for the given range of screw speeds, the amount of bead breakup would occur at a low level for the lower screw speeds and increase at the highest speeds.

To calculate the percent break up of CAMES beads, the areas under the RTD and RSD curves were determined, and the following equation was used to calculate the percentage of beads broken:

$$\text{Percent Breakup} = \frac{A_c}{A_r} \times 100\%$$

where A_c is the area under the CAMES RSD curve and A_r is the area under the ink RTD curve.

Percent breakup generated from screw configuration 1 (i.e. wide kneading blocks) is presented in Figure 14.

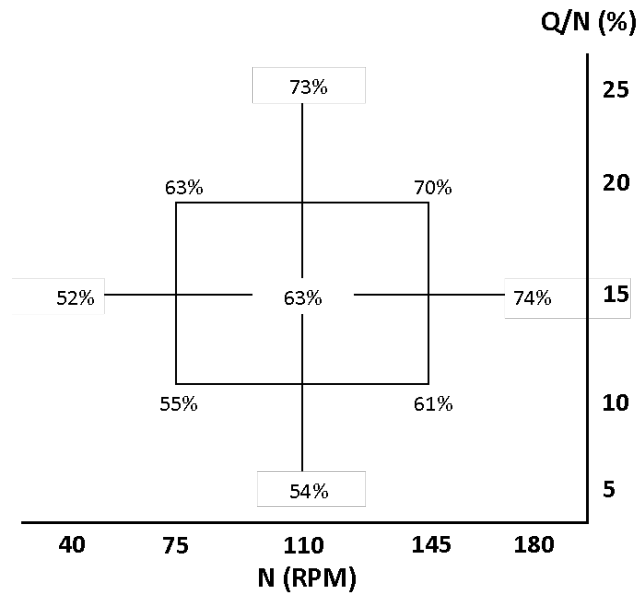


Figure 14. Percent breakup using wide kneading blocks.

Figure 14 presents the percent breakup for the wide kneading block configuration and indicates that there are trends within the data as a function of screw speed and specific throughput. As screw speed increases for a given Q/N, the percentage of broken beads also increases. This is expected, as shear rate increases as screw speed also increases, as given by Equation (2). Another noticeable trend in the data is percent breakup of beads increases as specific throughput increases. As the specific volume of material in the channel increases, the pressure on the melt while inside the kneading blocks also increases, inducing higher levels of stress on the beads.

Average percent breakup was calculated using the narrow kneading blocks screw design (screw configuration 2) and inserted in the CCD grid as shown in Figure 15.

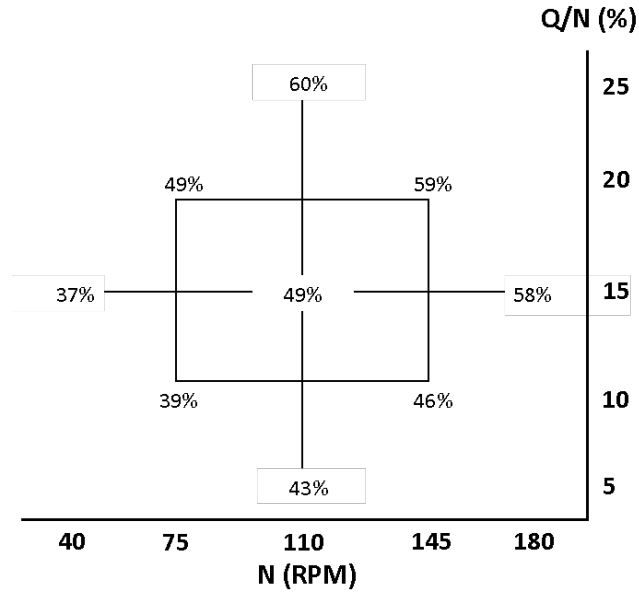


Figure 15. Percent breakup using narrow kneading blocks.

Figure 15 above shows similar trends within this data to that of Figure 14. Again, it can be seen that increasing N and Q/N yields a higher percent breakup.

Comparing the two average percent breakup grids (Figure 14 and Figure 15), it is apparent that screw configuration 1 (wide kneading blocks) broke up a larger percentage of CAMES beads than in the narrow kneading blocks configuration. This result is consistent with the common understanding that the wide kneading blocks are better for dispersive mixing due to the wider paddles and the higher extensional flows. The narrow kneading blocks are commonly described as better for distributive mixing, as confirmed by the lower stress levels.

To confirm that the range of obtained breakup was outside of experimental error, an error analysis was performed on both sets of data. It was determined that there is approximately a 2% error for both wide and narrow kneading blocks. This provides validation that the range of percent breakup is independent of experimental error and that there is in fact a significant increase in percent breakup as N and Q/N are increased.

Residence time and stress distribution curves were generated from the data acquisition program and plotted together for each condition. Figure 16 displays the RTD and RSD curves for a given operating condition using the wide kneading blocks configuration.

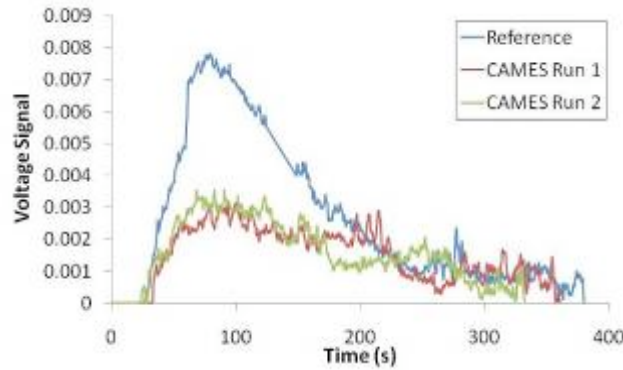


Figure 16. Normalized wide kneading blocks RTD and RSD curves for .236/110 condition.

Figure 16 shows the normalized RTD and RSD curves generated by the dye and CAMES shots, respectively. This figure shows the quality of the data collected by each individual run, which validates the claim that the feed method did not affect the output curves. The two RSD curves are essentially identical to each other, demonstrating the experimental repeatability. The curves also show that the CAMES beads are passive tracers, following identical paths in the extruder as described by the RTD. Upon inspection, it is clear that the RTD curve has higher amplitude than the RSD curves, indicating that 100% breakup of the CAMES beads was not achieved.

Since the residence distribution is the time history through the screw's geometry, it can be viewed as the history of the flow path through the mixing zone. The dye that comes through first transverses the least tortuous path, staying in the center of the channels, whereas the tail of the distribution passes back through the paddles. The difference in the RTD and RSD curves confirms that description. Initially the percentage of the flow that experiences the critical shear stress is a small percentage of the total flow, whereas the figure does indicate that at the tail end of the curves, the majority of CAMES beads did break during this segment as the RTD and RSD curves overlap.

The RTD and RSD curves generated using the narrow kneading blocks are plotted in Figure 17.

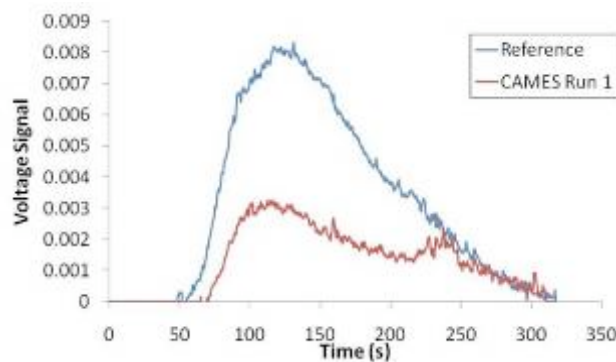


Figure 17. Normalized narrow kneading blocks RTD and RSD curves for .236/110 condition.

The comparison of the RTD and RSD curves for the narrow kneading blocks configuration follows the same pattern as the wide kneading blocks where the initial part of the flow experiences little of the critical stress, whereas all of the flow in the tail of the RSD experiences the critical stress. The one difference is there is a lag time between the start of the RTD and the RSD. This can be interpreted as the initial part of the RSD experiencing little to no shear stress until about 20% of the RTD is complete.

4. Difficulties Encountered/Overcome

- Not enough fiber filled nylon can be obtained quickly enough
- Looking at obtaining fiber-filled PPS for better thermal properties

5. Planned Project Activities for the Next Quarter

- Manufacture prototype of new candidate PHX design using a thermally enhanced polymer, and test prototype in upgraded experimental test rig.
- Apply the improved image processing algorithm to a variety of heat exchanger geometries and processing parameters to examine the effectiveness of Moldflow® fiber orientation predictions.
- Complete the study of model simplification techniques for simulating mold-filling of plate-type geometries and develop guidelines for when such methods are suitable.
- Vary geometric parameters (e.g., number of gas side fins, number of waterside fins, fin height, fin thickness, plate thickness) to assess their effect on stress and temperature distributions of orthotropic heat exchanger models.
- Utilize injection mold filling software to approximate full anisotropic structural and thermal material properties and compare the results of this anisotropic model with those of the orthotropic model to ensure similitude
- Apply new characterization technique for mixing in a TSE to Fiber Filled Nylon for PHXs.

Appendix

Goals

The goal of the proposed 3-year EERC II polymer composite heat exchanger (PCHX) project is to develop the science and technology needed to underpin the systematic design of polymer-fiber composite heat exchanger modules that address the needs of the fossil fuel industry. The project team, lead by A. Bar-Cohen, brings together expertise in thermal science and technology (Bar-Cohen, Rodgers) with polymer composite molding and manufacturing (Gupta, Bigio). Design studies and molding simulations, as well as fabrication and testing of laboratory-scale polymer composite heat exchangers, during the first phase of this project, have provided the foundation for aggressive pursuit of such polymer composite heat exchangers.

Successful development of cost-effective, high-performance PCHX's will require a detailed understanding of the limitations imposed on the thermal performance, mechanical integrity, and cost of such heat exchange devices by the candidate polymer material; carbon fiber geometry, orientation, and concentration; thermal and mechanical anisotropy of the polymer-fiber composite; molding processes; thermal and structural failure mechanisms in the molded heat exchanger; and the energy investment in the fabrication and formation of the heat exchangers. The development and experimental as well as numerical validation of a multi-disciplinary computerized design methodology, along with the fabrication and testing of scaled polymer heat exchanger modules, would provide a unique knowledge-base from which low-life-cycle-cost heat exchange systems for the petroleum and gas industries could be developed.

Project Tasks

A. Thermal Design and Characterization of Polymer Composite Heat Exchanger Module (Prof. Avram Bar-Cohen - UMD, Prof. Hugh Bruck- UMD, Prof. Peter Rodgers – PI)

- 1. Design and thermofluid evaluation of PHX concepts for LNG applications**, including sensitivity of thermal performance to key parameters, quantification of primary thermal and exergy figures-of-merit (metrics), comparison to conventional heat exchangers, and identification of least-mass/least-energy designs;
- 2. Detailed design, fabrication, and thermal characterization of least-energy PCHX module**, including mold fabrication for most promising design, assembly and instrumentation of laboratory prototype, analysis of thermal and structural performance under simulated LNG processing conditions;
- 3. Development of predictive models for anisotropic heat exchanger modules**, including use of molding CFD software for prediction of fiber orientation and effective thermal/ structural properties, numerical and analytical models for molded anisotropic fins, derivation of least-material anisotropic fin equations, determination of heat flow sensitivity to fiber geometry/concentration/orientation;
- 4. Evaluation of convective enhancement features in molded channels**, including identification of “best practices” in conventional heat exchangers, manufacturability analysis of candidate features with attention to mold complexity, part ejection, and warpage, polymer composite molding of 3-5 candidate enhanced channels; thermofluid characterization of candidate enhanced channels under simulated LNG processing conditions; and
- 5. Determination of seawater effects on polymer composite finned plates**, including design and molding of test samples, immersion in saltwater tanks at different temperatures and concentrations for pre-determined periods, surface/bulk imaging and mechanical characterization before and after immersion, analysis and correlation of effects.

B. Manufacturability Analysis and Mold Design for Polymer Composite Heat Exchanger Module (Prof. SK Gupta – UMD, Prof. HA Bruck - UMD)

1. Development of an improved meta-model for mold filling predictions: We plan to develop an improved meta-model for predicting mold filling for typical heat exchanger geometries. This meta-model will account for multiple gates with adjustable spacing. The data for developing this meta-model will be generated using mold flow simulations. We plan to utilize radial basis function based meta-models to provide the right balance of accuracy and computational speed.

2. Creation of a computational framework for gate placement to optimize fiber orientation: We plan to develop a computational framework for placing gates to optimize the fiber orientation, utilizing simulated fiber orientations to select the gates. The sensitivity of the gate locations on fiber orientation will be developed. Gradient-based optimization techniques will be used to optimize the fiber orientation. The optimization problem will incorporate the constraint satisfaction formulation of the weld-line locations to ensure that the fiber orientation formulation produces acceptable weld-lines.

3. Generation of insert molding process models to incorporate connectors at the weld-lines: In order to ensure that the weld lines do not compromise the structural integrity, we plan to embed metal connectors at the expected weld-lines locations. In order to accurately place these metal connectors in the structures, we plan to develop process models of the insert molding process and mold design templates for performing insert molding.

4. Develop key relationships for the dependence of fiber orientation on the flow geometry of the finned-plate PCHX module, in commercially available polymer composites, including the effect of carbon fiber length and diameter, for high and low fiber concentrations, for both base plate and fin passages in the mold, and the effect of fiber orientation/distribution on thermo-mechanical properties, verify relationships with suitable small scale experiments;

C. Polymer-Fiber Interactions in Polymer Composite Heat Exchanger Modules (Prof. David Bigio – UMD)

1. Determine achievable thermo-mechanical property enhancement through control of carbon fiber orientation, in the commercially available polymer composites, with attention to flow regimes, mixing processes in the flow of the melt, and heat exchanger module design, and verify experimentally;

2. Explore optimization of PCHX polymer composite properties through the creation of novel polymer composite compositions, including multi-scale filler geometries, develop the molding methods for the desired geometries, create the novel composites and experimentally verify improved thermo-mechanical polymer composite properties.

References

- [1] Bar-Cohen, A., Luckow, P., Cevallos, J.G., Gupta, S.K., 2010, Thermal Anisotropy in Injection Molded Polymer Composite Fins, International Heat Transfer Conference 14 at Washington DC
- [2] Cevallos, J.G., Gupta, S.K., Bar-Cohen, A., Incorporating Moldability Considerations during the Design of Thermally Enhanced Polymer Heat Exchangers (under revisions)
- [3] Cevallos, J.G., Bar-Cohen, A., Bergles, A.E., Gupta, S.K., Rodgers, P., Polymer Heat Exchangers – History, Opportunities, and Challenges (in progress)
- [4] Luckow, P., A. Bar-Cohen, P. Rodgers, 2009, “Minimum Mass Polymer Seawater Heat Exchanger for LNG Applications,” accepted for publication, ASME TSEA, January 2010
- [5] Cox, H.L., 1951, “The elasticity and strength of paper and other fibrous materials,” Brit. J. Appl. Phys., 3(3), pp. 72-79.

- [6] Amado-Becker, A., Ramos-Grez, J., Yanez, M.J., Vargas, Y., and Gaete, L., 2008, "Elastic tensor stiffness coefficients for SLS Nylon 12 under different degrees of desensification as measured by ultrasonic technique," *Rapid Proto. J.*, 14(5), pp. 260-270.
- [7] Halpin, J.C., and Kardos, J.L., 1976, "The Halpin-Tsai Equations: A Review," *J. Poly. Eng. and Sci.*, 16(5), pp. 344-352.
- [8] Hahn, H.T., and Tsai, S.W., 1980, *Introduction to Composite Materials*, Technomic Publishing Co., Lancaster, PA.
- [9] Pegoretti, A., Fambri, L., Zappini, G., and Bianchetti, M., 2001, "Finite element analysis of a glass fibre reinforced composite endodontic post," *Biomaterials*, 23, pp. 2667-2682.
- [10] Fu, S., and Lauke, B., 1997, "The elastic modulus of misaligned short-fiber-reinforced polymers," *Comp. Sci. and Tech.*, 58, pp. 389-400.
- [11] Foye, R.L., 1972, "The Transverse Poisson's Ratio of Composites," *J. Comp. Mater.*, 6(2), pp. 293-295.
- [12] "Thermal Graph DKD," Cytec Industries, Accessed 26 May 2010, <http://www.cytec.com/engineered-materials/products/cfThermalGraphDKDX.htm>.
- [13] Robinson, F., Bruck, H., Gupta, S.K., and Bar-Cohen, A., 2010, "Saltwater Hygrothermal Aging Studies of Short Carbon Fiber Reinforced Polyamide 12," ASME International Mechanical Engineering Congress & Exposition, Vancouver, British Columbia, Canada, November 12-18, 2010.

Microchannel-Based Absorber/Stripper and Electrostatic Precipitators for CO₂ Separation Processes

UMD Investigators: Serguei Dessiatoun, Amir Shooshtari, Michael Ohadi

GRAs: Radoslaw Kuzmicki, Arndt-Magnus Herzog

PI Investigators: Afshin Goharzadeh, Mohamed Alshehhi

Start Date: Oct 2006

1. Objective/Abstract

This project is focused on research leading to the development of a high-efficiency CO₂ separation mechanism with application to a diverse range of processes in the oil and gas industry, including CO₂ separation separation/injection in petrochemical and refining processes, gas sweetening, and CO₂ capture for enhanced oil recovery applications.

The removal of acidic gases such as carbon dioxide from gas streams is an important process in the natural gas industry. In gas sweetening at least 4% by volume of raw natural gas consists of CO₂ which needs to be lowered to 2% to prevent pipeline corrosion, to avoid excess energy for transport, and to increase heating value. The separation of CO₂ from flue gases and its use for enhanced oil recovery and CO₂ sequestration applications is an increasing area of importance, as evidenced by the large investments in this area by ADNOC and its group companies, as well as affiliated government agencies in Abu Dhabi. A typical CO₂ separation process involves three stages: cooling down the flue gas; separating the solid particles and condensed water droplets; and finally capturing the CO₂ using the absorption process. The microchannel-based CO₂ separator being developed in this project will significantly increase controllability of the thermal state of the reaction and the efficiency of the separation process while decreasing the reaction time and energy consumption, as well as potential substantial reduction of equipment footprint and the associated capital investment.

Flue gas also usually contains many contaminants in solid and liquid forms, the bulk of which are separated in gravity and inertia-driven feed gas separators. However, fine particles are carried on with the flow and can damage compressors, contaminate the gas absorption process, and reduce the quality of gas products. Electrostatic separation is one of the most effective techniques for separation of such particles and will be used in this project. The present project will address separation of droplets and particles using an EHD gas-liquid separation technique to remove liquid particles suspended in a moving gaseous medium, followed by the proposed micro channel-based separation of the CO₂ from the stream once the fine particles in the flow have been removed.

The project is being conducted jointly by the team at UMD and at PI. The team at PI is focusing on EHD separation process and absorption modeling, while the team at UMD has focused on the experimental work utilizing microchannel-based CO₂ separation and the absorption solution.

2. Executive Summary of Accomplishments in the Current Reporting Period

During this reporting period additional in-depth study of the processes and analysis of our experimental results contributed to our collective enhanced understanding of the physics and reaction kinetics. The team effort advanced on two fronts, mathematical modeling and experimental study. The main focus of the collaborators at the Petroleum Institute has been in mathematical modeling of the absorption process in microchannels, and during this period considerable success in development of the model has been achieved. The team currently is

focusing on improving the modeling capabilities and implementing the complicated absorption physics and the chemical reaction more in-depth.

On the other hand, the focus of collaborators at UMD has been on the experimental study of the process and the visualization study of the absorption of CO₂ in microchannels. During this period, the experimental setup was revised and new set of data was collected. The phenomenon was also successfully demonstrated in a test channel, and the performance was quantified. Some of the major results collected in this period and the outline of the future work are presented in current report.

In this reporting period, the collaborators from the PI and UMD continued on joint review of the project and shared ideas through biweekly video conferences and exchange of emails. The project has been strengthened also from addition of Dr. Kyu Yong Choi, a professor in chemical engineering, with extensive background and expertise in chemical reaction. Some experiments repeated by the new intern working on the project demonstrate good repeatability of experiments.

3. Milestones/Deliverables Scheduled for the Completed Quarter

- Improved experimental setup
- Collected new set of data
- Improved model
- Performed experimental study of absorption of CO₂ in a single microchannel reactor

4. Summary of Project Activities for the Completed Quarter

A thorough literature review has been conducted as introductory work by the new research assistant, Arndt-Magnus Herzog, to be well prepared for the coming work. In this connection the advantages of microchannel reactors were gathered. These are a high surface-volume ratio, small dimensions, small diffusion path and precise control of important parameters, such as the temperature.

With respect to these advantages some calculations were made to obtain a value for the surface-volume ratio of the used microchannel reactor.

Surface-volume ratio of used microchannel reactor

$$a_v = \frac{A}{V}$$

a_v := surface – volume ratio
A := inner surface of reactor
V := inner volume of reactor

$$A = \pi * d * l$$

d := inner reactor diameter
l := length of reactor

$$V = \frac{d^2}{4} * \pi * l$$

Combining these two equations yields

$$a_v = \frac{\pi * d * l}{\frac{d^2}{4} * \pi * l}$$

This solves in:

$$a_v = \frac{4}{d} \left[\frac{m^2}{m^3} \right]$$

$$a_v = \frac{4}{0.00075} = 5,333.33 \left[\frac{m^2}{m^3} \right]$$

A Rashig ring with an outer diameter of 2 mm has a surface-volume ratio of $a_{v,R} = 94 \left[\frac{m^2}{m^3} \right]$ (http://www.pyrotek.info/documents/datasheets/808_-_Carbon_Raschig_Rings_-_E4.pdf). If we now compare these two values, the surface-volume ratio of the micro-channel reactor is 56.74 times higher.

Experimental setups

The entire experimental setup is presented in Figure 1. The syringe pump drives a precise amount of DEA solution to the microchannel reactor. The CO₂ gas is derived from a pressurized gas cylinder. The flow rate, temperature and pressure of the flowing gas is measured by the laminar-based gas flow meter described above. The flow rate of the gas is adjusted manually via a needle valve (not shown in this figure).

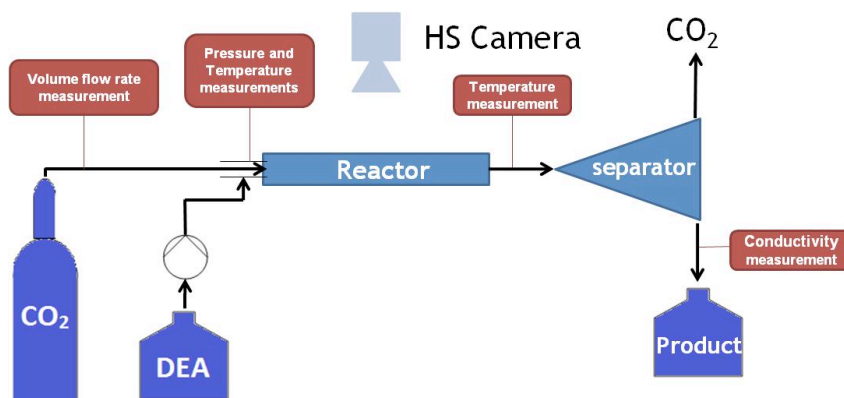


Figure 1. Experimental setup.

Experimental setup for measurement of the electrical conductivity variation with the concentration of absorbed CO₂

The electrical conductivity (resistivity) measurement was used to quantify the amount of CO₂ absorbed by DEA solution. This method consists of two stages. In the first stage, the electrical conductivity (or resistivity) of the amine solution after the microchannel is measured. In the second stage the measured conductivity is used to evaluate the amount or percentage of absorbed CO₂. The first stage can be conveniently achieved in the experimental setup as previously described. However, for the second stage, we need to know the relationship between the conductivity and the amount of CO₂ absorbed. With the current experimental setup only a two-point relationship could be obtained. For the first point the conductivity of fresh DEA solution, when no CO₂ gas is injected into the microchannel, is measured to obtain the conductivity of the solution with zero percent absorbed CO₂. For the second point, first the DEA solution is saturated by the CO₂ bubbling method, and then the saturated solution is derived through the microchannel and conductivity meter to obtain the conductivity of the 100% saturated solution.

Using the above method, the conductivity of two cases, one with zero percent and the other with 100 percent absorbed CO₂, is determined. In our previous calculations, since there was no information about the trend of conductivity versus absorbed CO₂, a linear relationship was

assumed between these two extreme conditions. However, it was understood that a more accurate approach is needed. To overcome this problem, a new experimental setup for measurement of the electrical conductivity variation with the concentration of absorbed CO₂ was designed and fabricated. A schematic of this experimental setup is depicted in Figure 2. The Pyrex flask forms the reactor where the absorption of CO₂ in DEA aqueous solution takes place. The weight of the solution must be accurately measured before the experiment. A three-way valve is used to connect the gas storage bottle either to the CO₂ tank for charging purpose or to the reactor for the absorption process experiment. A gas pressure regulator is used to maintain constant system pressure of the reactor. However, unlike the pressure of reactor, the pressure of gas storage bottle varies gradually as CO₂ gas is absorbed by the DEA solution. A pressure transducer is used to monitor this pressure. A magnetic stirrer is used to promote the absorption process in the reactor. A tubing pump is used to circulate the liquid through the conductivity measurement cell and facilitate mixing of the CO₂ gas and the DEA solution. A cooling/heating circulating bath is used to maintain the temperature of the solution constant during the experiment. Another pressure transducer measures the pressure of the gas after passing through the gas regulator. As the experiment proceeds, CO₂ gas flows from the storage bottle towards the reactor and is absorbed by the DEA solution. The conductivity cell measures the conductivity of the DEA solution as the concentration of absorbed CO₂ varies.

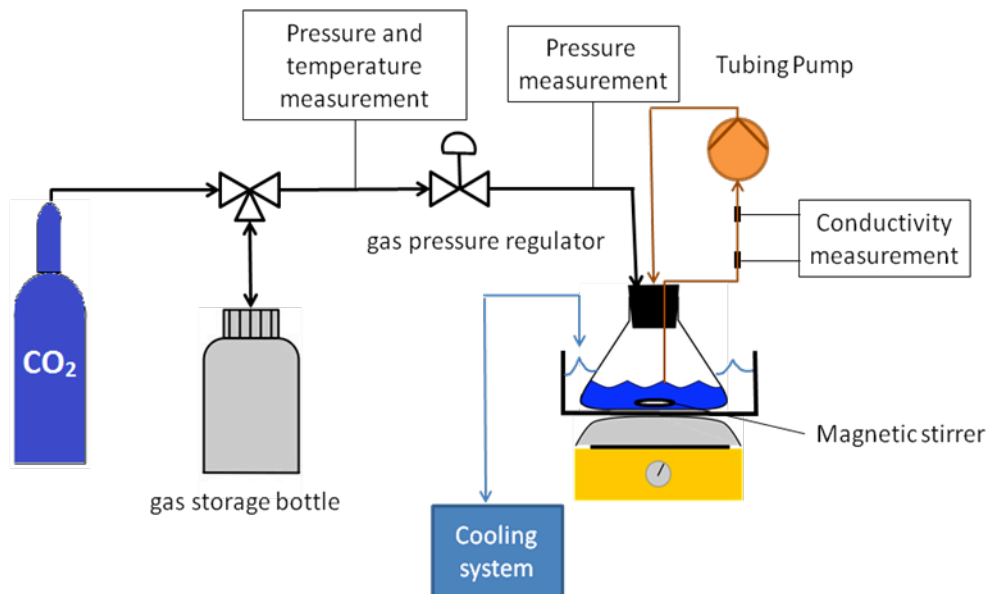


Figure 2. Experimental setup for measurement of electrical conductivity as function of absorbed CO₂ concentration.

In order to measure the amount of gas that leaves the storage bottle and gets absorbed in DEA solution, the ideal gas equation can be used:

$$\Delta m = \frac{\Delta PV}{RT} \quad (1)$$

In this equation ΔP is the pressure variation of the gas storage bottle measured by the pressure transducer, V is the total volume of the bottle and connecting tubes before the pressure regulator, T is the temperature of the bottle measured by a temperature sensor, and R is the gas constant for CO₂.

It is worth mentioning that this experiment is quite susceptible to the presence of any leakage in the setup. Therefore, special attention was given to locate the leaking spots and eliminate them.

Experimental Results

Finding an equation for calculating the ratio of absorbed CO₂/DEA

Objectives

- Investigate the relationship between ratio and conductivity
- Find equations with which to calculate the ratio in terms of conductivity
- Investigate the relationship between pressure and loading

Methodology

The maximum-absorption setup described above was used for these experiments. The storage side was filled with CO₂ and a pressure of 35 psig was maintained for each experiment. The reactor side was operated at 5, 10 and 15 psig, controlled by the pressure reducer. The reactor, including the DEA solution, was evacuated before each experiment to ensure that the air inside of the reactor would not disturb the reaction. We opened the valve between the storage side and the reactor side after evacuation. All parts of this setup except the reactor were flushed with CO₂ to ensure that the CO₂ concentration would not be diluted by air. The entire reaction took between 1 and 2 hours. The computer recorded the pressure on the storage side every 4 seconds, hence enabling us to calculate the amount of CO₂ at the end of the reaction.

Results

First, we had to apply the time-dependent pressure loss to the ratio CO₂/DEA. We used the following equation for these calculations:

p_{Start} = stored-gas pressure at beginning of experiment

$p(t)$ = stored-gas pressure

V_1 = stored-gas volume

V_2 = employed volume of DEA solution

c_{DEA} = DEA concentration of employed DEA solution

T = temperature of stored gas

$$\frac{n_{CO_2}}{n_{DEA}}(t) = \frac{(p_{start} - p(t)) * V_1}{R * T * c_{DEA} * V_2} \quad (2)$$

We also needed to transfer the collected conductivity data from the maximum-absorption setup onto the single-line setup to ensure that our equations could be applied without further calculation with the direct results from the single-line setup. For this, we first had to calculate the specific conductivity for each result obtained with the following equation:

σ = specific conductivity [S/mm]

Σ = conductivity [S]

C = cell constant, maximum-absorption setup [1/mm]

$$\sigma = \Sigma * C \quad (3)$$

The method for calculating the cell constant is explained a previous section. After transforming the equation to accommodate the specific cell constant, we then applied the equation to transfer the results onto the single-line setup:

σ_1 = specific conductivity in single-line setup

σ_2 = specific conductivity in maximum-absorption setup

$$\sigma_1 = 2.234 * \sigma_2 - 3.549 * 10^{-5} \quad (4)$$

The final transformation is the calculation from specific conductivity back to conductivity as in the single-line setup:

σ = specific conductivity [S/mm]

Σ = conductivity [S]

C = cell constant, single-line setup [1/mm]

$$\Sigma = \frac{\sigma}{C} \quad (5)$$

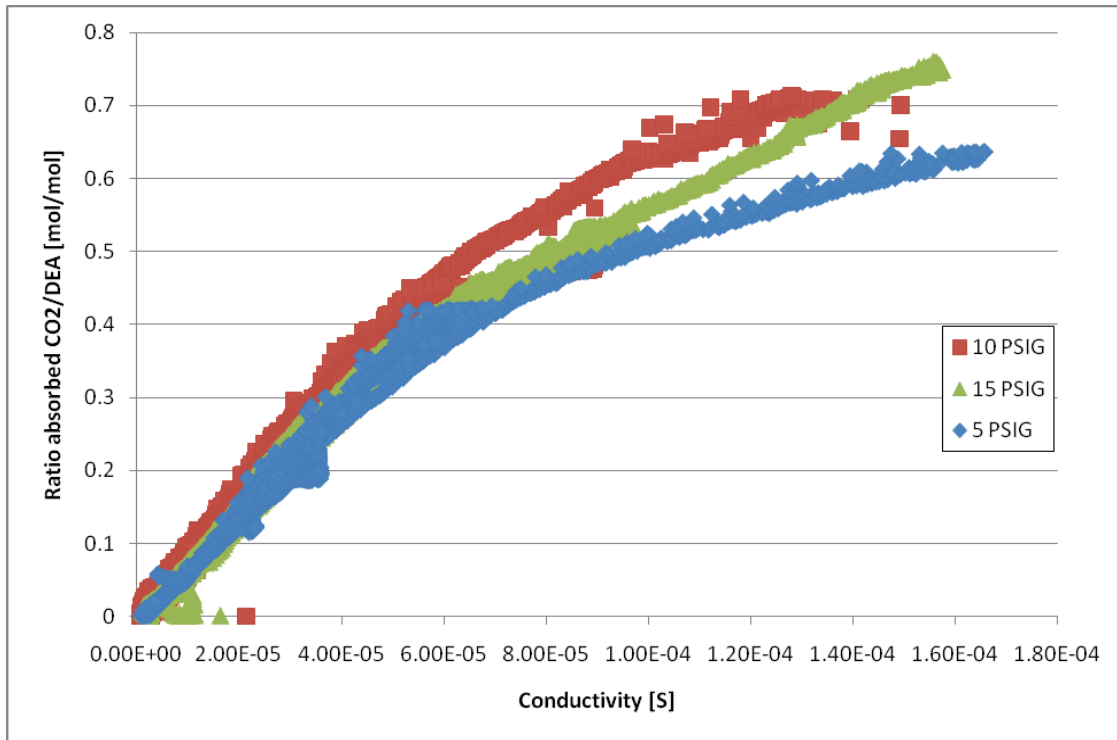


Figure 3. Ratio of absorbed CO₂/DEA vs. conductivity at 10 psig, 15 psig and 5 psig.

Figure 3 shows the results of our test runs, at least 4 each, for all 3 pressures. The tests run with 10 and 15 psig are important for our work with the single-line setup. Consequently, we omitted the 5-psig results in the following work steps. With the 2 remaining curves situated so close to each other, only their end points indicate an increase in pressure. These curves enabled us to construct an equation for all 3 pressures. With the combined results of the 10-psig and 15-psig runs and the Excel equation function, we arrived at the following function:

σ = Conductivity [S]

R = Ratio absobt CO₂/DEA [mol/mol]

$$R = 1.829 * 10^{11} * \sigma^3 - 6.252 * 10^7 * \sigma^2 + 1.032 * 10^4 * \sigma - 2.020 * 10^{-2} \quad (6)$$

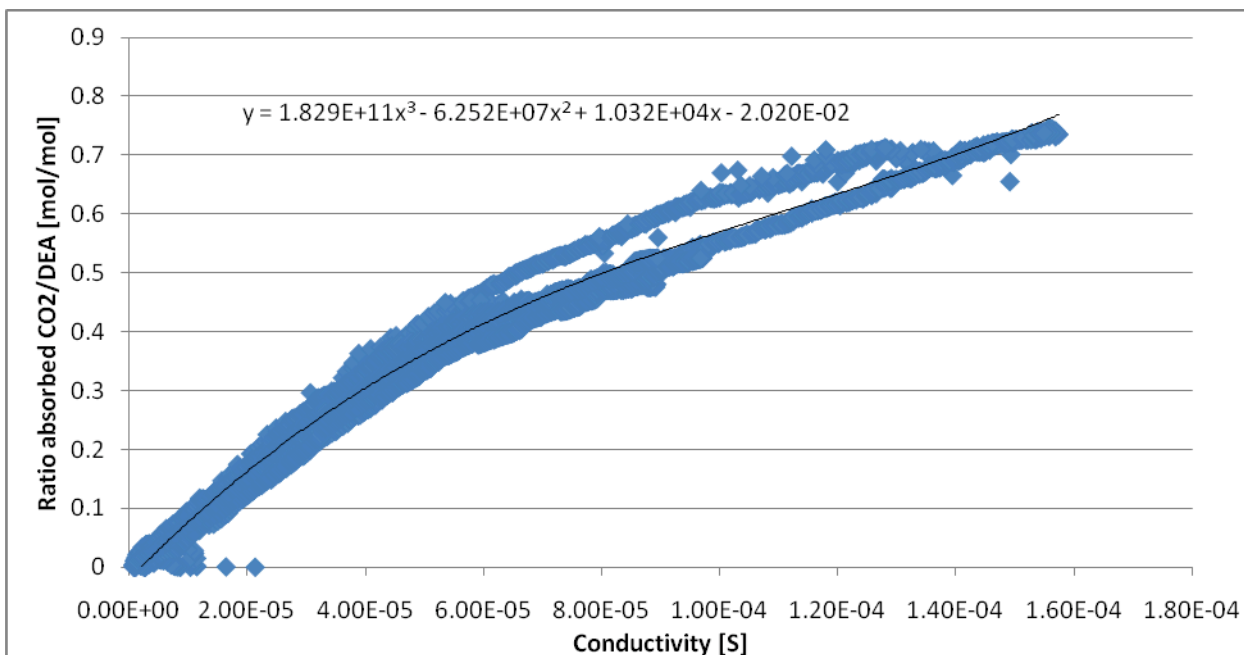


Figure 4. Ratio of absorbed CO₂/DEA vs. conductivity for 10 and 15 psig.

Discussion

The good repeatability of the runs made us feel confident that this equation fairly closely represents the real conditions. Even the end-point rise with increasing pressure matched our expectations. Some work still remains to be done, since our experiments did not yield an absolute end point for every pressure condition. While the end points were situated close to each other, they nonetheless showed residual divergence. Consistent end points would be desirable, but the different end points are not inconsistent with our equation, because the form of the relation between ratio and conductivity is always the same. We therefore remain confident in our use of the equation:

x = conductivity

y = ratio absorbed CO₂/DEA

$$y = 1.829E+11x^3 - 6.252E+07x^2 + 1.032E+04x - 2.020E-02 \quad (7)$$

We also refrained from constructing a loading equation like in that past, because it is absolutely necessary for the present purposes to know the conductivity of maximum loaded DEA.

Change of reactor size

Objectives

- Develop the relationship between length and efficiency
- Improve the efficiency of the reactor
- Develop the relationship between reactor length and system pressure

Methodology

For this experiment, we used the microchannel setup described in Figure 2, but with several modifications. First, we reduced the length of the tube behind the reactor to the point of negligibility. That is comparable to reducing the length of the main reactor, because we used the

same kind of tube for the connection between the reactor and the separator. After several initial test runs with this setup, we began to increase the length of the reactor. The following table recounts the experimental changes in reactor length.

Table 1. Experimental changes in reactor length

Length of reactor [cm]	Length of reactor-separator connecting tube [cm]	Total length [cm]
20	2	22
20	30	50
80	2	82

The 50 cm-long version represents the setup that had already been used and which was employed for the previous experiments. To ensure that the temperature in our experiments was not subject to change due to air streams in the laboratory, we incorporated a heat-exchange system. As seen in Figure 5 and Figure 6, we installed two copper tubes carrying water well tempered by a cooling system. We held the temperature of the cooling system at 25 °C. That corresponds to the temperature most used in the past. To decrease the influence of air streams in the lab while increasing the influence of the cooling system, we also installed an insulating system. The cooling bath at the end of the reactor helped us maintain the temperature of the DEA solution at a constant 25 °C.

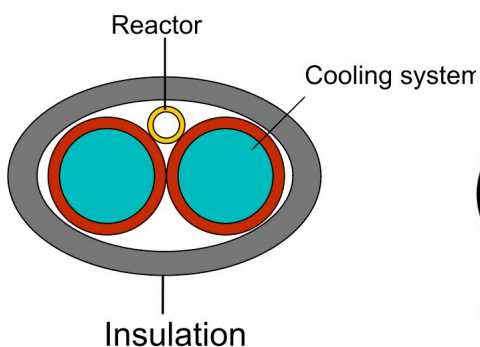


Figure 5. Copper tubing heat exchanger.

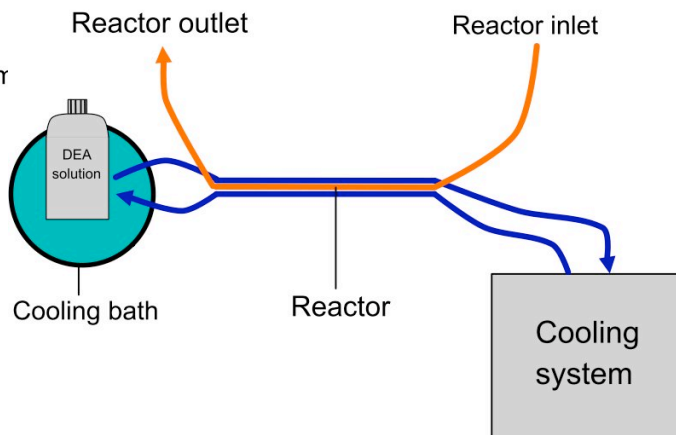


Figure 6. Cooling system schematic.

We test-ran all three reactor lengths with the volume ratios 1.5, 2.5, 3.75, 5, 7.5 and 10 at least as long as necessary to obtain three reproducible runs for every length and every volume ratio. We defined “reproducible” as having a maximum deviation of 5% from average.

Results

We inserted the conductivity data collected with different reactor lengths into this equation:

$$R = 1.829 \cdot 10^{11} \cdot \sigma^3 - 6.252 \cdot 10^7 \cdot \sigma^2 + 1.032 \cdot 10^4 \cdot \sigma - 2.020 \cdot 10^{-2} \quad (8)$$

σ = conductivity [S]

R = ratio absorbed CO₂/DEA [mol/mol]

Figure 7 below represents the results obtained for the 3 different reactor lengths and the different volume ratios. Each point was confirmed for reproducibility by at least 3 reproducible runs.

We also monitored the pressure at the inlet of the reactor. To develop a feeling for the pressure conditions within the reactor, we calculated its average interior pressure using the following equation:

p_{in} = inlet pressure

p_{out} = outlet pressure (equal to ambient air pressure = 0 psig)

$p_{average}$ = average pressure in the reactor

$$p_{average} = \frac{p_{in} + p_{out}}{2} \quad (9)$$

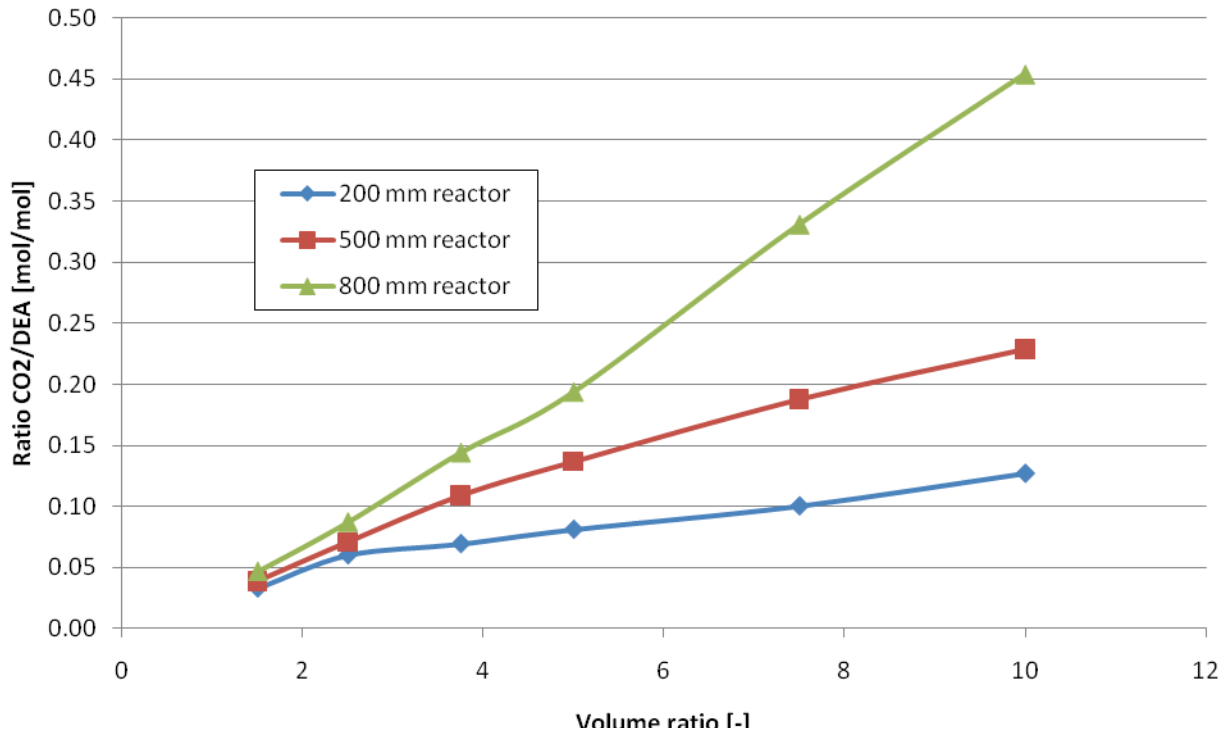


Figure 7. Volume ratios of absorbed CO₂/DEA for three reactor lengths. The ratio of absorbed CO₂/DEA increases with the length of the reactor.

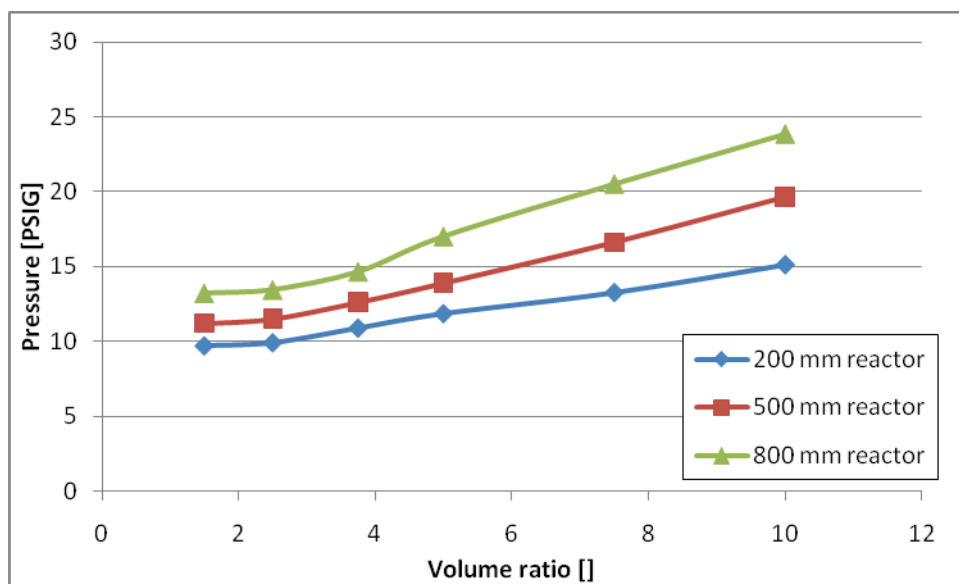


Figure 8. Average interior pressure of reactor.

Discussion

The results shown in Figure 7 closely match our expectations. The ratio of absorbed CO_2/DEA increases with the length of the reactor. That makes sense, because the reaction time increases with the size of the reactor. With more time to react, the DEA has more time to absorb the CO_2 . Calling to mind that it takes 2 mol DEA to absorb 1 mol CO_2 , we realize that full absorption is achieved at a ratio of 0.5. Hence, for 0.45 the result was very close to full absorption (every DEA mol having been used). Of course, there will always be a degree of uncertainty as long as we employ an equation based on experimental results. For a higher volume ratio, we anticipate a gentler slope in these graphs. With every increase in volume ratio, we also increased the flow of CO_2 through the reactor. A higher flow of CO_2 affected the flow of the DEA solution, and with that the concentration movements in the DEA solution. The spent DEA moves away from the interface between gas and liquid and is replaced with fresh DEA that is better able to enter into reaction. We expect that, at some point, further increasing the flow of CO_2 would no longer help mix the DEA solution, and that the reaction time in a short reactor will set the limit for the highest possible ratio.

Figure 8 also matches our expectations. It is only logical for the pressure to rise for any volume ratio in response to lengthening of the reactor. With every additional cm of reactor length, friction between the fluids and the reactor wall increases the resistance that the fluid has to overcome. As long as the volume flow remains constant during the test runs, the pressure has to increase to compensate for the friction.

Transfer of conductivity from one setup to the other

Objectives

A function was needed to enable transfer of the results of the maximum-absorption setup to the single-line without loss of accuracy.

Methodology

We measured the conductivity of 5 different DEA solutions. Each DEA solution had a different ratio of absorbed CO_2/DEA . We measured the conductivity in both setups and compared them

with each other. The first step of comparison was to calculate a cell constant from the geometry of the measurements. With this constant we were able to calculate the specific conductivity. We plotted this specific conductivity and let Excel calculate a function that enabled us to transfer the specific conductivity from one setup to the other.

Results

First, the conductivity data from the different setups had to be converted to specific conductivity to make them more amenable to comparison. We calculated the cell constant from the geometry using the following equation:

d = inner tube diameter [mm]
 l = length of tube between the two electric contacts [mm]
 C = cell constant [mm]

$$C = \frac{4 * l}{d^2 * \pi} \quad (10)$$

With this equation, we then calculated the following constants for both setups:

Table 2. Constants for experimental setups

Maximum-absorption setup constant	112.2 1/mm
Single-line setup constant	82.875 1/mm

The next step was to use the constants to calculate the respective specific conductivity with the following equation:

σ = specific conductivity [S/mm]
 Σ = conductivity [S]
 C = cell constant [1/mm]

$$\sigma = \Sigma * C \quad (11)$$

The following diagram shows the results of all five runs. The red dots were included to demonstrate the fact that this is a linear function.

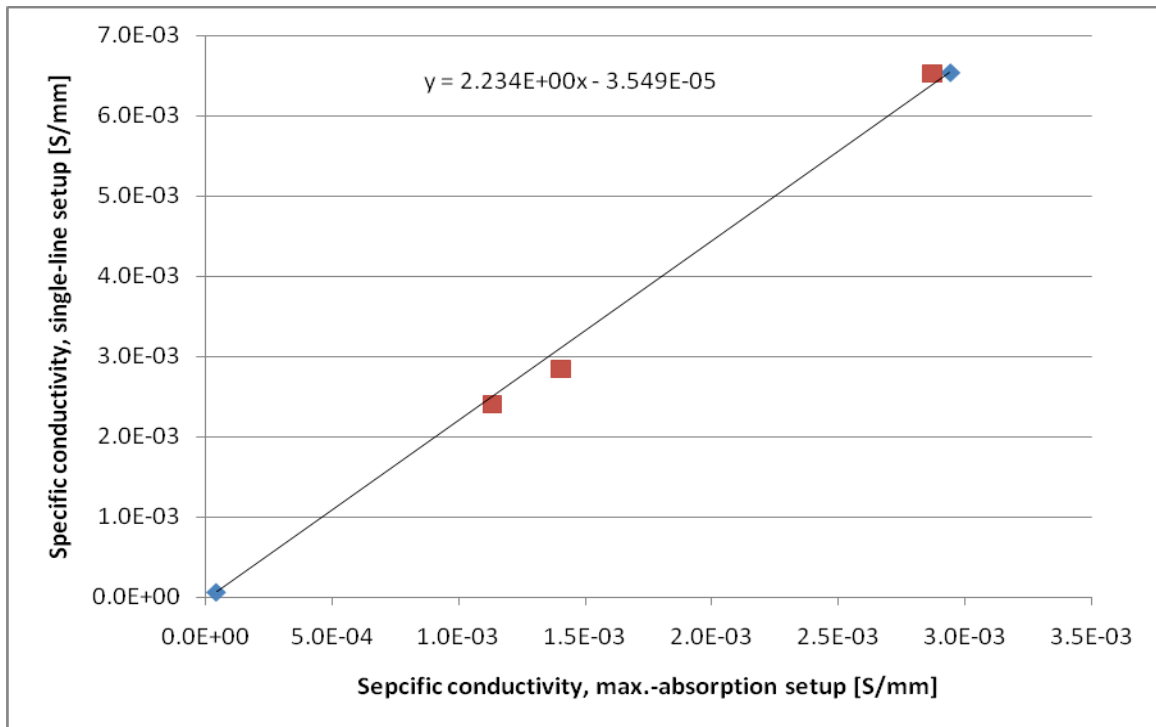


Figure 9. Specific conductivity.

Discussion

It is important to note that the equation derived from Figure 9 is only useful for transferring results from the maximum-absorption setup to the single-line setup. If it should become necessary to transfer the results the opposite way, a new equation would have to be created. The red squares were included in order to demonstrate the linearity of the system. The results are situated quite close to our line, and we are therefore confident that our adjusted assumption is correct.

Validating the results of Kuzmicki

Using the experimental setup shown in Figure 1, a series of experiments was conducted to replicate the results of Kuzmicki. A few runs with the single-channel setup were made, and as can be seen in Figures 10 to 15, the results do not differ too much in their value. All necessary values of every volume-flow ratio are shown in Table 3. Also the standard deviations of both researchers are included. The calculations of the standard deviations were made with Excel and all measurements were used.

Table 3. Average conductivities, means and standard deviations of all volume-flow ratios of both researchers

Volume-flow ratio		Experimental runs average conductivity [S]			Average [S]	Standard deviation
		1 st	2 nd	3 rd		
1.5	Herzog	6.34E-06	6.04E-06	5.84E-06	6.06E-06	2.51661E-07
	Kuzmicki	6.23E-06	6.09E-06	5.84E-06	6.08E-06	3.12631E-07
2.5	Herzog	1.05E-05	1.06E-05	1.07E-05	1.06E-05	1.01E-06
	Kuzmicki	9.56E-06	9.66E-06	9.30E-06	9.51E-06	4.14777E-07
3.75	Herzog	1.50E-05	1.52E-05	1.48E-05	1.50E-05	1.62453E-06
	Kuzmicki	1.37E-05	1.38E-05	1.38E-05	1.38E-05	4.25983E-07
5.0	Herzog	1.74E-05	1.69E-05	1.76E-05	1.69E-05	5.31977E-07
	Kuzmicki	1.72E-05	1.73E-05	1.72E-05	1.72E-05	4.87462E-07
7.5	Herzog	2.60E-05	2.47E-05	2.43E-05	2.50E-05	2.58E-06
	Kuzmicki	2.37E-05	2.33E-05	2.34E-05	2.35E-05	1.32311E-06
10.0	Herzog	2.83E-05	2.90E-05	2.94E-05	2.88E-05	2.43308E-06
	Kuzmicki	2.93E-05	2.88E-05	2.90E-05	2.90E-05	2.20231E-06

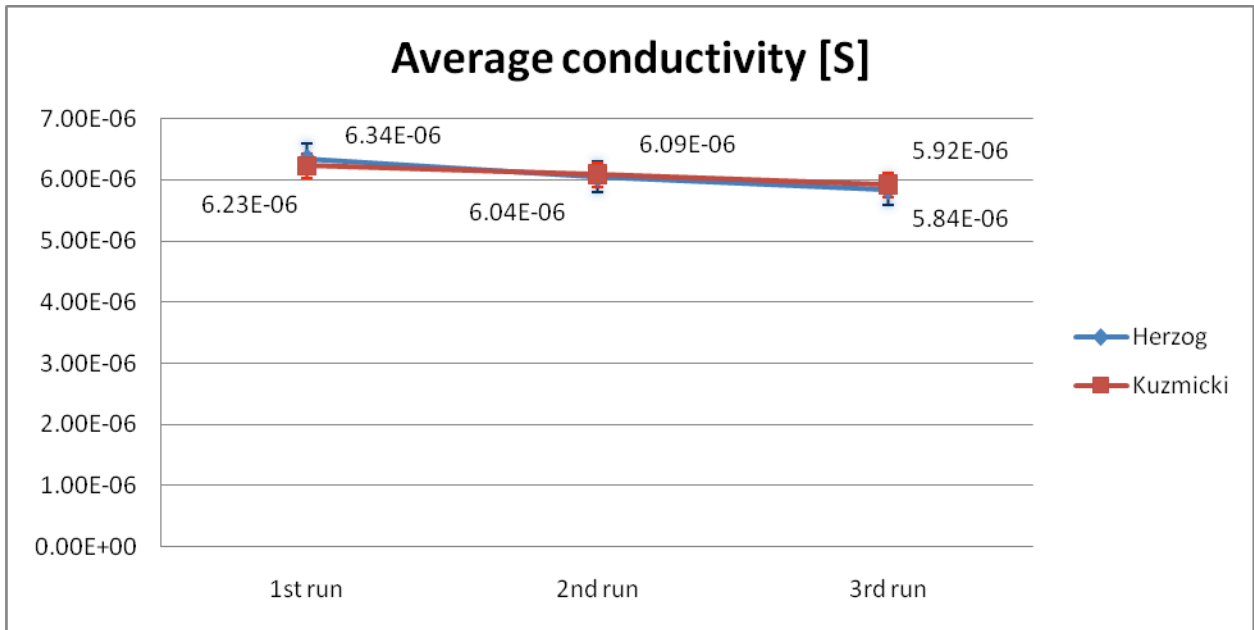


Figure 10. Comparison of the results of the 500mm microchannel reactor with a volume-flow ratio of 1.5 between Herzog and Kuzmicki.

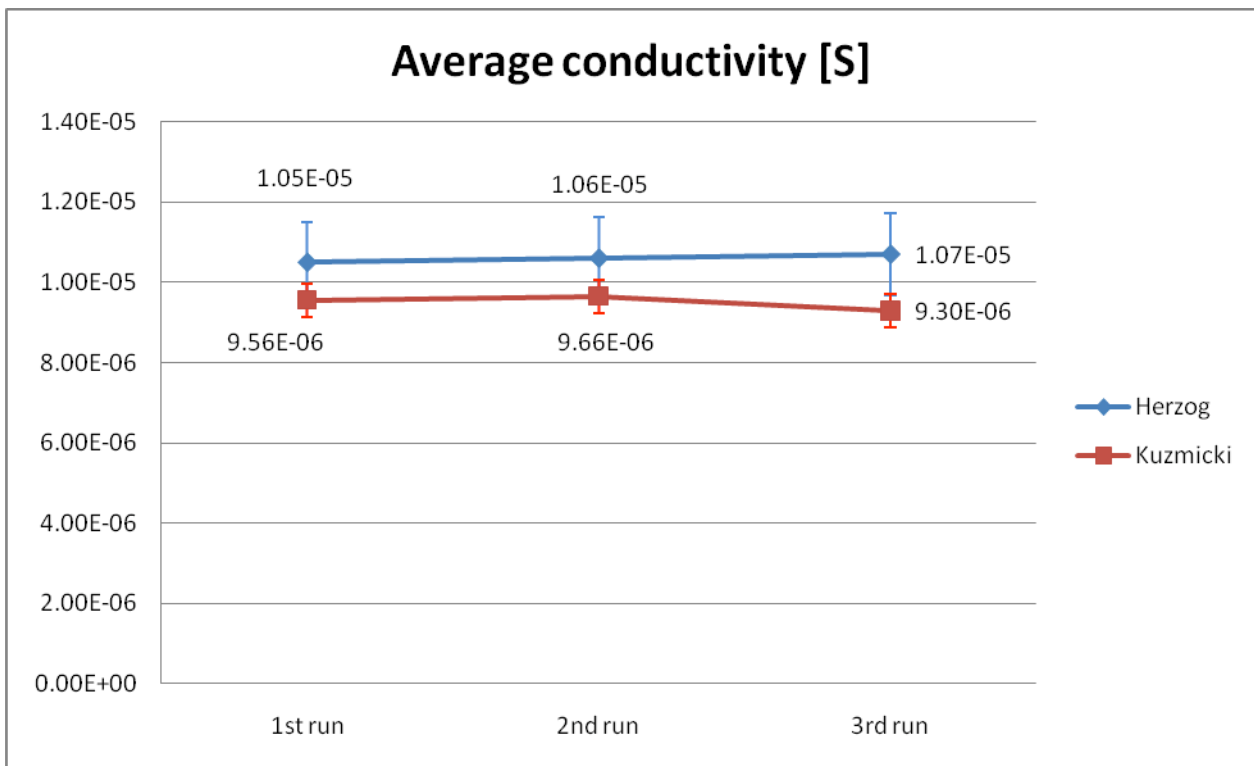


Figure 11. Comparison of the results of the 500mm microchannel reactor with a volume-flow ratio of 2.5 between Herzog and Kuzmicki.

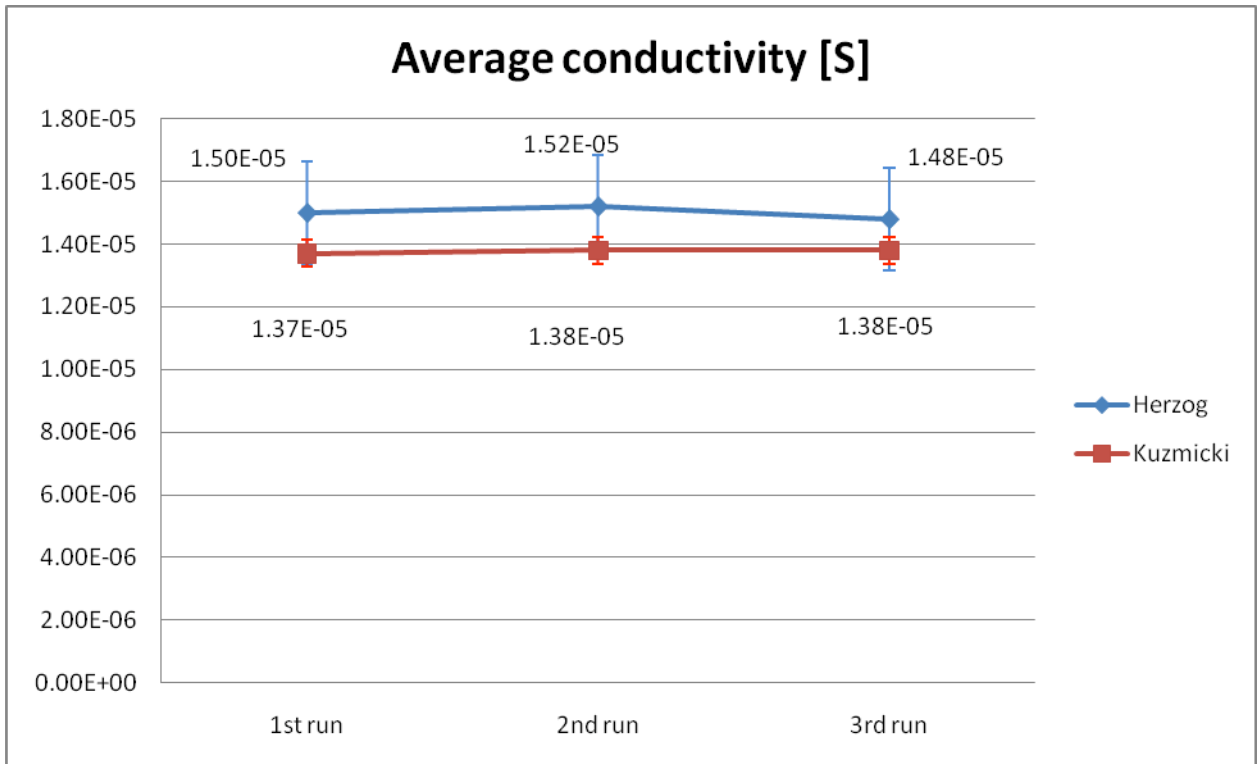


Figure 12. Comparison of the results of the 500mm microchannel reactor with a volume-flow ratio of 3.75 between Herzog and Kuzmicki.

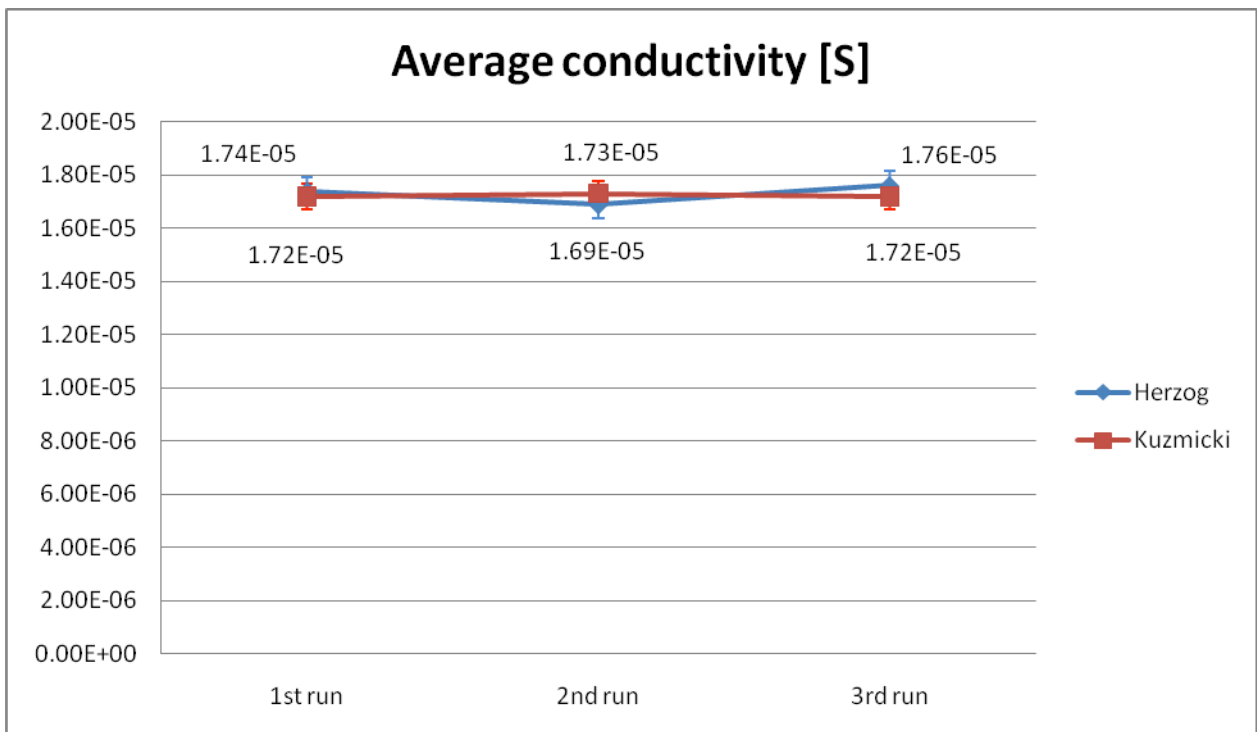


Figure 13. Comparison of the results of the 500mm microchannel reactor with a volume-flow ratio of 5.0 between Herzog and Kuzmicki.

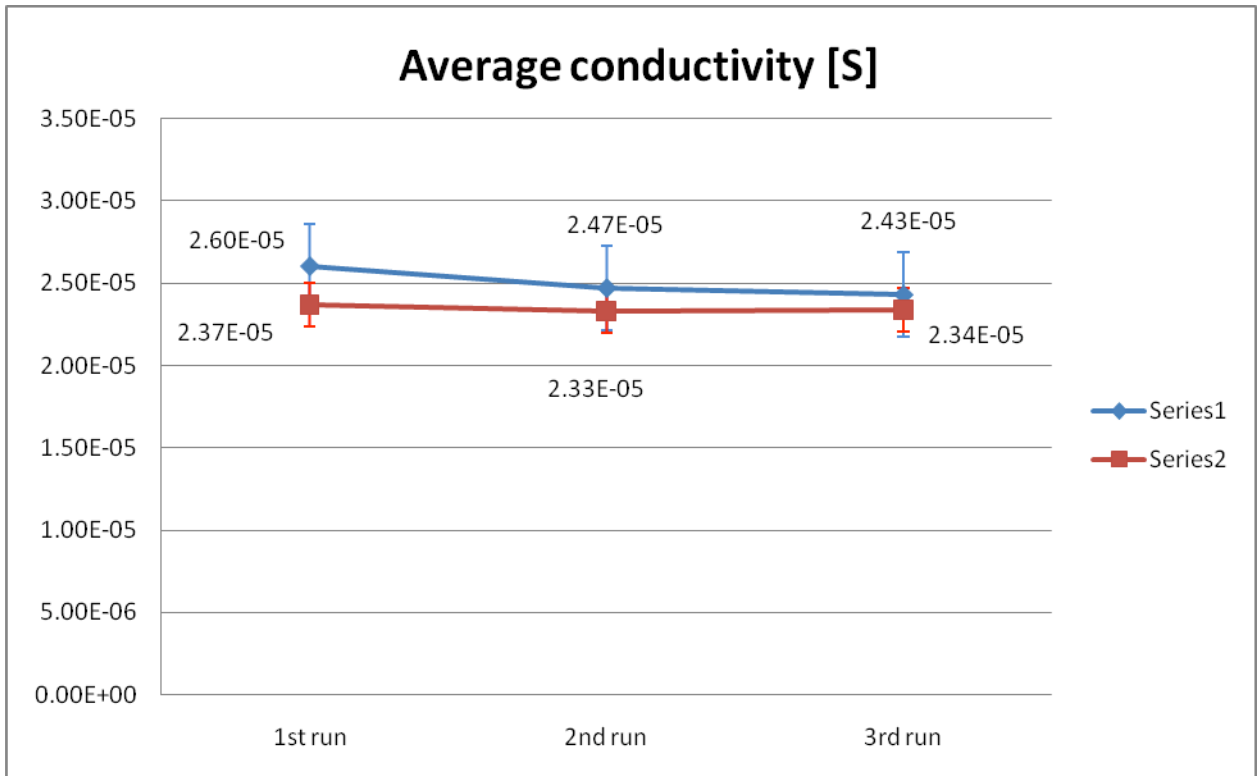


Figure 14. Comparison of the results of the 500mm microchannel reactor with a volume-flow ratio of 7.5 between Herzog and Kuzmicki.

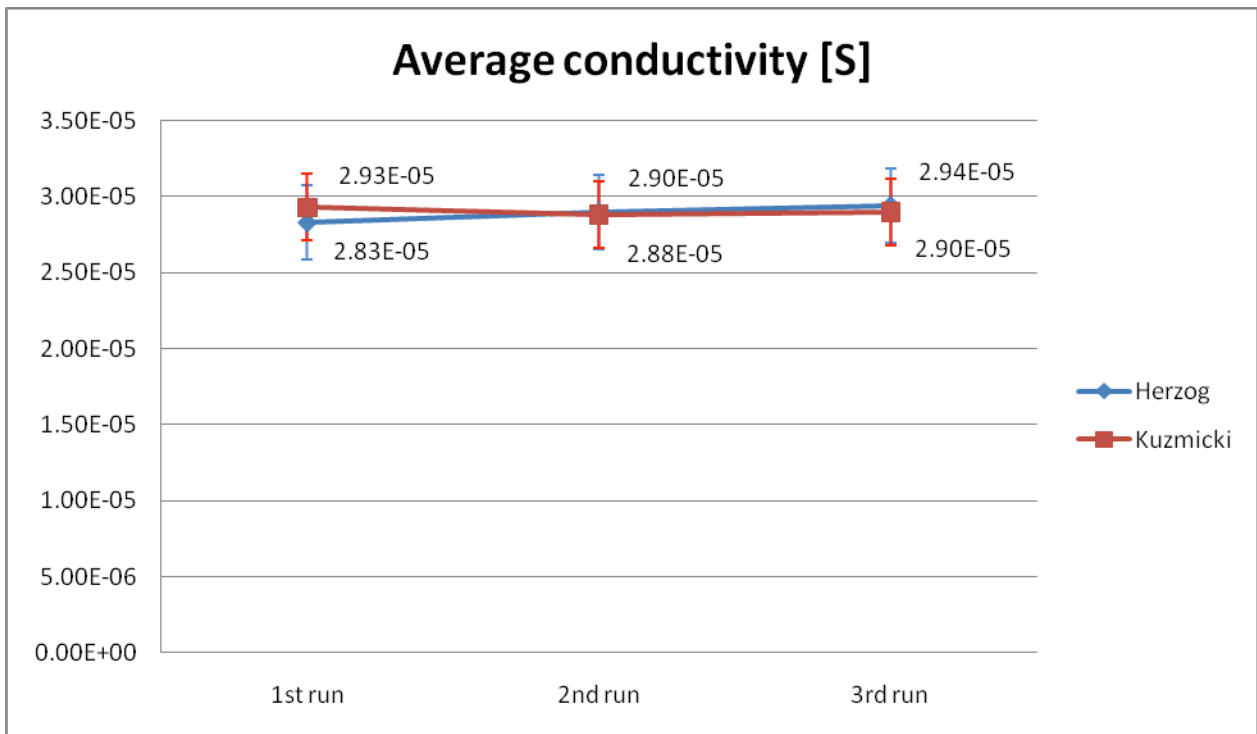


Figure 15. Comparison of the results of the 500mm microchannel reactor with a volume-flow ratio of 10.0 between Herzog and Kuzmicki.

As can be seen in Figures 10 to 15, we were able to reproduce the results of Kuzmicki, and the results are in good agreement with each other. This leads us to conclude that both researchers did not make any mistakes regarding the calculations or the apparatus construction. With this certainty we can now move on and start new experiments, e.g. with bigger reactor diameters or the maximum absorption of CO₂ in DEA.

Summary of Results

In this reporting period different experiments were made and results fulfilling our expectations were gathered. The good repeatability of the runs made us feel confident that the equation for the absorbed CO₂/DEA fairly closely represents the real conditions. Different end points are not inconsistent with our equation, because the form of the relation between ratio and conductivity is always the same. We therefore remain confident in our use of Equation 6.

The results shown in Figure 7 closely match our expectations. The ratio of absorbed CO₂/DEA increases with the length of the reactor and it is only logical for the pressure to rise for any volume ratio in response to lengthening of the reactor.

According to Figure 9, a linear function between the absorbed CO₂/DEA and different DEA-solutions were found, but this function is only useful for transferring results from the maximum-absorption setup to the single-line setup and not vice versa.

A set of data from the single-channel reactor was collected. The results showed a good agreement regarding the average conductivity. Also, in this period, a comparison in respect of the surface-volume ratio between the microchannel reactor and a column with a packing of Rashig rings, which are used in coal-fired power plants, was made.

5. Difficulties Encountered/Overcome

None to report.

6. Planned Project Activities for the Next Quarter

- Continue on literature survey
- Conduct further experiments and collect data
- Conduct a parametric study
- Design/Fabrication of a 2nd generation laboratory scale Microchannel CO₂ separator
- Continue on collaboration work with the PI partners to compare experimental results with numerical modeling results for the absorption process

Appendix

Justification and Background

The development of environmentally friendly process in industry is one of the major goals that have to be achieved. One way to approach cleaner environment is capturing or minimizing harmful gas components before emission to the atmosphere. One of the main gases which contribute significantly in global warming is CO₂. Due to a necessity to develop more efficient techniques for CO₂ capturing, scientific research in this area has been expanded rapidly. Since in the past very little R&D was devoted to CO₂ capture and separation technologies, opportunities for revolutionary improvements in CO₂ separation technologies is very high. To maintain its competitiveness and bring environmental friendly industry to the region, ADNOC has adopted various policies and approached it via many plans including “zero-flare” policy, acquiring more energy efficient process and the agreement signed with MASDAR to develop CO₂ capture technology. CO₂ separated from flue gases will be re-injected in oil wells, increasing oil production.

One of the promising concepts which can lead to major technology advancement is microchannel-based absorption units with enhanced kinetics. The objective of this study is to develop a full process of CO₂ separation from flue gas with incorporating micro-channel absorption technology at laboratory scale. The project addresses various stages of separation process: separation of solid particles and condensed water droplets and CO₂ separation using absorption process. Microchannel absorption CO₂ separator developed in this project will, significantly, increase the efficiency of separation process while decreasing energy consumption involved in such operation. Moreover, development of such technology will lead to reduction of equipment's size and, therefore, minimizing the footprint and cost of equipment. An electrostatic separator will be used prior to CO₂ separation to remove solid and liquid contaminants from flue gas. The ultimate objective is to design all separation stages such that the overall performance will be optimized.

Approach

Detailed analysis and identification of the phenomena and the design challenges involved in effective implementation of the mechanism. Parametric study of existing and improved separators. Design iterations, including numerical flow and field simulations, fabrication, and testing. Creation of database and engineering design correlations.

Three-Year Schedule

The schedule below reflects the revised scope approved by both sides

Year 1:

- Conduct literature review to understand the basic of mass transfer in micreactor and separation of flue gas;
- Evaluate existing technologies and assess their applicability to CO₂ separation of flue gas;
- Repeat and implement some previous classical examples of microchannel separation to get familiarized with fundamentals and basic challenge;
- Analyze mixing in microchannels and possibility to use it in CO₂ separation;
- Continue improving efficiency of EHD separator for the fine liquid and solid particles;
- Conduct visualization study of liquid and solid particles migration in the electrical field.

Year 2:

- Continue on literature survey;
- Selection of the target alkanolamine;
- Simulate mixing and separation phenomena in microreactor via modeling and analytical means;
- Develop laboratory scale microchannel absorber and desorber for CO₂ separation;
- Conduct Experimental study and design optimization study;
- Continue on visualization study of liquid and solid particles migration in the electrical field.
-

Year 3:

- Conduct visualization study on absorption and desorption in microchannels;
- Design iterations and implementation;
- Parametric study of CO₂ separation process and experiment on different designs;
- Continue on simulation of mixing and separation phenomena in microreactor via modeling and analytical means;
- Present the best design to ADNOC group of companies;
- Develop design correlation;
- Prepare report.

References

- [1] Aresta, Michael, ed. *Carbon Dioxide Recovery and Utilization*. Kluwer Academic Publishers, 2003.
- [2] Kohl, Arthur L., and Richard B. Nielsen. *Gas purification*. Houston, Texas: Gulf Publishing Company, 1985.
- [3] Rinker, Edward B., Sami S. Ashour, and Orville C. Sandall. "Kinetics and Modeling of Carbon Dioxide Absorption into Aqueous Solutions of Diethanolamine." *Ind. Eng. Chem. Res.* 35 , no. 4 (1996): 1107–1114.

Microreactors for Oil and Gas Processes Using Microchannel Technologies

UMD Investigators: Serguei Dessiatoun, Amir Shooshtari, Kyu Young Choi

GRA: Meera Mahadevan

PI Investigators: Afshin Goharzadeh, Ebrahim Al-Hajri (Returning ADNOC Scholar)

Start Date: Oct 2006

1. Objective/Abstract

Microfabrication techniques are increasingly used in gas and petrochemical engineering to realize structures with capabilities exceeding those of conventional macroscopic systems. In addition to already demonstrated chemical analysis applications, microfabricated chemical systems are expected to have a number of advantages for chemical synthesis, chemical kinetics studies, and process development. Chemical processing advantages from increased heat and mass transfer in small dimensions are demonstrated with model gas, liquid and multiphase reaction systems.

Evaluation of different applications for microreactors and their impact on UAE industry economies has been conducted in this quarter. The application of microreactors in the polymerization of ethylene and propylene is feasible and may provide significant economical benefits, therefore will be considered for further investigation in the current project

2. Milestones/Deliverables Scheduled for the Completed Quarter

- Design of tubular polymerization microreactor
- Detailed theoretical modeling of polymerization in microreactor.

3. Summary of Project Activities for the Completed Quarter

Modeling the reaction kinetics for a microreactor channel

Brief introduction to the theory behind the modeling

Reaction Kinetics- Coordination mechanism

- | | |
|-------------------------------|--|
| 1) Catalyst site activation | $C_o + MAO \xrightarrow{k_a} C^*$ |
| 2) Initiation | $C^* + M \xrightarrow{k_i} P_1$ |
| 3) Propagation | $P_n + M \xrightarrow{k_p} P_{n+1}$ |
| 4) Chain transfer to monomer | $P_n + M \xrightarrow{k_{fm}} P_1 + M_n$ |
| 5) Chain transfer to hydrogen | $P_n + H_2 \xrightarrow{k_{fh}} M_n + C^*$ |
| 6) Deactivation | $P_n \xrightarrow{k_d} M_n + D^*$ |
| | $C^* \xrightarrow{k_d} D^*$ |

Here,

C^* – Activated Catalyst

D^* – Deactivated Catalyst

M – Monomer

P – Polymer

k – Rate constants

M_n – Dead polymer

n – Chain length

P_n – Live Polymer

I – Initiator

R – Radical

We now represent the reaction rates with respect to each of the reactants and products by the following expressions:

Coordination
$r_M = -k_i C^* M - k_p PM - k_{fm} PM$
$r_{C^*} = -k_i C^* M - k_{fh} H_2^p \sum_{n=2}^{\infty} P_n - k_d C^*$
$r_{P_1} = k_i C^* M - k_p P_1 M + k_{fm} \sum_{n=2}^{\infty} P_n M$
$r_{P_n} = k_p (P_{n-1} - P_n) M - k_{fm} M P_n - k_{fh} H_2^p P_n - k_d P_n$
$r_{H_2} = -k_{fh} H_2^p \sum_{n=2}^{\infty} P_n$
$r_{M_n} = -k_{fm} M P_n + k_{fh} H_2^p P_n + k_d P_n$

Molecular weight moments

Polymers produced from a reaction are distributed over a wide length range and usually a Gaussian distribution of molecular weights is assumed. Normalizing this weight distribution is an aspect that can be worked on. Weight moments are defined to get a polymer weight distribution based on the chain length.

- Live polymer moment

$$\lambda_k' = \sum_{n=1}^{\infty} n^k P_n$$

- Dead polymer moment

$$\lambda_k = \sum_{n=2}^{\infty} n^k M_n$$

- The number average and weight average polymer molecular weights are defined as

$$\bar{M}_n = M_0 \frac{\lambda_1' + \lambda_1}{\lambda_0' + \lambda_0} \quad \text{and} \quad \bar{M}_w = M_0 \frac{\lambda_2' + \lambda_2}{\lambda_1' + \lambda_1}$$

The instantaneous chain length distribution for olefin polymerization is given by a single-parameter equation, Flory's most probable distribution (Flory, 1953), where $w(r)$ is the weight chain length distribution for polymer chains of length r , and τ is the ratio of all chain transfer rates to the propagation rate.

$$w(r) = r\tau^2 \exp(-r\tau),$$

The chain length distribution function is often combined with a reactor residence time distribution function to calculate the overall molecular weight distribution in a continuous process.

Microreactor

The microchannel can be considered as a plug flow reactor with a few microns of diameter. We consider an unsteady state flow and ignore axial and radial dispersions and assume isothermal behavior initially for simplicity.

A mass balance for a PFR results in the following equation where C_i is the concentration of a component 'i' varying along the length of the reactor 'y'. 'v' is the velocity of flow, 'A_r' is the cross-sectional area of the reactor, and 'r_i' is the reaction rate with respect to component i.

$$\frac{\partial C_i}{\partial t} = -\frac{v}{A_r} \frac{\partial C_i}{\partial y} + r_i$$

Using all the above equations we obtain a mass balance for the coordination mechanism in terms of moments:

$$\begin{aligned}\frac{\partial \lambda'_o}{\partial t} &= -u \frac{\partial \lambda'_o}{\partial y} + k_p M \beta \lambda'_o - (k_{fh} H_2^p + k_d)(1 - \alpha^{1-n}) \lambda'_o \\ \frac{\partial \lambda_o}{\partial t} &= -u \frac{\partial \lambda_o}{\partial y} + (k_{fh} H_2^p + k_d + k_{fm} M)(1 - \alpha^{1-n}) \lambda'_o \\ \frac{\partial M}{\partial t} &= -u \frac{\partial M}{\partial y} + (k_i \beta + k_p + k_{fm}) \lambda'_o M \\ \frac{\partial H_2}{\partial t} &= -u \frac{\partial H_2}{\partial y} - k_{fh} (1 - \alpha^{1-n}) \lambda'_o H_2^p\end{aligned}$$

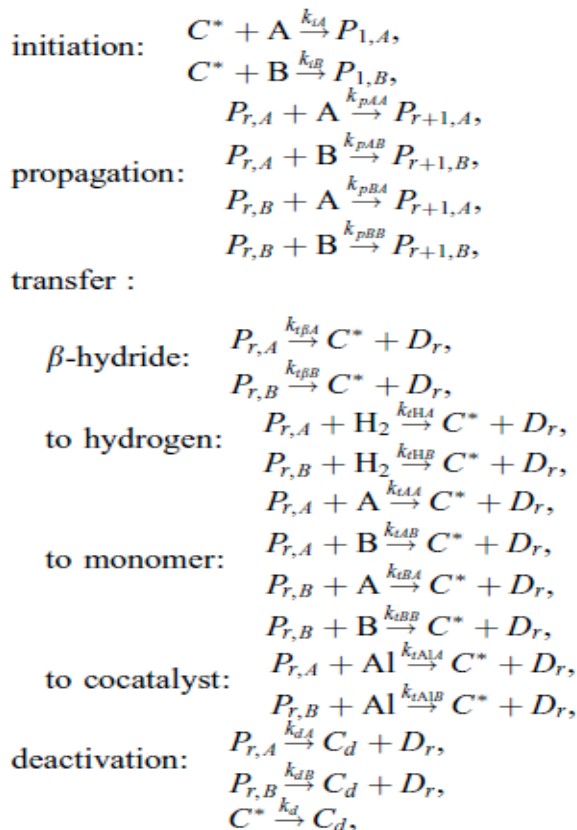
For a steady-state plug flow reactor,

$$\begin{aligned}\frac{\partial C_i}{\partial t} &= -\frac{v}{A_r} \frac{\partial C_i}{\partial y} + r_i \\ \frac{v}{A_r} &= u \quad (\text{Linear Velocity}) \\ u \frac{\partial C^*}{\partial y} &= -k_d C^* \quad (\text{Active site Catalyst}) \\ u \frac{\partial M}{\partial y} &= -k_p C^* M \quad (\text{Monomer}) \\ C^* &= C_0^* \exp\left(\frac{-k_d y}{u}\right) \\ M &= M_0 \exp\left[\frac{k_p}{k_d} (C^* - C_0^*)\right]\end{aligned}$$

We consider the active center of a supported metallocene catalyst as a surface fixed microreactor, which produces polymer independent of other microreactors. Therefore, the deactivation of such an active center is not a function of the distance between those centers, the active center concentration. Our kinetic measurements of gas phase polymerization of supported metallocenes lead us to the hypothesis that the deactivation is proportional to the polymerization rate, which can be influenced by a number of physical and chemical factors. From our present data it can be deduced that it is most likely that a certain percentage of the insertions lead to deactivated sites. An important indication for the blocked site hypothesis could be the generally noticed increase in activity in the presence of H₂ as a chain transfer agent. The small H₂ molecule could easily break the bond between blocking polymer and site by chain transfer, reactivating the site in this way.

Co-polymerization kinetics

We have been considering ethylene homopolymerization so far. We now consider copolymerization kinetics of ethylene with any other monomer like butene or hexene to produce high-density polymers.



The velocity conundrum:

The Reynolds number for turbulent flow should typically exceed 2200. For a 500 micron microchannel, a simple calculation would show us that a velocity of around 5m/sec. This velocity is extremely high for flow through a microchannel.

Findings from “Microchannel Reactors: Applications and Use in Process Development” (International Journal of Chemical Reactor Engineering) indicate that

- Most published work assumes the validity of Navier-Stokes equations despite some contradictory results.
- For microchannels (>30 μm) the flow can be described by conventional theory, and laminar to turbulent transition is governed by conventional rule of $\text{Re} \leq 2500$.
- The momentum equations are considered to be decoupled from conservation of mass and heat equations and are separately solved.
- The fluid properties and composition of gas and liquid streams are independent of the chemical reactions in the temperature range.
- The heat and mass transfer equations utilize the average velocity and it is generally believed that the laminar flow profile or the flow development does not influence heat and mass transfer.

- The gas is modeled as a continuum, and the system is considered to be thermodynamically ideal following Henry's law and Fickian diffusion mechanisms.
- It is reasonable to assume no-slip boundary condition for the momentum equation and no flux condition for the mass balance equation. Similarly, no heat-flux condition is valid for the left, right and top edges of the domain while the bottom wall of the reactor housing is assumed to be at constant temperature in equilibrium with the coolant channel.

Particle morphology

The MGM is one of the most extensively used models for the prediction of polyolefin particle morphology and is well supported with experimental evidence from electron microscope and TEM studies [8–13]. The model assumes instantaneous fragmentation of the catalyst particle into a large number of catalyst fragments that remain encapsulated by growing polymer to form microparticles. These microparticles are the building blocks of the entire polymer particle, termed the macroparticle.

The MGM models the transport of mass across the external boundary layer of the macroparticle as well as mass transport through the pores of the macroparticle (i.e., in the voids between the microparticles).

Diffusion limitations in the pores can lead to concentration gradients of species such as monomers, cocatalysts, and donors. At every radius of the macroparticle, sorption equilibrium is assumed for the monomer and other species at the outer surface of the microparticles. This is followed by diffusion of these species through the semicrystalline polymer of the microparticles to catalyst sites located on the catalyst. Fragment energy balance is similar, except that heat is transported out from the catalyst fragment where the large heat of reaction is released, across the radius of the microparticle, through the pores and polymer at every radius of the macroparticle, and through the macroparticle boundary layer. Convective transport of heat and mass within the polymer particle is assumed to be negligible.

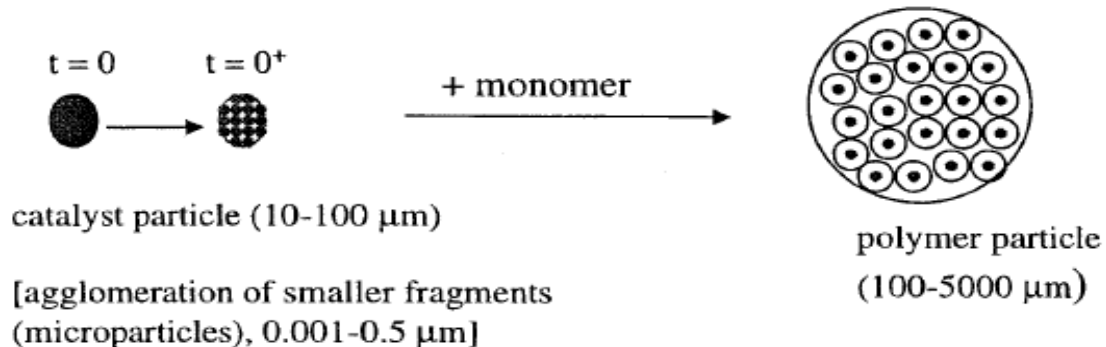


Figure 1. Catalyst fragments form microparticles, the building blocks of the entire polymer particle.

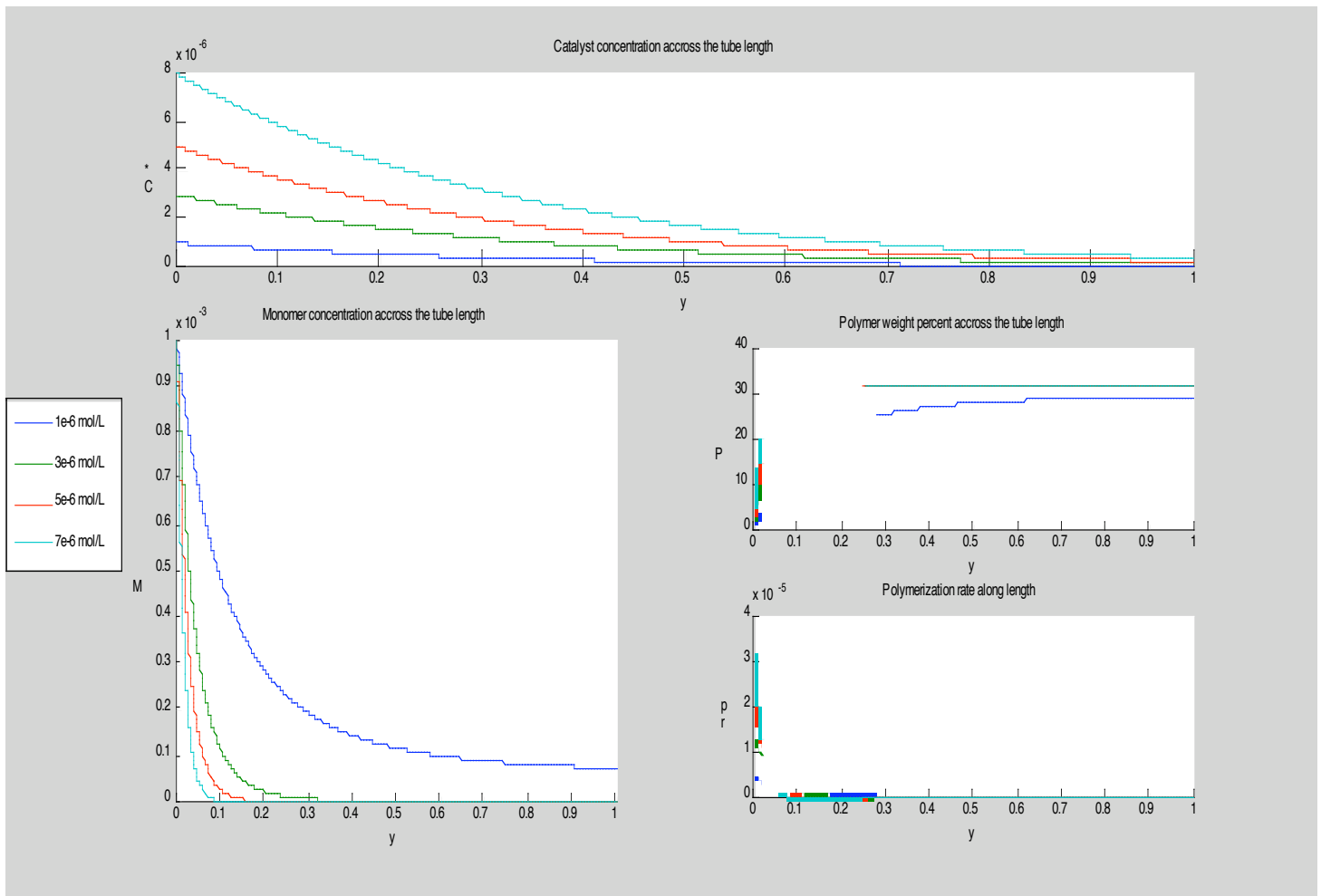


Figure 4. Results of varying the catalyst active site concentration.

Varying mean residence time

$T=70^{\circ}\text{C}$

Initial Catalyst Concentration= 10^{-6} mol/L

Initial Monomer Concentration= 0.001 mol/L

$k_p=4638.8$;

$k_d=0.0017$;

Length=1.5 m

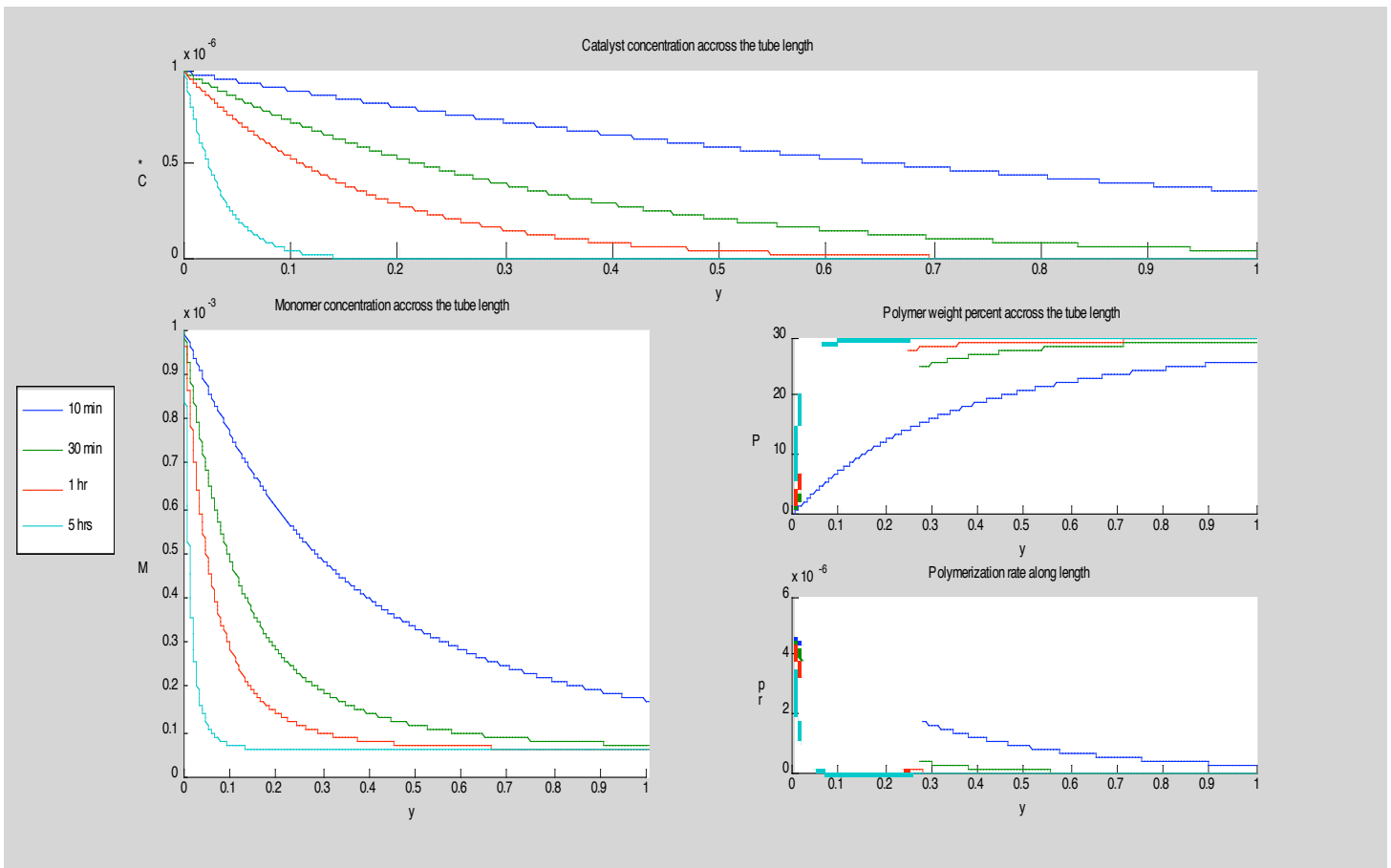


Figure 5. Results of varying mean residence time.

Unsteady state analysis of the reactor kinetics

$T=70^{\circ}\text{C}$
 Initial Monomer Concentration= 0.001 mol/L
 Initial Active Site Concentration= 10^{-6} mol/L
 $k_p=4638.8$;
 $k_d=0.0017$;
 Length=1.5 m
 Linear velocity=0.00083 m/sec

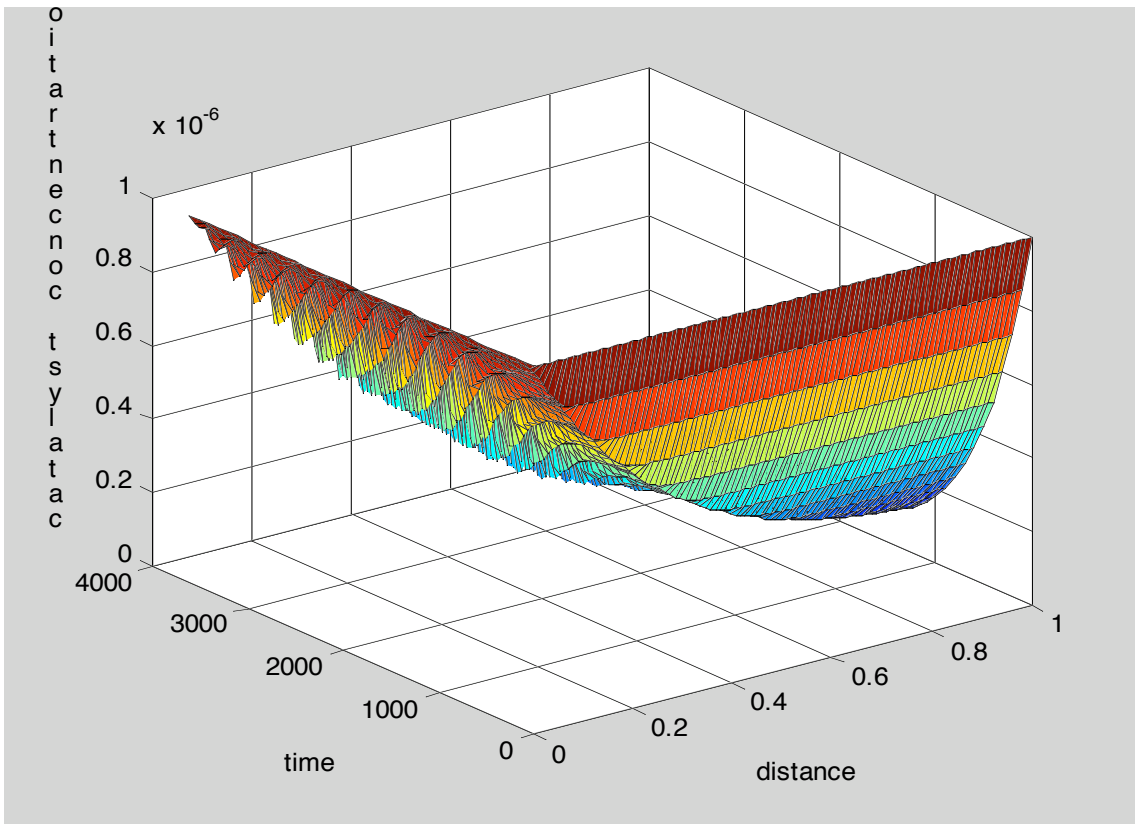


Figure 6. Catalyst concentration compared with time and distance.

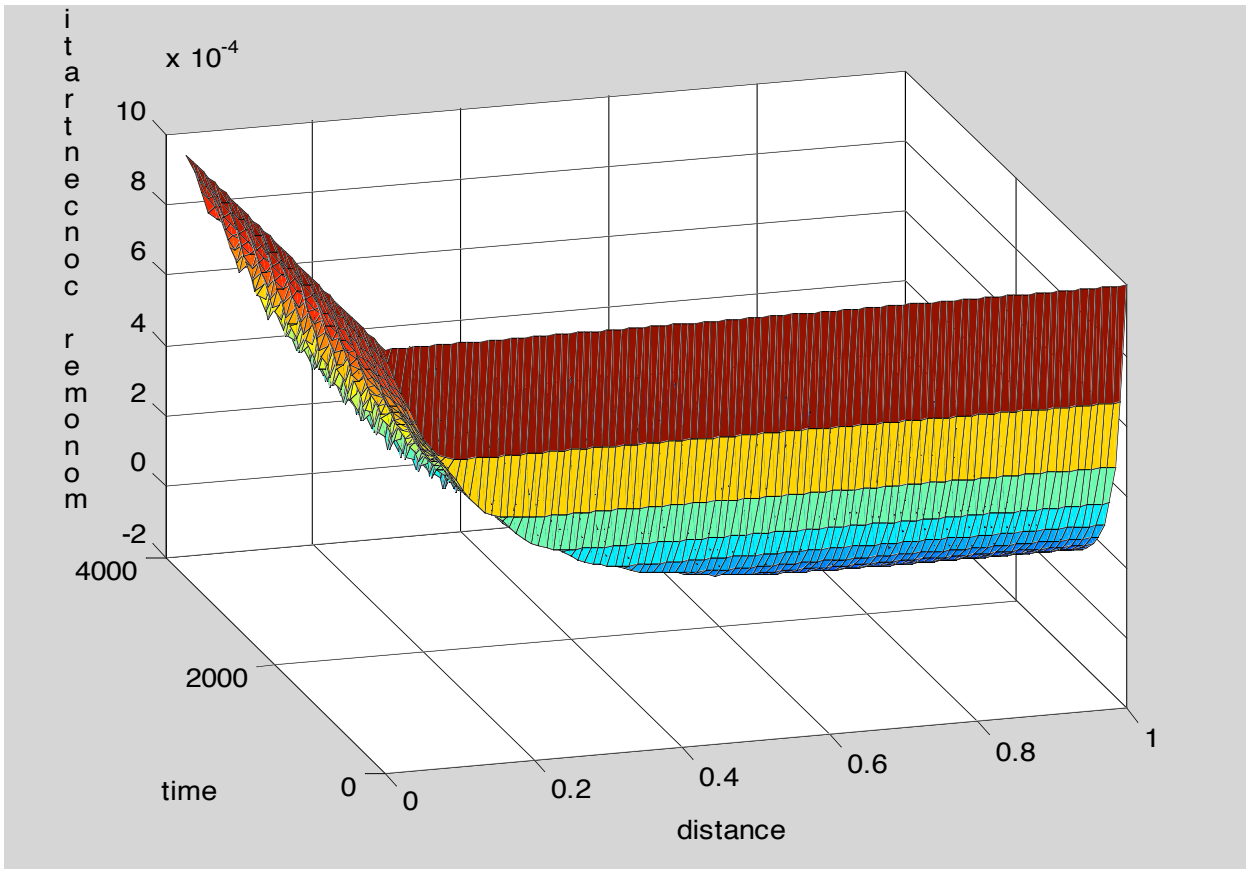


Figure 7. Monomer concentration compared with time and distance.

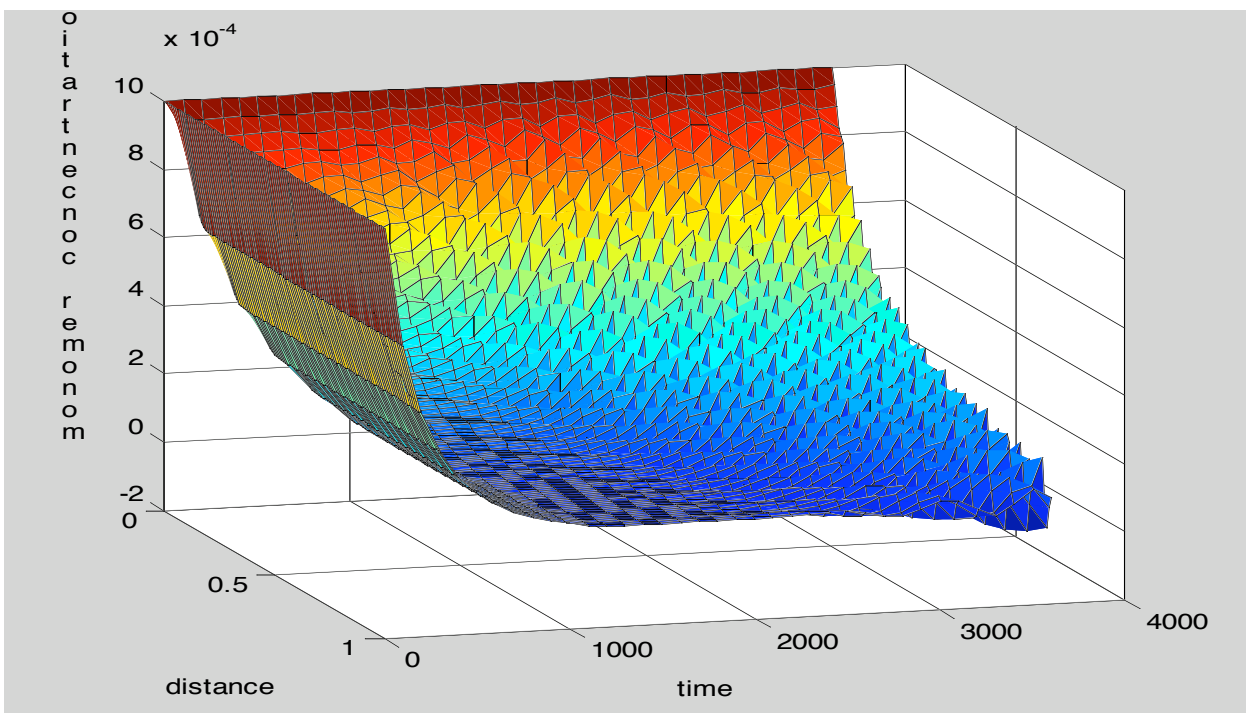


Figure 8. Monomer concentration compared with distance and time.

Molecular weight distributions:

W(r)- weight fraction

r-chain length

For Ethylene Polymerization @ 50°C using EBI catalyst– Kinetic Parameters:

$K_p=4638.8$

$K_{tm}= 0.72$

$[M]=0.001 \text{ mol/L}$

$\zeta=1.5521e-004$

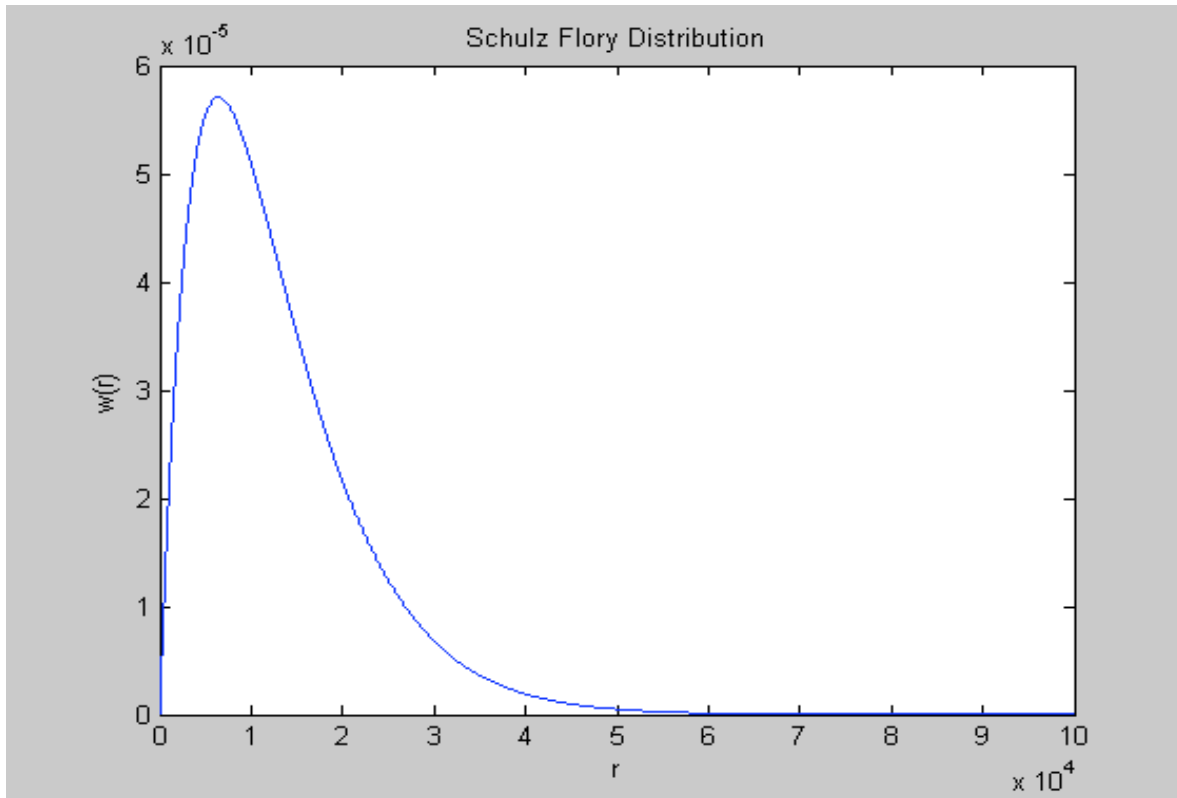


Figure 9. Molecular weight distribution.

Molecular Weight Distribution from solving of moment equations:

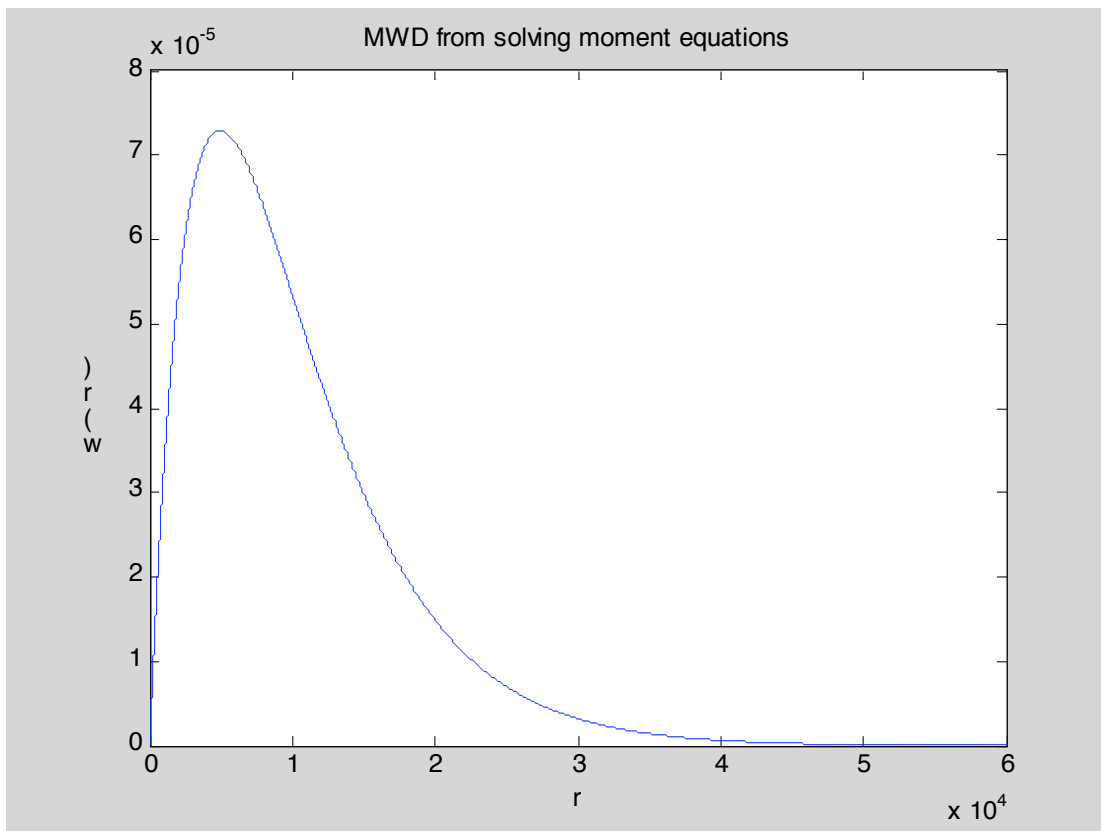


Figure 10. Molecular weight distribution from solving moment equations.

Silica Support Particle Synthesis

Prepared using measured quantities TEOS, ethanol, ammonia and water. The particles were viewed under SEM.

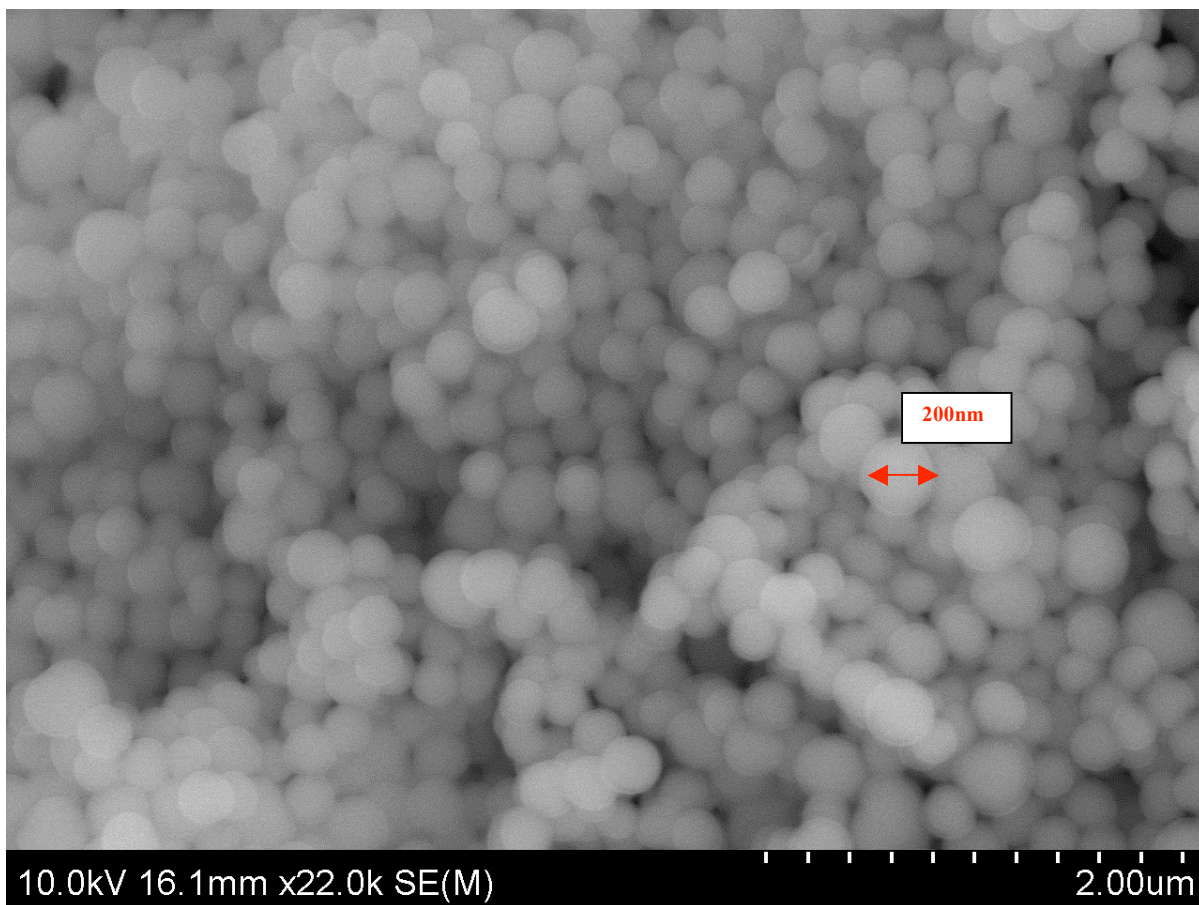


Figure 11. SEM image of silica support particles.

4. Difficulties Encountered/Overcome

- Production of large amount of catalyst support particles is material intensive.

5. Planned Project Activities for the Next Quarter

- Synthesizing more silica particles and analyzing pore structure and surface area of silica support
- Support catalyst onto silica
- Building the micro reactor set-up and running experiments and simultaneously validating a model.
- Continue the polymerization modeling for additional analysis like heat transfer and particle modeling.

Appendix

Justification and Background

Microreactors form a basis for the potential future downscaling of existing chemical processes, allowing tremendous reductions in capital and operating cost. They provide finer control of conditions, allow for faster process times, and improve safety in operation. Also, they should not encounter a significant problem in scaling from laboratory-sized systems to commercial-sized systems, since their operating principle will simply allow them to be stacked together modularly.

Of critical importance to the microreactors' capability to make the jump into industrial applications is the mixing efficiency, which controls the reaction rates and the yield expected from a reactor. Due to the scale of the systems, laminar flow is almost always encountered, which means that the vortices typically associated with turbulent flow are often missing. Instilling vortices into the flows to encourage mixing is accordingly a matter of construction of mixer channels.

Correct design parameters of microreactor influence the process yield. Designing microreactor for appropriate reaction conditions is very important for the reactions to be fast. Microreactors can be energy efficient too by appropriately designing and visualizing heat transfer. The channel dimensions have direct impact on diffusive mixing of reactants.

Approach

- Literature survey of the microreactor technologies as well as microchannel fabrication technologies.
- Selection of the target process for realization in microreactors with maximum benefit.
- Selection of microchannel fabrication technology suitable for microchannel mass production.
- Design and fabrication of a microreactor using microchannel fabricating technology suitable for mass production.
- Microreactor demonstration.
- Prepare experimental set-up and conduct the experiments.

Two-Year Schedule

Year 1:

- Conduct literature review to study current technologies for microreactors, micromixers, and incorporation of catalysts into microreaction technology.
- Evaluate existing microchannel formation techniques and their applications to microreactor construction.
- Selection of the target process for realization in microreactors with maximum benefit to ADNOC.
- Selection of microchannel manufacturing process most suitable for mass production.
- Preparation of a microreactor testing facility.
- Visualization study of mixing in microchannels.

Year 2:

- Literature survey of the olefin polymerization technologies focus on microchannels
- Selection of the target polymerization process for realization in microreactors with maximum benefit.
- Design and fabrication of a microreactor capable of realization of selected polymerization process

- Select type and size of catalyst particles to be used in the process
- Investigate propagation of selected catalyst particles in microchannels
- Investigate polymerization and polymer particle behavior in microchannels
- Parametric study of polymerization process at different temperatures, catalyst and reactant concentration.
- Microreactor demonstration.
- PI-side participation:
 1. Selection in cooperation with Borouge of the catalyst for the target polymerization process for realization in microreactors.
 2. Prepare a microreactor testing facility.
 3. Visualization study of mixing in microchannels
 4. Combine PI/UMD testing of the microreactor
 5. Microreactor demonstration to ADNOC representatives
 6. Prepare final project report and recommendations.

References

[1] Daryoosh Beigzadeh, Charles A. Nielsen, Study of Ethylene Polymerization Under Single Liquid Phase and Vapor-Liquid Phase Conditions in a Continuous-Flow Tubular Reactor, Chem. Eng. Technol. 2007, 30, No. 8, 1088–1093.

[2] A. B. Pangborn et al., J. Organomet. 1996, 15, 1518.

[3] Joˆao B. P. Soares, Mathematical modelling of the microstructure of polyolefins made by coordination polymerization: a review, Chemical Engineering Science 56 (2001) 4131–4153

[4] S. D. NAIK, W. H. RAY ,Particle Morphology for Polyolefins Synthesized With Supported Metallocene Catalysts

[5] Seung Young Park and Kyu Yong Choi ,Kinetic Modeling of Ethylene-Norbornene Copolymerization Using Homogeneous Metallocene Catalysts, Macromolecules 2003, 36, 4216-4225



Thrust 3
Energy System Management

Integration of Engineering and Business Decisions for Robust Optimization of Petrochemical Systems

UMD Investigators: Shapour Azarm, P.K. Kannan
PI Investigators: Ali Almansoori, Saleh Al Hashimi
UMD GRA: Weiwei Hu
PI GRA: Adeel Butt
Acknowledgement: Zhichao Wang, Khaled Saleh
Start Date: Oct 2006

1. Objective/Abstract

The overall objective of this project is to develop a framework for integrating engineering and business decisions. In view of this objective, a robust decision support system is being developed that can be used for multi-objective and multi-disciplinary optimization and sensitivity analysis under interval uncertainty for oil, gas and petrochemical systems. Our progress in this quarter is as follows. Our research continued on developing a meta-modeling assisted Multi-Objective Robust Optimization (MORO) approach with both reducible and irreducible interval uncertainty. A framework for this new approach (i.e., meta-model assisted MORO) was laid out which can be used for petrochemical process optimization with computationally expensive simulations. One advantage of this new approach is that it improves the previously reported MORO approaches by considering both reducible and irreducible interval uncertainty. A numerical example was used to demonstrate the applicability of this new approach and the solutions from the new approach were compared well with the solutions from a previous approach.

In terms of our progress for the dashboard, we developed an improved decision support system for a notional refinery plant. The improved dashboard can be used to determine parameters for a plant simulation in order to reduce the difference between the simulated plant performance and real plant performance. A case study adapted from a previously developed oil refinery business and engineering simulation model was used to demonstrate the proposed technique for a dashboard. The case study shows that the difference between the simulated and real profits progressively reduces as the crude oil price is iteratively updated. Finally, the HYSYS simulation model of an o-xylene oxidation process for producing phthalic anhydride has been further revised.

2. Deliverables for the Completed Quarter

- Developed and under implementation is a new Kriging meta-model assisted optimization approach for Multi-Objective Robust Optimization (MORO) with both reducible and irreducible interval uncertainty:
 - Extended the previous MORO approaches by applying interval uncertainty reduction on parameters with reducible uncertainty.
 - Significantly reduced computational cost in MORO by applying online meta-modeling to both objective and constraint functions.
 - Applied the newly developed approach on both numerical and engineering examples.
 - Completed a draft paper based on the newly developed optimization approach. This paper is currently under revision and preparation as a journal article.

- Proposed a decision support model with a dashboard-like interface for a notional refinery problem that can be used for adjusting/predicting critical parameters in a simulation model:
 - Provided a technical basis to adjust simulation parameters in order to match the simulated performance of a notional refinery model with its “real” performance.
 - Improved the decision support role of the previously developed dashboard for a notional oil refinery model.
 - Demonstrated/verified the working of the proposed decision support model with a notional oil refinery case study.
- Revised/implementing the HYSYS simulation model of an o-xylene oxidation process for producing phthalic anhydride
 - Simulated a reactor for the case of maximum possible conversion of o-xylene.
 - Adjusted o-xylene to air ratio as per commercial requirements.
 - Recovered maximum possible o-xylene in the recycle stream, which is connected to the inlet of the plant.
- Progress on joint publications:
 - Conference paper:
 - [1] Hu, W., Azarm, S. and Almansoori, A., 2010, "Approximation Assisted Multi-objective collaborative Robust Optimization (AA-McRO) under Interval Uncertainty," 13th AIAA/ISSMO Multidisciplinary Analysis and Optimization Conference, Fort Worth, TX.
 - Journal Paper:
 - [2] Hu, W., Azarm, S. and Almansoori, A., 2010, "On Improving Multi-Objective Robust Optimization Under Interval Uncertainty Using Worst Possible Point Constraint Cuts," ASME Journal of Mechanical Design (forthcoming).
 - [4] Hu, W., A. Almansoori, Kannan, P.K., Azarm, S. and Wang, Z. 2010, "Corporate Dashboards for Integrated Business and Engineering Decisions in Oil Refineries: an Agent-Based Approach" Decision Support Systems, submitted (under revision).
 - Working Journal paper:
 - [5] Hu, W., Azarm, S. and Almansoori, A., 2011, "Uncertain Interval Reduction Approach with Multi-Objective Robust Optimization with Online Approximation," to be submitted.
 - [6] Hu, W., Azarm, S. and Almansoori, "Approximation Assisted Multi-objective collaborative Robust Optimization (AA-McRO) under Interval Uncertainty," to be submitted.

3. Summary of Project Activities for the Completed Quarter

PI-UMD meetings during the seventh quarter included the following:

- Three teleconference meetings were held between PI and UMD research collaborators on January 18, February 22 and March 14, with SKYPE (first two meeting) and Adobe Connection (last meeting). Highlights of those meetings are:
 1. Research progress from both PI and UMD research teams were reported and reviewed;
 2. The integrated business and engineering model was reviewed with respect to its applicability to ADNOC;
 3. The improvement in HYSYS simulation model for producing phthalic anhydride from o-xylene was discussed. Furthermore, PI's progress on developing a new heat-integrated HYSYS model based on the current simulation was discussed;
 4. A newly developed Kriging meta-model assisted MORO with both reducible and irreducible interval uncertainty was presented by UMD, and plans were made to demonstrate the new approach with the improved HYSYS simulation model;
 5. With respect to the reviewers' comments on the paper submitted to the Journal of Decision Support Systems, plans were made on improving the paper and addressing the comments. In particular, an improved decision support model was devised.

Research efforts in this quarter are as summarized in the following:

Developing a new meta-model assisted optimization approach for Multi-Objective Optimization (MORO) with both reducible and irreducible interval uncertainty

Uncertainty in most petrochemical processes can be classified into two types: irreducible and reducible. Irreducible uncertainty is caused by the inherent uncertainty or variation in the process. For example, uncertainty in a raw material property or composition is inherently irreducible. However, reducible uncertainty is due to a lack of sufficient information or knowledge about the process. For example, measuring the temperature inside a distillation column can have uncertainty. This uncertainty is reducible, since using a more accurate thermometer or increasing the frequency of measurement or using a more expensive measurement device can reduce such uncertainty. Both irreducible and reducible uncertainties may create undesirable variations in system performance (or output) of the process. To get around such variations, researchers have developed robust optimization techniques. Basically, robust or robustness implies that the system's controllable parameters (or decision variables) are set so that performance is relatively insensitive to input uncertainty. In robust optimization, the system performance is not only optimized but also the variation in the performance is kept within an acceptable range, as we elaborate next.

Objective and feasibility robustness

Robustness is a term referring to a system that is insensitive to uncertain parameters. In MORO, robustness implies that under interval uncertainty i) variation in each objective function should not exceed an Acceptable Objective Variation Range (AOVR), i.e., objective robustness; ii) variation in the requirement should maintain feasibility of the system, i.e., feasibility robustness. The concept of objective and feasibility robustness is shown in Figure 1 using a one-variable objective function f and constraint g . The goal is to minimize f subject to $g \leq 0$ with interval uncertainty in x , represented by the grey bar shown on the x -axis. In Figure 1 (a), point I is identified as the global optimum solution. However, with interval uncertainty in x and the given AOVR for f , only point III is robust. For the constraint function shown in Figure 1(b), all points within the interval formed by points I to III satisfy feasibility robustness because even when there is uncertainty in x , the variation in g will not violate the feasibility requirement, i.e., $g \leq 0$. On the other hand, assuming uncertainty in x is reducible, then both points I and II may potentially become a robust solution with respect to the objective function f as the uncertain interval is reduced. However, point II is more likely to be the robust optimum solution since objective function variation at point II is much less compared to the objective function variation at point I.

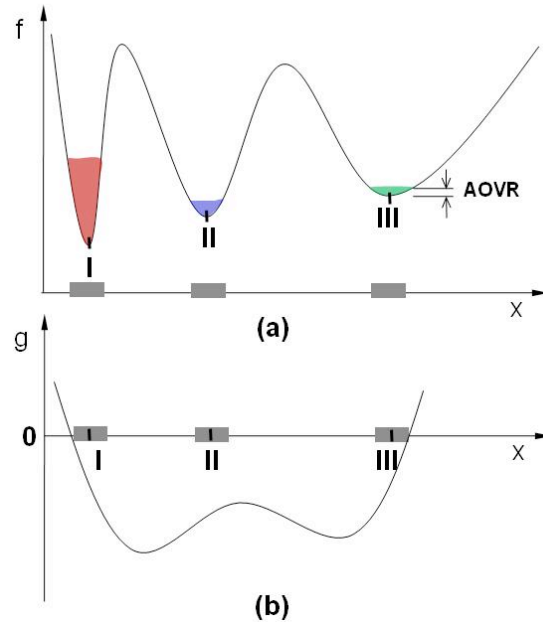


Figure 1. Objective and feasibility robustness.

Reducible uncertainty and uncertain interval reduction

Let x be a variable with reducible uncertainty; the nominal lower and upper bounds for the uncertainty in x are denoted by x^L and x^U . Now assume the interval uncertainty in x is reduced: we use αx^L and αx^U to represent the reduced lower and upper bounds for x , or $x \in [\alpha x^L, \alpha x^U]$, as shown in Figure 2. Particularly, α is called the uncertainty reduction index, which is used to indicate how much uncertainty can be reduced. It is easy to show that $0 \leq \alpha \leq 1$. Conceptually, as the value of α is reduced, the range of uncertainty is also reduced. For example, when $\alpha = 1$, the uncertain interval for x is at the nominal (not reduced); when $\alpha = 0.5$, the uncertain interval for x is reduced by fifty percent; when $\alpha = 0$, the uncertain interval in x is completely eliminated. As mentioned before, to reduce uncertain interval for x , it is necessary to make investment: for example, by purchasing better equipment for measuring the temperature, which will reduce uncertainty in the value of the temperature measured. Note that the more expensive the equipment the less the uncertainty (smaller tolerance) and the more accurate the temperature measurement. Since more investment is required to reduce an uncertain range, it can be expected that α is inversely proportional to the investment for uncertainty reduction.

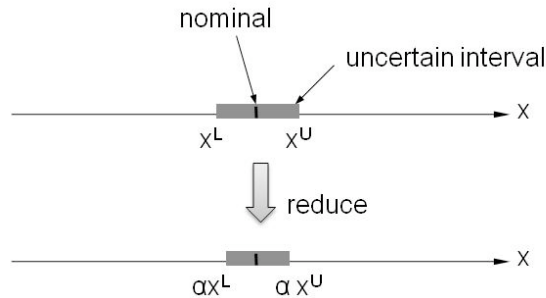


Figure 2. Uncertain interval reduction for reducible uncertainty.

MORO under both reducible and irreducible uncertainty

MORO with both reducible and irreducible uncertainty can be computationally expensive because the robustness for each alternative should be verified, as shown in the double loop in Figure 3. To

reduce the computational cost, we combine online approximation with the optimization approach. To do this, we approximate all objective functions and constraints using online meta-modeling. The approach for MORO under both reducible and irreducible uncertainty with online approximation consists of four blocks, as shown in Figure 3. The approach starts with an initial set of sample points which can be generated offline using Maximum Entropy Design (MED) [15]. The offline sample points are used for building an initial meta-model for each objective/constraint function. Next, the meta-model based optimization problems are solved. The obtained optimal solutions (as shown by the Pareto frontier in objective space) are combined with previous samples in the online sampling and validation block. Finally, a filtering and validation procedure is used to prevent crowding of sample points and to verify that predicted errors for meta-models are within an acceptable threshold. After sample points are updated, the control returns to the meta-modeling block and previous meta-models for the objective functions and constraints are updated. The iterations among meta-modeling, MORO under reducible and irreducible uncertainty, and online sampling and validation blocks will continue until predefined stopping criteria are satisfied.

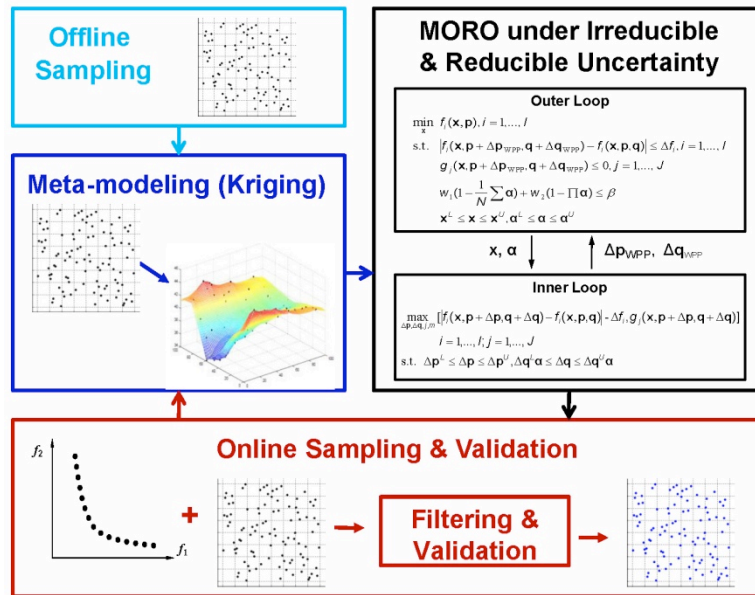


Figure 3. MORO approach with online approximation.

Demonstrative example

We use a numerical example to demonstrate the meta-model assisted approach for MORO with both reducible and irreducible uncertainty. The problem formulation is shown in the following:

$$\begin{aligned}
 & \min f_1 = x_1 \\
 & \min f_2 = x_2 \\
 & \text{s.t. } g_1 = 1 + 0.1 \cos(16 \arctan \frac{x_1}{x_2}) + \\
 & \quad 0.2 \sin(p_1) \cos(p_2) - x_1^2 - x_2^2 \leq 0 \\
 & \quad g_2 = (x_1 - 0.5)^2 + (x_2 - 0.5)^2 \leq 0 \\
 & \quad 0 < x_1, x_2 \leq p;
 \end{aligned}$$

The problem is to minimize the objective functions f_1 and f_2 , subject to constraints g_1 and g_2 . Note that uncertainty exists in two parameters p_1 and p_2 , whose nominal values are zero. The lower

and upper bounds of uncertain interval for both parameters are -2 and 2, respectively. The lower and upper bounds for design variables x are given in the formulation. Since constraints in this example have uncertainty but the objective functions do not, we only consider feasibility robustness. To show the effectiveness and computational efficiency of the online meta-modeling approach, we compared two sets of solutions. One set was obtained with online meta-modeling, while the other was obtained without online meta-models, i.e., using a previous approach. These solutions are plotted in the objective space formed by f_1 and f_2 in Figure 4. The feasible domain is defined by the area between g_1 and g_2 . It can be seen that the optimum solutions from the proposed online meta-modeling assisted approach are comparable with the previous approach. However, there is a significant difference between the two approaches in terms of computational costs. That is, the total number of function calls for the meta-model assisted approach is only 111, while for MORO without online meta-models the total number of function call is 4,682,872. Additionally, the deterministic optimum solutions to the problem are also obtained and plotted in Figure 4. Notice that because of the non-convexity of g_1 , the Pareto frontier of the deterministic solutions as shown by the star symbols consists of three discontinuous sections along g_1 . Compared to the deterministic solutions, the two sets of robust solutions are slightly inferior because of the uncertainty.

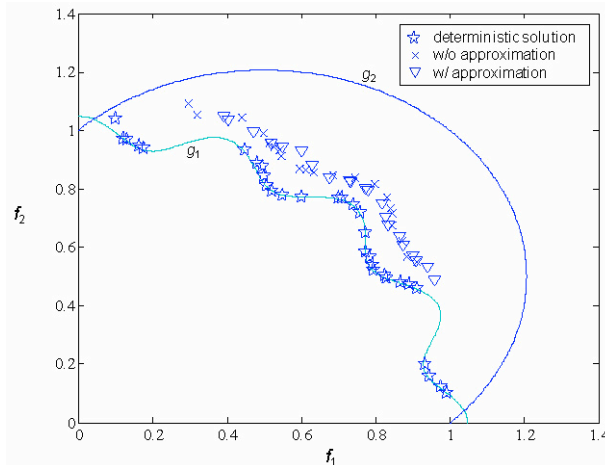


Figure 4. Comparing MORO solutions with and without approximation

Finally, since Kriging meta-models are used to approximation both constraint functions, we also validated the errors of these meta-models. It was found that the relative root mean square error and the relative maximum absolute errors for g_1 and g_2 are less than 0.1 and 0.2 (the maximum acceptable errors), respectively.

Improving decision support model behind dashboard

In an integrated decision support framework, the dashboard provides an interface between the decision maker (e.g., management) and plant/firm's simulation, as shown in Figure 5. More specifically, the dashboard is used to show the state of Key Performance Indicators (KPIs) such as revenue, profit, customer service, quality indicators, etc. For example, profit from sales of an end product is an indicator of how efficiently the company is turning investment into net income and which products are driving profits. The expected values of the KPIs are obtained from the simulation model and the optimization results, while the current values of the KPIs are obtained from the firm-market interactions. The expected and actual values of the KPIs can be different due to an assumed value of uncertain parameters, e.g. the price of crude oil, in the simulation. Therefore, the DM, based on the expected KPIs from the optimization, the current KPIs, and the difference between these two values, will try to eliminate the differences by adjusting the assumed parameters in the simulation. The simulation-based optimization is then repeated according to the adjustments and it will suggest a new set of decisions for the decision maker. After the new decisions are implemented in the plant, it will produce a current KPI value

according to the firm-market interactions. As a result, the expected values and current values of KPIs may be changed. These changes and the differences between the expected and current KPIs are shown on the dashboard again, through which the DM repeats the adjustments until plant performance reaches an equilibrium state and the difference between the expected and current KPI values are within an acceptable range.

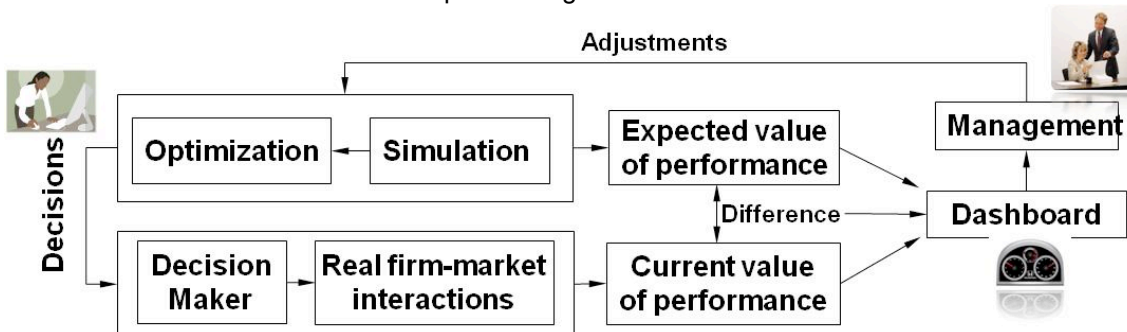


Figure 5. Decision support role of dashboard.

Case study

In our previous research on integrating business and engineering decisions, we identified the interactions between the business and engineering processes for a typical/notional oil refinery and successfully integrated the business and engineering models. This case study is intended to further demonstrate the procedure that a DM should follow in order to bring a simulated firm-market model close to a real one through adjustments in simulation parameters. In the case study, the business and engineering processes are developed in NetLogo (an agent-based simulator) and HSYSYS, respectively. These models can be used to simulate how a notional refinery model, as in this case study, will react (in terms of profit) to oil market price adjustments based a given set of plant decision variables.

In the case study, it is assumed that the DM needs to match the simulation profit with real profit by proper adjustment (or estimate) of the crude oil price, which is assumed to be a critical parameter in the integrated simulation model for estimating profit. For this study (and just for demonstration), it is assumed that crude oil price in the market is set at \$30/barrel. However, the oil price used in the simulation model is unknown *a priori* while it must be specified to obtain the expected profit. The approach helps the DM specify (or reduced the uncertainty) in the estimate of the oil price. For simplicity, suppose that the DM can pick one value from an action space consisting of four discrete values for the oil price, i.e., 30, 40, 50 and 60 dollars per barrel. Initially the DM's belief on the price is presumed to follow a uniform distribution, and thus the four discrete values have equal probability of being chosen. A reward function is defined based on the difference between the simulated profit and the real profit. The reward value is then used to update the probability distribution of the management's belief on the oil price iteratively until the difference between actual and simulated profit falls within a given threshold. Also notice that since the oil price can affect the profit obtained from the simulation model, the price choice may change as the simulation parameters are updated. Therefore, whenever the DM updates the oil price, an optimization based on the integrated simulation model should be performed to obtain the new set of optimized decision variables.

For demonstration, a total of 10 adjustment iterations are run, and the probability distributions for the management's belief on oil price for iteration 1, 5 and 10 are shown in Figure 6. Notice that as a result of iterative adjustment by the DM, the expected crude oil price is gradually approaching the true value, which is assumed to be \$30/barrel. Also in Figure 7, the simulated and real profit and the difference between them are shown. It is noted that the difference between the simulated and real profit for iteration 1 is significant. However, as the DM adjusts the crude oil price, this difference is reduced. After 10 iterations, the difference is very small, and it is reasonable to assume that the simulated profit is consistent with the real profit.

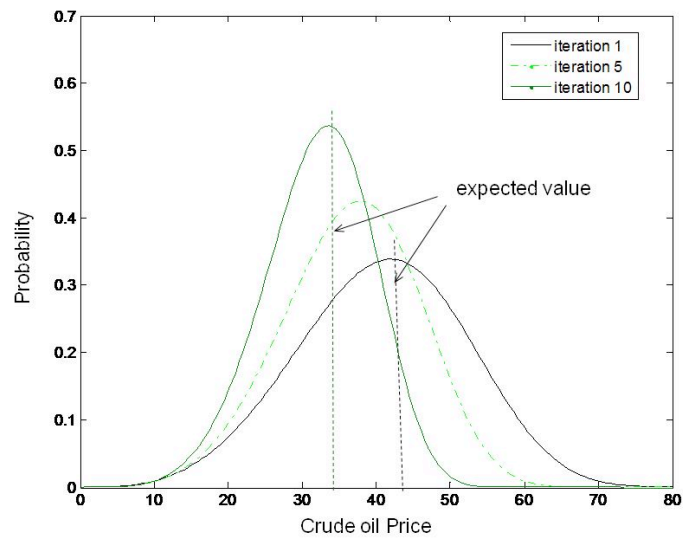


Figure 6. Iterative adjustment of probabilistic distribution of oil price.

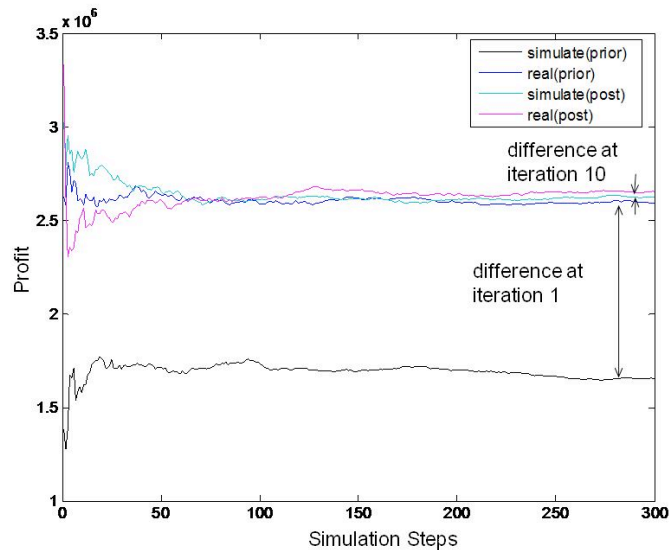


Figure 7. Simulated and real profit at iteration 1 and iteration 10.

4. Difficulties Encountered/Overcome

In developing a decision support model for the DM to adjust the simulation parameters, the real plant performance is also obtained from the simulation model because the real refinery data is not available. However, when the proposed framework is implemented in an actual refinery, the real data can be obtained from the refinery and used instead. On the other hand, the simulation model contains many parameters. All parameters may have an important role on the performance of the refinery. At this time, we are not able to consider many parameters in the proposed approach because of the complexity of the problem. Instead, we only chose one such parameter, i.e., the crude oil price, to demonstrate how adjustment on the parameter can improve the simulation model so that it matches the real oil refinery performance in terms of profit. We plan to explore

the proposed approach further and provide additional insights in our future investigation. The demonstrated results in this report were our first attempt on the proposed improved research directions.

5. Planned Project Activities for the Next Quarter

- Implement the new meta-model assisted MORO approach with reducible and irreducible uncertainty on a chemical engineering example (HSYSY model for o-xylene oxidation process).
- Develop a heat-integrated simulation process using HSYSY and increase complexity to the current process by considering its applicability to ADNOC companies.
- Continue developing an agent-based market model and integrate the model with the revised engineering model. Revise dashboard based on the new integrated business and engineering models.
- Revise and submit the paper for the Journal of Decision Support System. Complete and submit the working papers.

Appendix

Justification and Background

Many oil, gas and petrochemical systems involve numerous coupled subsystems. These systems and their subsystems usually have uncertain inputs and thus it can be difficult to make the “best” engineering and business decisions in terms of independent operations of these complex systems. It becomes even more difficult to make those decisions when the system consists of many units or plants producing different products. This difficulty presents an opportunity taken on in this project. A review of mainstream literature has revealed that previous models in management of petrochemical systems have been based on either engineering or business decisions but not both. There is a significant gap in the literature as to how these two types of decisions should be devised and integrated. To address this important gap, the focus of this investigation is to develop an integrated robust decision support framework considering both engineering and business models under uncertain conditions. Our overall objective has several underlying research questions, including: (i) how to develop business models that include management decisions in a multi-unit organization and at the same time account for engineering aspects; (ii) how to determine the relative importance and effects of uncertain system and/or subsystem input parameters on subsystem and/or system outputs (e.g., system performance); (iii) how to define a set of metrics, by way of a dashboard, that will serve as a visualization tool to keep track of a company’s financial status in view of competition and market systems and provide for easy communication between various levels in the company, and (iii) how to extend our current single-level robust optimization method to multi-subsystem problems and maintain reasonable computational complexity for the method. These underlying questions and corresponding investigations will be organized into tasks throughout the time frame allocated to the project. The details of these tasks are explained in the next section.

Approach

There are two main tasks in this investigation as detailed in the following.

Task 1 (PI):

Develop and implement engineering analysis models, in a Matlab (or Matlab compatible) environment, for a crude distillation unit case study model.

- Task 1.1: Develop a multi-input multi-output analysis model for a representative petrochemical system with corresponding subsystem analysis models.
- Task 1.2: Extend the analysis model in Task 1.1 to include: (i) additional complexity, (ii) subsystem details and uncertainty to include reasonable representation of engineering side of a plant. The ultimate goal is to develop an integrated multi-subsystem petrochemical analysis model for a plant or a group of units in a plant.

Task 2 (UMD):

Develop and implement a Robust Decision Support System (RDSS).

Engineering Tasks

- Task 2.1: Develop a single level (all-at-once) approximation-assisted robust optimization technique that is able to significantly reduce the computational efforts of making robust decisions.
- Task 2.2: Demonstrate an application of the approach from Task 2.1 with a case study in petrochemical systems which will be developed by PI as a part of Task 1.
- Task 2.3: Develop an approximation assisted multi-objective multi-disciplinary robust optimization approach, which is an extension to Task 2.1.

- Task 2.4: Demonstrate an application of the approach from Task 2.3 with a case study in petrochemical systems which will be developed by PI as part of Task 1.

Business Tasks

- Task 2.5: Develop business models in Netlogo and/or Matlab and solve a simplified refinery supply chain optimization problem with Matlab.
- Task 2.6: Develop a Dashboard and test the robustness and sensitivity of the Dashboard's elements for the model in Task 2.5.

Integration Tasks

- Task 2.7: Inspect engineering and business problems to determine coupling variables between two problems.
- Task 2.8: Integrate Tasks 2.1 to 2.4 with Tasks 2.5 to 2.6 to formulate a refinery optimization problem that considers both engineering and business objectives and constraints.
- Task 2.9: make the supply chain management problem more realistic by considering more decision levels, more finished products and a wider market, and by increasing the size of the refinery's internal network and then repeat Task 2.8.
- Task 2.10: Verify and validate the integrated model.

References

- [1] Anderson, S. P., Palma, A.d., and Thisse, J., 1992, "Discrete Choice Theory of Product Differentiation", Cambridge, MA, MIT Press, 1992.
- [2] Aspen HYSYS, 2009, <http://www.aspentech.com>, Aspen Technology.
- [3] Deb, K., 2001, Multi-Objective Optimization using Evolutionary Algorithms, John Wiley & Sons, Ltd, New York.
- [4] Douglas, J.M., 1988, "Conceptual Design of Chemical Processes", McGraw-Hill, New York, USA.
- [5] Forbes, R.J., 1948, "Short History of the Art of Distillation", Brill, Leiden, Holland.
- [6] Gargeya, V., 2005, "Plant Level Performance Measurement: An Exploratory Case Study of a Pharmaceutical Encapsulation Company", *Technovation*, 25(12), 1457-1467.
- [7] Gattu, G., Palavajjhala, S., and Robertson, D., 2003, "Are Oil Refineries Ready for Non-Linear Control and Optimization?" International Symposium on Process Systems Engineering and Control, Mumbai, India.
- [8] Grossmann, I. E., 2005, "Enterprise-Wide Optimization: A New Frontier in Process Systems Engineering," *AIChE Journal*, 51(7), p. 1846-1857.
- [9] Halemane K. P., Grossmann I. E., 1983, "Optimal Process Design under Uncertainty," *AIChE Journal*, 29(3), 425-433.
- [10] Hu, W., M. Li, S. Azarm, S. Al Hashimi, A. Almansoori, and N. Al Qasas, 2009, "On Improving Multi-Objective Robust Optimization Under Interval Uncertainty Using Worst Possible Point Constraint Cuts," *CD-ROM Proceedings of the ASME International Design Engineering Technical Conferences*, Aug. 30 – Sep. 2, San Diego, CA, USA.
- [11] Jackson, J., Hofmann, J., Wassick, J. and Grossmann, I., 2003, "A nonlinear multi-period process optimization model for production planning in multi-plant facilities", *Proceedings FOCAPO2003*, 281-284..
- [12] Janak, L., Lin, X. and Floudas, C. A., 2007, "A New Robust Optimization Approach for Scheduling Under Uncertainty: II. Uncertainty with Known Probability Distribution," *Computers and Chemical Engineering*, 31(3), 171-195.
- [13] Kaplan, R. and Norton, D., 1996, "Using the Balanced Scorecard As a Strategic Management System", *Harvard Business Review*, 74(1), 75-85.

- [14] Kleijnen, J. and Smits, M., 2003, "Performance metrics in supply chain management". *Journal of the Operational Research Society*, 54(5), 507–514.
- [15] Koehler, J.R., Owen, A.B., 1996, "Computer Experiments," *Handbook of Statistics*, Elsevier Science, New York. pp. 261-308.
- [16] Lin, X., Janak, S. L. and Floudas, C. A., 2004, "A New Robust Optimization Approach for Scheduling Under Uncertainty: I. Bounded Uncertainty," *Computers and Chemical Engineering*, 28(6-7), 1069-1085.
- [17] Li, M., and Azarm, S., 2008, "Multiobjective Collaborative Robust Optimization with Interval Uncertainty and Interdisciplinary Uncertainty Propagation," *Journal of Mechanical Design*, 130(8), pp. 081402-1-081402-11.
- [18] Li, M., N. Williams and Azarm, S., 2009, "Interval Uncertainty Reduction and Single-Disciplinary Sensitivity Analysis With Multi-Objective Optimization," *Journal of Mechanical Design*, 131(3), pp. 031007-1-031007-11.
- [19] Micheletto, S. R., Carvalho, M. C. A. and Pinto, J. M., 2008, "Operational Optimization of the Utility System of an Oil Refinery," *Computers and Chemical Engineering*, 32(1-2), 170-185.
- [20] Netlogo, <http://ccl.northwestern.edu/netlogo/>
- [21] Pinto, J., Joly, M. and Moro, L., 2000, "Planning and scheduling models for refinery operations", *Computers and Chemical Engineering*, 24(9), 2259–2276.
- [22] Sahdev, M., Jain, K., Srivastava, P., "Petroleum Refinery Planning and optimization Using Linear Programming", *The Chemical Engineers' Resource Page*, http://www.cheresources.com/refinery_planning_optimization.shtml
- [23] Simpson, T. W., and Mistree, F., 2001, "Kriging Models for Global Approximation in Simulation-Based Multidisciplinary Design Optimization," *AIAA Journal*, 39(12), pp. 2233-2241.
- [24] Suresh, S. Pitty, Li, W., Adhitya, A., Srinivasan, R., Karimi, A., 2008, "Decision support for integrated refinery supply chains", *Computer and Chemical Engineering*, 32, 2767–2786.

Dynamics and Control of Drill Strings

UMD Investigator: Balakumar Balachandran
PI Investigators: Hamad Karki and Youssef Abdelmagid
GRA: Chien-Min Liao (started in Spring 2007)
Start Date: Oct 2006

1. Objective/Abstract

Drill-string dynamics need to be better understood to understand drill-string failures, control drill-string motions, and steer them to their appropriate locations in oil wells. Although a considerable amount of work has been carried out on understanding drill-string vibrations (for example, Leine and van Campen, 2002; Melakhessou *et al.*, 2003; Spanos *et al.*, 2003; Liao *et al.*, 2009), the nonlinear dynamics of this system are only partially understood given that the drill string can undergo axial, torsional, and lateral vibrations, and operational difficulties include sticking, buckling, and fatiguing of strings. In addition, the prior models focus on either bending or torsional or axial motions. Hence, it is important to consider coupled axial-bending-torsional vibrations and contact instability in oil and gas well drilling. A better understanding of these vibrations can help keep the drill string close to the center of the borehole and help realize near-circular bores during drilling operations.

The overall goal of the proposed research is to understand the nonlinear dynamics of the drill string and develop a control-theoretic framework for its stabilization enabling energy efficient drilling with longer life span for the equipment. Specific research objectives of this project are the following: i) building on Phase I efforts, develop and study control-oriented models for the drill strings through analytical and numerical means, ii) investigate the control of an under-actuated nonlinear system (drill string) with complex interactions with the environment, and iii) use the drill-string test-beds constructed at the Petroleum Institute & the University of Maryland to validate the analytical findings and suggest possible strategies to mitigate drill-string failures in fixed and floating platform environments.

2. Summary of Results

The trajectory of a drill-string within a cross-section of the borehole is a useful method to monitor the system dynamics. Identifying rotor movements and observing the characteristic behaviors is a necessary step to generate systematic information for enhancing drilling operations. The authors also introduce a distributed-parameter model which may be useful for describing horizontal drill string dynamics. The model is first compared to experimental data from the vertical drill string experiment, and similar characteristics were observed in both the numerical simulations and the experiments.

The rest of this section is organized as follows. In Section 2.1, experimental results for different rotor trajectories are presented and discussed and characterized. In Section 2.2, a distributed-parameter model along with the new experimental configuration used to study horizontal drilling is presented. Section 2.3 contains current results and an outline of future work.

2.1 Experimental Studies

In this section, the experimental arrangement used for studying the drill-string system at different rotational speeds and with different system parameters is presented. Qualitative changes in the

system were observed with respect to changes in the following: i) driving speed of motor, ii) magnitude of unbalanced mass attached to the disc, and iii) friction coefficient between the outer shell and the disk at the bottom of the drill string.

2.1.1 Experimental Arrangement

In Figure 1 and Figure 2, the experimental arrangement is presented along with details used for studying the drill-string system for different combinations of the unbalanced mass and coefficient of the contact surface between the bottom disk and the outer shell. On the left-hand side of Figure 1 and Figure 2(a), a string with a bottom disc is illustrated. This system is driven by a motor with a constant rotating speed that ranges from 10 rpm (revolutions per minute) to 190 rpm. Generally, real field drill systems are driven at speeds under 300 rpm, and most of these drilling speeds are studied here. Five different levels of unbalanced mass attachments to the disc were used: 0.0 g, 28.1 g, 48.1 g, 61.7 g, and 87.1 g. The unbalanced mass may be viewed as being representative of the curvature of the drill string. For instance, the case of zero unbalanced mass corresponds to a straight drill string, while a non-zero unbalanced mass is representative of a drill string in a curved orientation. Due to changes in soil type and rock conditions with respect to the mine-hole depth, the friction coefficient between a drill bit and the borehole changes during the course of an operation. In order to mimic the physical conditions of “real drilling” and better understand the system dynamics, three different levels of friction coefficients were considered. The details of the bottom disc with outer shell are shown in Figure 2(c).

The images of the bottom rotor, which were captured by using a video camera, are shown in Figure 2(b). These images were used for monitoring the system response during the experiments. Rotor trajectories were traced and constructed by analyzing the location of the center of rotor in each video frame through a gradient-based image processing procedure. An example of a typical image of the rotor as seen from the camera is shown in the right-hand side of Figure 1(a) and 1(b). The rotor motions can be clearly seen as one goes from Figure 1(a) to Figure 1(b); the rotor is at a 3 o'clock position within the shell region in (a) and at a 12 o'clock position in (b). The capture rate from the camera is 110 FPS (frame per second), which is sufficient for capturing the response over the range of rotation speeds, which extend up to a maximum rotating speed of 190 rpm.

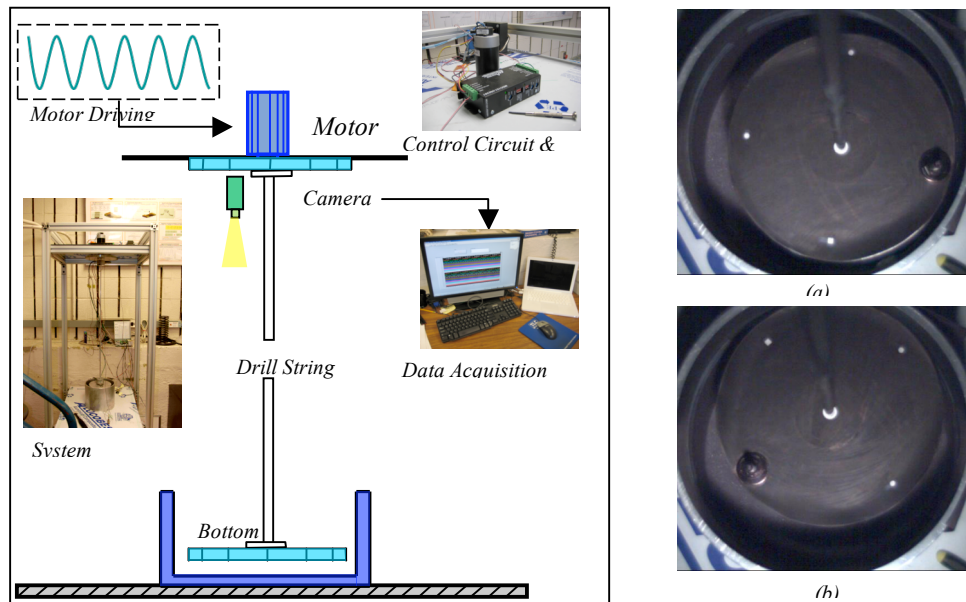


Figure 1. Schematic of experimental setup and (a) and (b) sample video output.

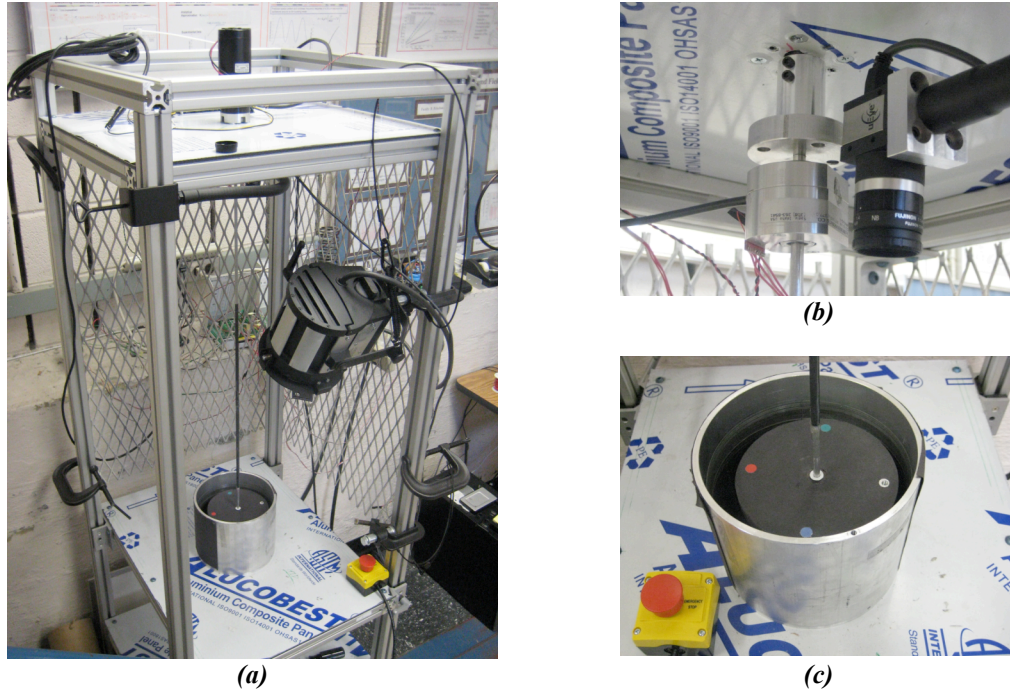


Figure 2. Experimental setup with details: (a) system overview, (b) camera and encoder, and (c) test platform: disc with outer shell.

2.1.2 Experimental Results

As shown in the previous report, the rotor motions can change quite significantly with increase in driving speed. One of the aims of this report is to explore these motions further by studying the rotor trajectory characteristics in different phases. The first phase is characterized by rotor motions around the center of the shell. In a subsequent phase, the rotor changes to bumping motions, which can lead to forward whirling. Details of these two phases are provided in Figure 3 and Figure 4.

A rotor trajectory for a case with 28.1 g unbalanced mass, aluminum–aluminum contact surface between the rotor and outer shell, and a driving speed of 37.5 rpm is illustrated in Figure 3(a). The rotor trajectory in this case exhibits no bumping between rotor and shell. The time history of the radial displacement in Figure 3(b) also shows no contact between the rotor and shell since the displacement is around 0.01 m; this magnitude is smaller than the shell edge located at around 0.02 m. The radial velocity amplitude in Figure 3(c) is of small magnitude, since the driving speed is at a slow speed. The displacement components of the rotor along the normal and tangential directions are sinusoidal in nature and have a phase difference with respect to each other; the corresponding frequency spectra of Figure 3(d) show a clear response peak at the motor driving frequency.

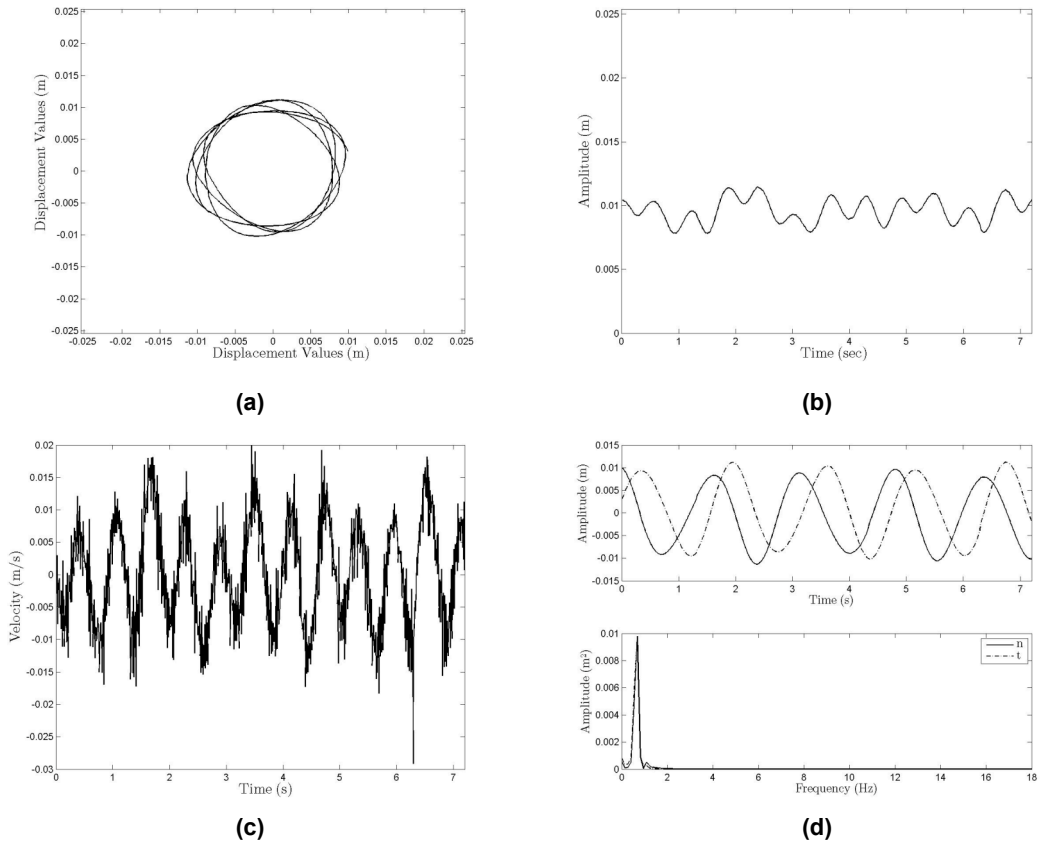


Figure 3. Rotor response for rotation speed of 37.5 rpm with aluminum-aluminum contact: (a) rotor trajectory, (b) radial displacement history, (c) variations of normal and tangential speeds, and (d) normal and tangential displacement histories (top) and corresponding frequency spectra (bottom).

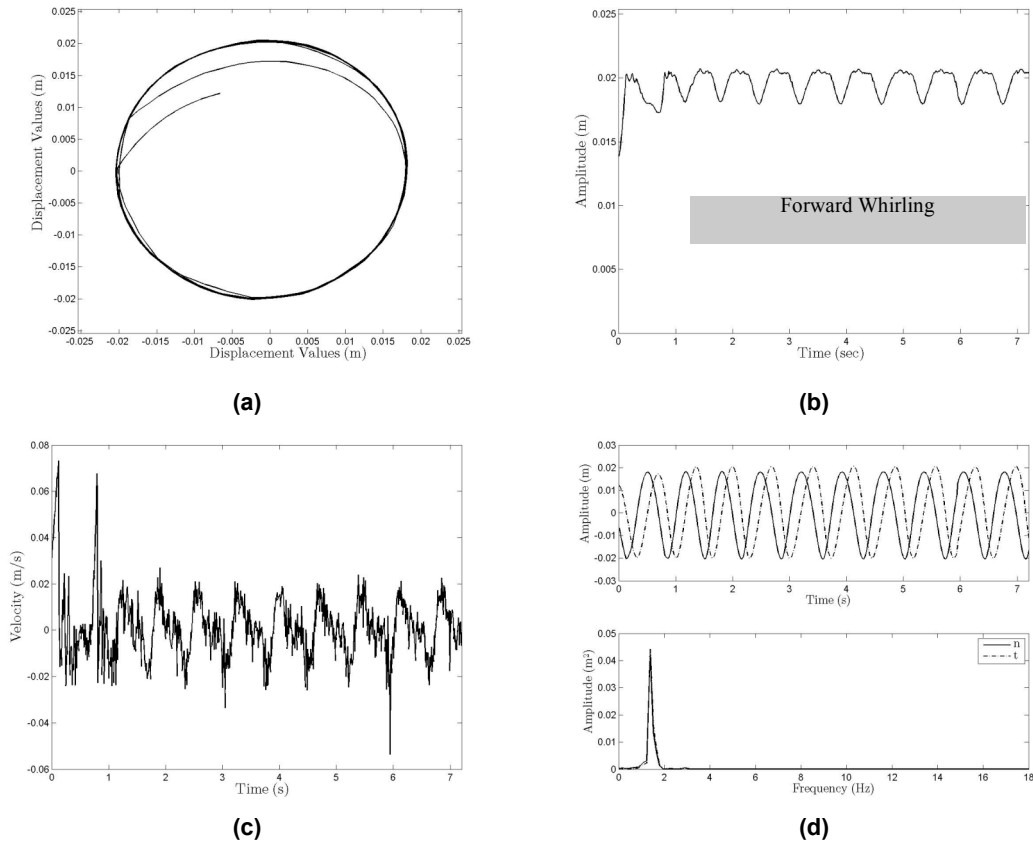


Figure 4. Rotor response for rotation speed of 83.1 rpm with aluminum-aluminum contact: (a) rotor trajectory, (b) radial displacement history, (c) variations of normal and tangential speeds, and (d) normal and tangential displacement histories (top) and corresponding frequency spectra (bottom).

With an increase in rotating speed, the rotor goes into a bumping and forward whirling phase. The rotor trajectory of Figure 4(a) shows more than two impacts with the outer shell before exhibiting forward whirling. In forward whirling, the radial displacement history is sinusoidal in nature with a small amplitude and a DC offset close to the outer shell during forward whirling (see for example, Figure 4(b)).

In Figure 4(c), the first two peaks in radial velocity time history occur when the rotor bumps into the shell. When the rotor goes into forward whirling right after the impacts, the radial speed reduces to zero. It should be noted that the velocity amplitude of the forward whirling phase is lower than that observed during the bumping stage. In Figure 4(d), the frequency spectra are shown. A prominent response component at the driving frequency is noticeable.

Next, the rotor goes from a forward whirling phase to a bumping phase, when the drive rotation speed is increased. Bumping occurs when the rotor starts bouncing on and off the shell edge; the trajectories form sharp corners, which can be noted from the rotor trajectory shown in Figure 5(a). In Figure 5(b), the first peak represents the rotor in forward whirling followed by a bumping phase. During the bumping stage, the radial speed has a high amplitude compared to that during the forward whirling phase, as discernible from Figure 5(c). The normal direction displacement component of the rotor is not sinusoidal since bouncing occurs. Again, there is a discernible response component at the drive frequency in the frequency spectra of Figure 5(d).

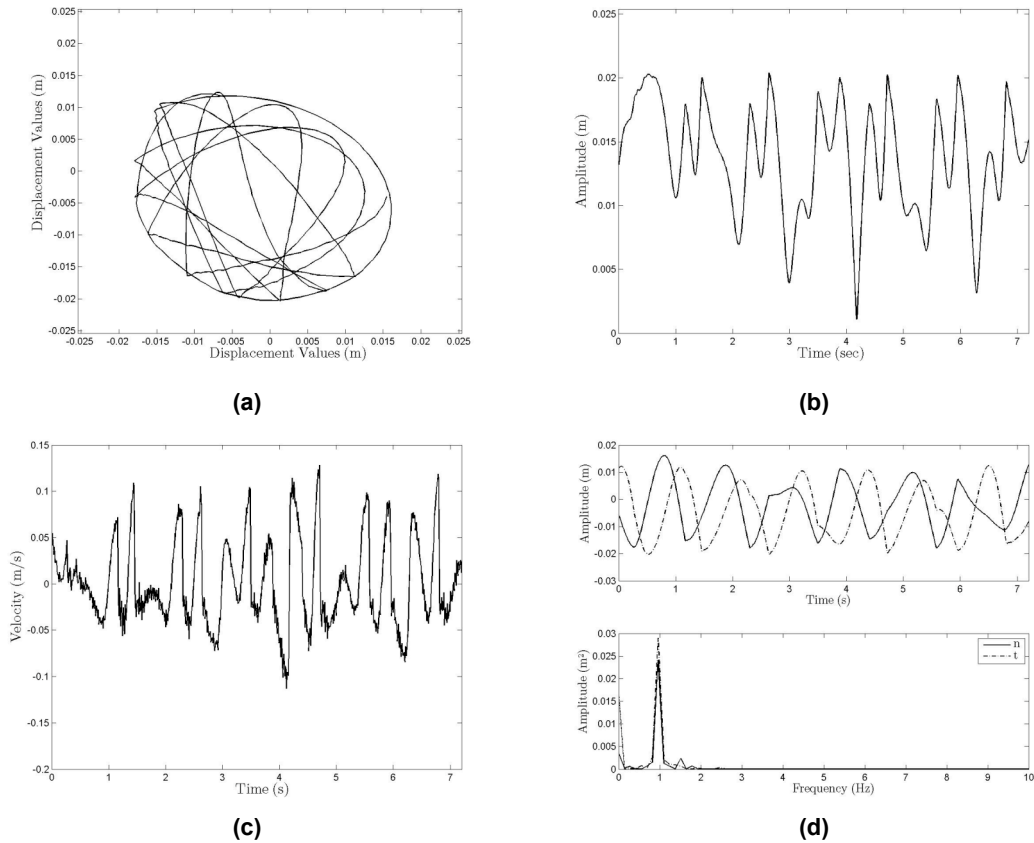


Figure 5. Rotor response for rotation speed of 55.6 rpm with rubber-rubber contact: (a) rotor trajectory, (b) radial displacement history, (c) variation of radial speed, and (d) normal and tangential displacement histories (top) and corresponding frequency spectrum (bottom).

In Figure 6(a), a rotor trajectory in a pure bumping phase is illustrated. In this stage, the rotor bumps periodically back and forth across the whole outer shell region, as shown in Figure 6(b). After an impact, the amplitude of the radial velocity experiences a jump, as seen from Figure 6(c). The frequency spectra of Figure 6(d) show two prominent peaks, with the first peak corresponding to the drive frequency.

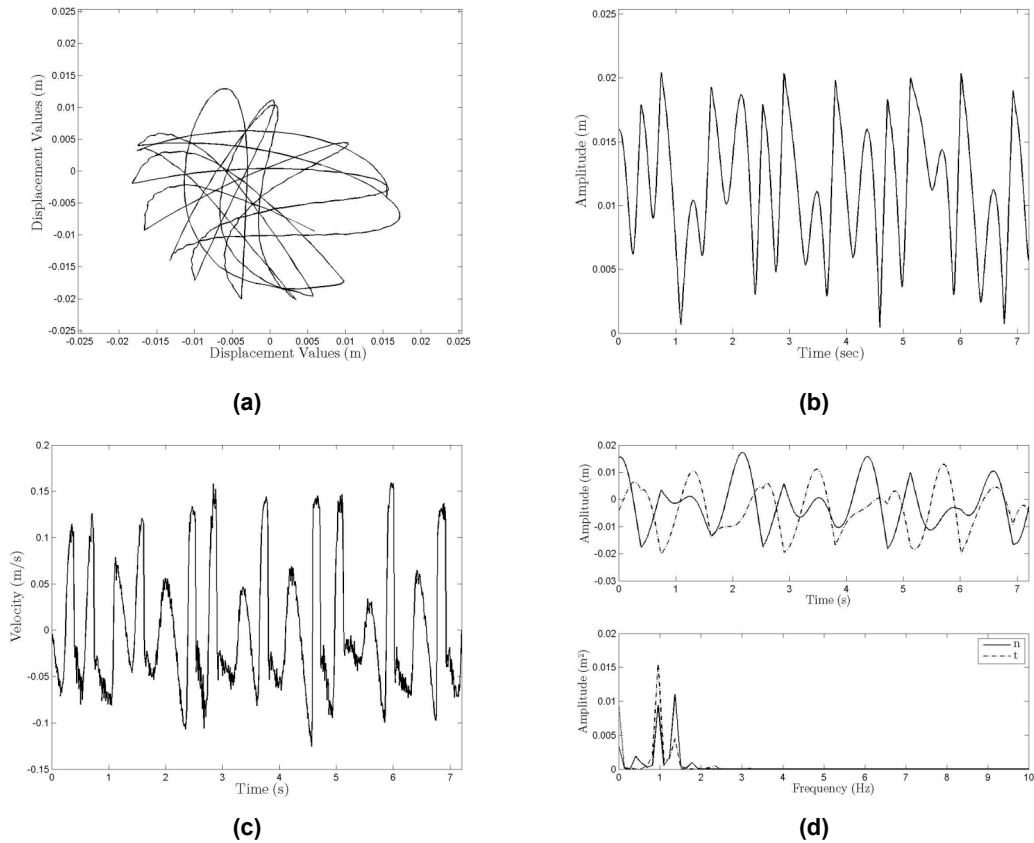


Figure 6. Rotor response for rotating speed of 55.6 rpm with rubber - rubber contact: (a) rotor trajectory, (b) radial displacement history, (c) radial velocity history, and (d) normal and tangential displacement histories (top) and corresponding frequency spectra (bottom).

Following the bumping phase, backward whirling can occur. The rotor trajectory of Figure 7(a) is similar to the one seen for forward whirling in Figure 4(a), but the dynamics are different. During backward whirling, the drill string is expected to experience considerable torsion strains and oscillations. One way to distinguish between forward whirling and backward whirling is on the basis of the radial displacement time history, such as that shown in Figure 7(b). Another means is to use the frequency spectra, such as those shown in Figure 7(d). During backward whirling, the response component frequency is higher than the excitation frequency; the ratio of the backward whirling frequency to excitation frequency is roughly determined by the rotor diameter and inner diameter of the shell [see, Vlajic, Liao, Karki, and Balachandran, 2011]. Backward whirling is important to avoid, as it can cause drill-string failures. In practice, this should be avoided.

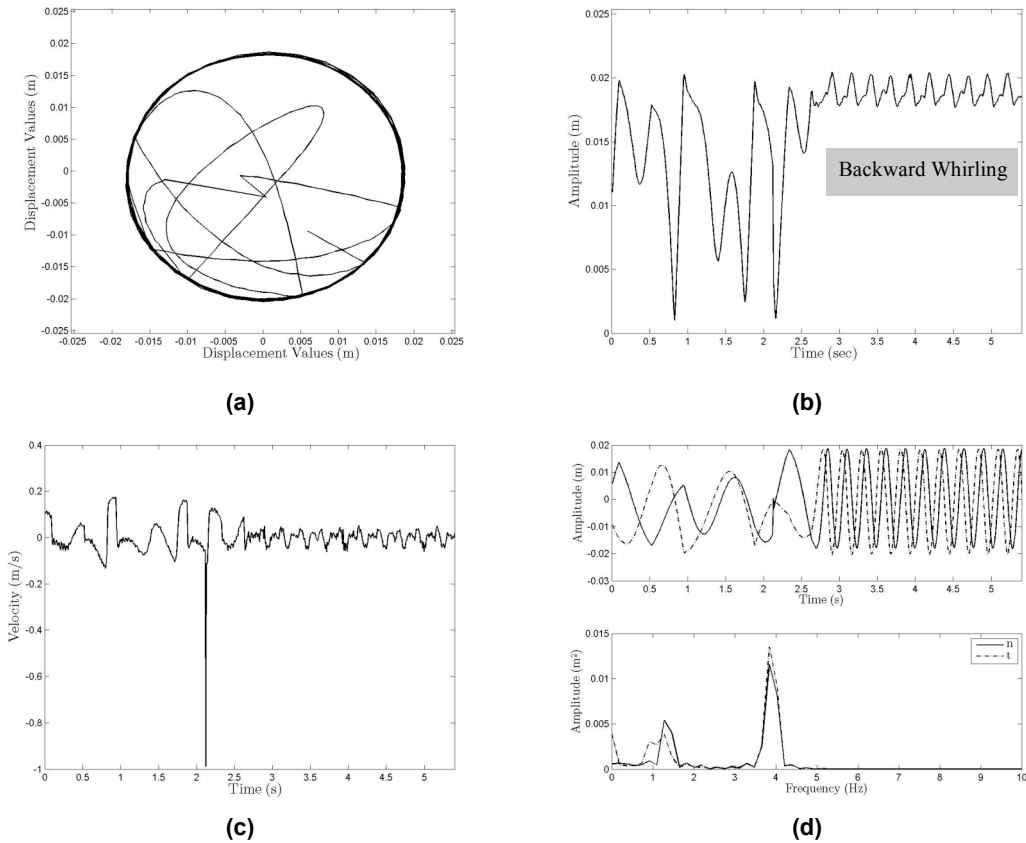


Figure 7. Rotor response for rotation speed of 55.6 rpm with rubber-rubber contact: (a) rotor trajectory, (b) radial displacement history, (c) radial velocity history, and (d) normal and tangential displacement histories (top) and corresponding frequency spectra (bottom).

2.2 Horizontal Drilling Studies

An experimental apparatus used to study horizontal and curved drill strings was outlined in the November 2010 report. Photographs of the horizontal drill string experiment are given in Figure 8. The contents of this section primarily focus on modeling efforts that can be used to predict the dynamics of drill strings that are not necessarily in a vertical orientation.

In previous drill-string models within this study, reduced-order models have primarily been used to predict the dynamics of vertical drill strings. These models have served as a tool to examine the interaction forces between the drill string and the borehole wall. As a result, researchers have been able to create a drill string-well bore force interaction model which is able to capture *stick-slip interactions*, which are thought to be one of the sources of torsion vibrations. Although the previous reduced-order model was able to capture certain dynamics of vertical drill strings, the model is not well-suited for studying horizontal and curved drill strings; therefore, a distributed-parameter model, or sometimes referred to as a continuous model, is necessary as a starting point.

Continuous models have a few advantages and disadvantages in comparison to lumped-parameter models. Some of the advantages are as follows. The curvature of the drill string used for horizontal drilling processes can readily be taken into account by using continuous models, as opposed to lumped-parameter models where an unbalanced mass is introduced in an attempt to capture inertia effects related to curvature. Further, lumped-parameter models can only be used

to study oscillations associated with a limited number of natural frequencies and modes of vibration. On the other hand, distributed-parameter models can be used to predict a much larger number of natural frequencies and mode shapes, which is theoretically infinite – yet, often times a pre-specified number of natural frequencies are selected in order to have a tractable problem. One of the main disadvantages is that lumped-parameter models are described by ordinary differential equations, whereas, continuous models are described by partial differential equations of motion, which often pose challenges in determining a numerical solution.

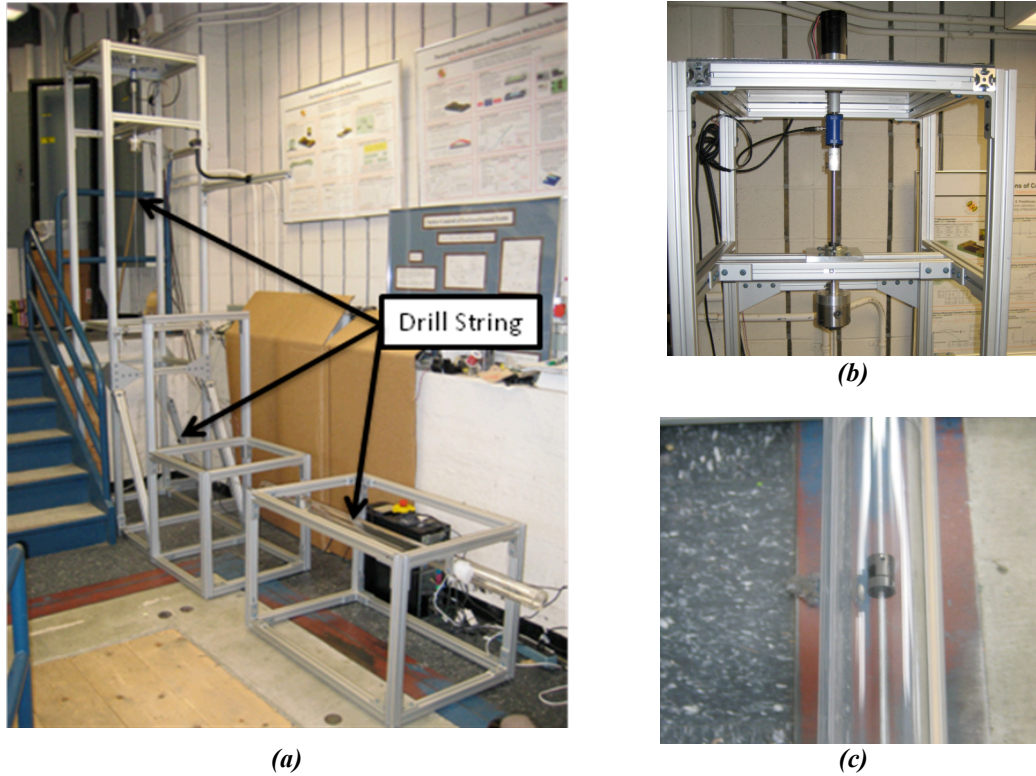


Figure 8. Horizontal drilling experimental apparatus: (a) drill string in horizontal configuration, (b) driving motor and torque sensor at string top, and (c) drill string and stabilizer in acrylic housing.

2.2.1 Development of a Distributed-Parameter Model

Motivated by the above discussion, a distributed parameter model is being developed to explain some of the dynamics observed in the horizontal drill string experimental apparatus. As a first step, it is useful to verify the predictive capabilities of the continuous model with data collected from the previous vertical drill string apparatus. The model used to generate the energy components and equations of motion is illustrated in Figure 9. It follows that the kinetic energy of the drill string, the lower disk (rotor), and unbalanced mass may be expressed as follows:

$$T_{shaft} = \frac{1}{2} \int_0^L \left[\rho A (\dot{u}^2 + \dot{v}^2 + \dot{w}^2) + \rho I (\dot{v}^2 + \dot{w}^2) + \rho I_o \dot{\beta}^2 + 2\rho I_o \dot{\beta} \dot{v} \dot{w}' \right] dx \quad (1)$$

$$T_{disk} = \frac{M}{2} \left[(\dot{u}^2 + \dot{v}^2 + \dot{w}^2) + \frac{I_D}{2} (\dot{v}^2 + \dot{w}^2) + \frac{I_{Do}}{2} (\dot{\beta}^2 + 2\dot{\beta} \dot{v} \dot{w}') \right] \Big|_{x=L} \quad (2)$$

$$T_{ubm} = \frac{m}{2} \left[(\dot{u}^2 + (\dot{v} - \dot{\beta} \sin \beta))^2 + (\dot{w} + \dot{\beta} \cos \beta)^2 \right] \Big|_{x=L} \quad (3)$$

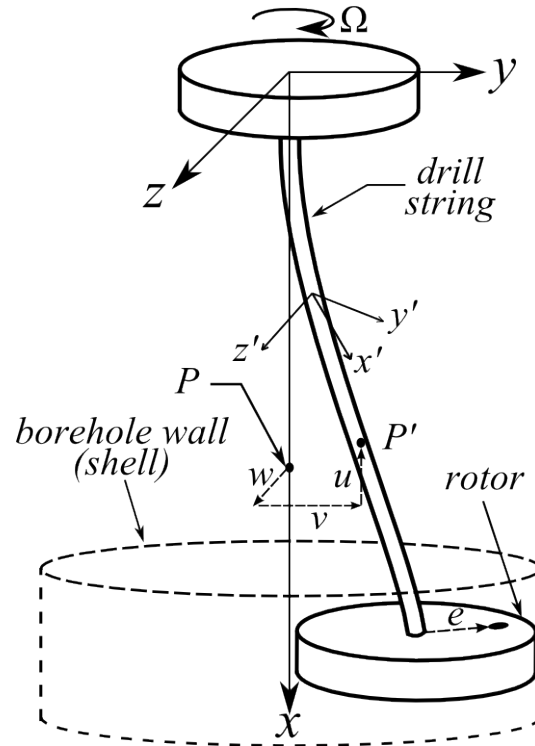


Figure 9. Model of a drill string section used to generate the equation of motion.

The operations $(\bullet)'$ and $(\dot{\bullet})$ denote the partial derivatives with respect to x and t , respectively. It should be noted that the kinetic of the upper disk is not considered, since it is assumed that the upper disk motion is prescribed at a constant velocity. From linear elasticity, the potential energy of the shaft structure may be expressed as

$$V = \frac{1}{2} \int_0^L \left[EAu'^2 + EI(v''^2 + w''^2) + GI_o\beta'^2 \right] dx \quad (4)$$

Assuming inextensibility, it follows that the partial derivative of u with respect to x may be given by

$$\frac{\partial u}{\partial x} \approx -\frac{1}{2} \left(\left(\frac{\partial v}{\partial x} \right)^2 + \left(\frac{\partial w}{\partial x} \right)^2 \right) \quad (5)$$

Additionally, the variation of the external work may be expressed as

$$\delta W_{ext} = \lambda \left[F_{tan} \frac{D_D}{2} \delta\beta + F_v \delta v + F_w \delta w \right] \quad (6)$$

Making use of Equations 1 through 6, neglecting the mass of the drill string as well as the axial inertia of the lower disk and unbalanced mass, and using a single-mode Galerkin projection with

shape functions selected to satisfy the linear boundary conditions, adding linear viscous damping, and finally invoking Hamilton's principle, the governing equations of motion are obtained as

$$c_1\ddot{V} + c_2\dot{V} + c_3\dot{W} + c_4V + c_5V^3 + c_6W^2V + c_7\ddot{\Theta}W + c_8\dot{\Theta}\dot{W} + c_9\dot{\Theta}\dot{V} - me\phi_\theta\phi_v\ddot{\Theta}\sin(\beta)\Big|_{x=L} - me\phi_v\dot{\beta}^2\cos(\beta)\Big|_{x=L} = F_v \quad (7)$$

$$d_1\ddot{W} + d_2\dot{W} + d_3W^3 + d_4WV^2 + d_5\dot{W} + me\phi_w\phi_\theta\ddot{\Theta}\cos(\beta)\Big|_{x=L} - me\phi_w\dot{\beta}^2\sin(\beta)\Big|_{x=L} = F_w \quad (8)$$

$$f_1\ddot{\Theta} + f_2(\ddot{V}W + \dot{V}\dot{W}) + f_3\Theta + f_4\dot{\Theta} - me\phi_\theta\ddot{W}\phi_w\cos(\beta)\Big|_{x=L} + me\dot{V}\phi_v\sin(\beta)\Big|_{x=L} = F_{tan} \frac{D_D}{2} \quad (9)$$

The constants c_j ($j = 1 \dots 10$), d_k ($k = 1 \dots 5$), and f_l ($l = 1 \dots 4$) are described in the work of Vlajic, Liao, Karki, and Balachandran (2011).

2.2.2 Force-Interaction Model

The authors would like to introduce a new force-interaction model in this section. Similar to earlier work in this study, the presence of contact is determined by the following definitions

$$\delta = \frac{1}{2}(D_S - D_D) \quad (10)$$

$$\rho = \sqrt{W^2 + V^2} \quad (11)$$

$$\lambda = \begin{cases} 0 & \text{for } \rho \leq \delta \\ 1 & \text{for } \rho > \delta \end{cases} \quad (12)$$

wherein the above definitions, D_D is the diameter of the rotor and D_S is the diameter of the shell. Furthermore, λ is the contact parameter, which is equal to zero when there is no contact, and equal to unity in the presence of contact. The forces that act upon the rotor are then governed by the following set of equations:

$$F_{normal} = \begin{cases} 0 & \text{for } \rho \leq \delta \\ K_c(\rho - \delta) & \text{for } \rho > \delta \end{cases} \quad (13)$$

$$\mu = \begin{cases} \left| \frac{V_{rel}}{V_{min}} \right| \mu_o & \text{for } |V_{rel}| < V_{min} \\ \mu_o & \text{for } |V_{rel}| \geq V_{min} \end{cases} \quad (14)$$

$$F_{tan} = -\mu \text{sign}(V_{rel}) F_{normal} \quad (15)$$

The difference between the previous force-interaction model used in earlier studies and the one presented here lies within Equations 14 and 15. In the previous work, the tangential force is discontinuous when the relative velocity is equal to zero. At that point, the tangential force is governed by a moment balance on the rotor, whereas in the current model, this force is piecewise continuous with respect to the relative velocity, and the tangential force is linearly interpolated when the relative velocity is in the region $-V_{\min}$ and V_{\min} , where V_{\min} is usually set to be a small value, which here is approximately 0.001m/s in the simulations. The advantage of the force-interaction model presented here is that it allows for *rolling*, which is defined when $\lambda = 1$ and when V_{rel} is close to zero. Under the condition of *perfect rolling*, the relative speed will equal zero. Feng and Zhang (2002) proposed a similar tangential force model with applications to a rotor and stator system. Although the current force-interaction model is able to account for rolling, it cannot consistently predict forward whirling in the presence of contact. The reason for this shortcoming is thought to originate from the perfectly elastic contact model given by equation **Error! Reference source not found.** In experiments and in practice, energy is lost when the rotor impacts the outer shell. In future work, consideration will be given to equation (4.13) to account for energy dissipation.

2.2.3 Comparisons between numerical and experimental results

Simulation results are compared to experimental results in Figure 10 for a drive speed of 80 rpm and an unbalanced mass of 87.1 g. In both the experiments and the simulations, the rotor makes several impacts with outer shell, and then starts to exhibit rolling behavior. The distinguishing difference between the experiments and the simulations is that the rotor makes several more impacts with the shell before rolling in the simulations. Again, this is likely a result of the perfectly elastic contact model given by Equation 13.

Next, the frequency response of the rotor lateral displacement is considered while exhibiting rolling motions. From experimental observations, it is known that during rolling, the lateral response frequency of the rotor is much higher than the driving frequency. Assuming perfect rolling (i.e., the relative speed is zero), and also that the torsion deformation and shell deflection are very small, the ratio between the driving frequency and lateral response frequency, as in Feng and Zhang (2002), is given by

$$\Omega_{whirl} = -\frac{D_D}{D_S - D_D} \Omega \quad (16)$$

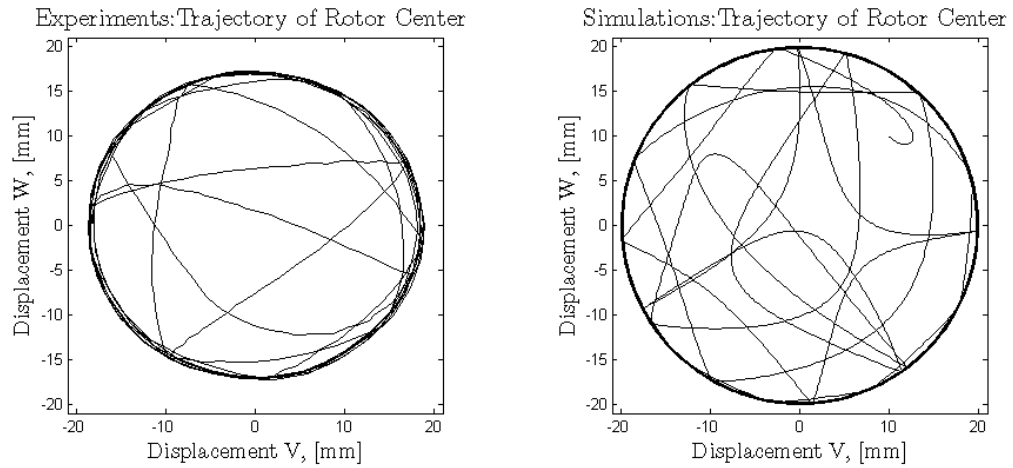


Figure 10. Comparison between experimental rotor trajectory and numerically determined rotor trajectory.

For the given experimental parameters, this ratio is approximately equal to 3.75. A graph showing comparisons amongst the predicted response frequency during rolling for the experiment, numerical simulation results, and Equation 16 prediction is presented in Figure 11. Discrepancies between the experimental values and the above derived equation are likely due to the violation of the no-slip condition and interspersed slipping and rolling motions.

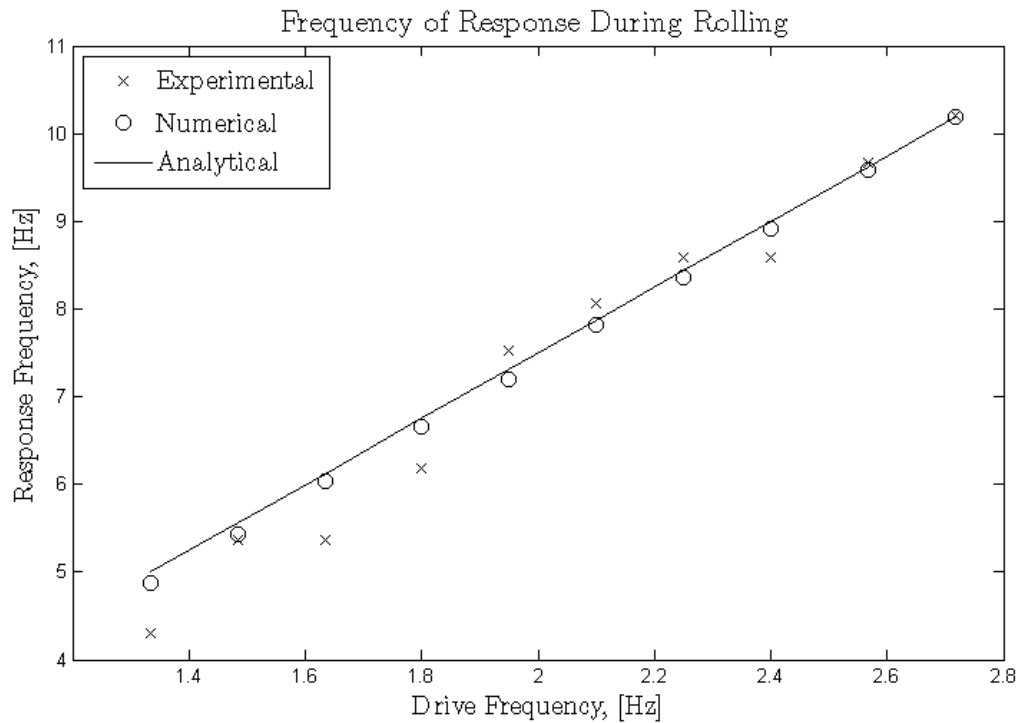


Figure 11. Experimental, numerical, and analytical results during rolling.

In this section, a novel distributed-parameter drill string model, including a force-interaction model has been presented. This model is able to capture dynamical features not captured in the previous modeling efforts, in particular, rolling. Additionally, the continuous model presented here may be modified to take into account initial curvature of a drill string used to bore dog legs and horizontal wells.

3. Planned activities for the next quarter

Rotor movements for different levels of rotating speed have been divided into phases such as center rotation, bumping/forward whirling and bumping/backward whirling. The characteristics of each stage provide guidelines for distinguishing the rotor movement, which can be applied for field study and for developing new control schemes. A distributed-parameter drill string model with compelling initial results has been presented as a first step towards studying the whole drill string in vertical or horizontal configurations.

After obtaining an understanding of the complex dynamics of a drill string in a vertical direction, the research is currently moving in the direction of horizontal drill strings with an experimental apparatus that has an aspect ratio close to that of “real” drill strings. Future reports are to contain findings and results pertaining to horizontal drilling studies.

Appendix

Approach

A combined analytical, numerical, and experimental approach is being pursued at the University of Maryland and the Petroleum Institute. Specifically, the drill string is being modeled as a reduced-order nonlinear dynamical system. Appropriate attention is also to be paid to the interactions with the environment. The experiments at UMD and PI are tailored to address specific aspects of the drill-string dynamics as well as complement each other. Actuator and sensor choices are also to be explored to determine how best to control the system dynamics, in particular, through the control rpm. The studies will be initiated with drill strings located on fixed platforms, and later extended to systems located on floating platforms

Three-Year Schedule

Phase II:

January 1, 2009 to December 31, 2009: Carry out quantitative comparisons between experimental results and predictions of reduced-order models for open-loop studies; understand stick-slip interactions and explore continuum mechanics based drill-string models for fixed platform environments; examine different configurations including horizontal drilling

January 1, 2010 to December 31, 2010: Construct control schemes; carry out experimental, analytical, and numerical studies; and identify appropriate schemes; study horizontal drilling configurations through experiments and analysis

January 1, 2011 to December 31, 2011: Continue horizontal drilling studies; carry out experiments, analysis, and numerical efforts and also examine drill-string operations in off-shore environments

January 1, 2012 to May 1, 2012: Compile results obtained for drill-string operations in vertical and horizontal configurations and provide guidelines for enhancing operations.

References

- [1] Akgun, F. 2004, "A Finite Element Model for Analyzing Horizontal Well BHA Behavior," J. of Petrol. Sci & Eng., Vol. 42, pp. 121-132.
- [2] Bednarz, S., 2004, "Design and Exploitation Problems of Drill Strings in Directional Drilling," Acta Montanistica Slovaca, Vol. 9, pp. 152-155.
- [3] Downton, G., 2009, "New Directions in Rotary Steerable Drilling", Oilfield Review, pp. 18-29.
- [4] Feng, Z., and Zhang, X., (2002). "Rubbing phenomena in rotor-stator contact". Chaos, Solitons & Fractals, 14(2), August, pp. 257-267.
- [5] Leine, R. I., van Campen, D. H., and Keultjes, W. J. G. (2002). "Stick-Slip Whirl Interaction in Drill String Dynamics," ASME Journal of Vibration and Acoustics, Vol. 124 (2), pp. 209-220.

- [6] Liao, C.-M., Balachandran, B., and Karkoub, M., (2009). "Drill-String Dynamics: Reduced Order Models," To appear in Proceedings of ASME IMECE 2009, Nov. 13-19 Lake Buena Vista, FL, USA, 2009; Paper No. IMECE2009-10339.
- [7] Melakhessou, H., Berlioz, A., and Ferraris, G. (2003). "A Nonlinear Well-Drillstring Interaction Model," *ASME Journal of Vibration and Acoustics*, Vol. 125, pp. 46-52.
- [8] Mihajlović, N., van Veggel, A. A., van de Wouw, N., and Nijmeijer, H. (2004) "Analysis of Friction-Induced Limit Cycling in an Experimental Drill-String System," *ASME Journal of Dynamic Systems, Measurement, and Control*, Vol. 126(4), pp. 709-720.
- [9] Mihajlović, N., van de Wouw, N., Rosielle, P.C.J.N., and Nijmeijer, H. (2007) "Interaction between torsional and lateral vibrations in flexible rotor systems with discontinuous friction," *Nonlinear Dynamics*, Vol. 50, pp. 679-699.
- [10] Nayfeh, A. H. and Balachandran, B. (1995). *Applied Nonlinear Dynamics: Analytical, Computational, and Experimental Methods*, Wiley, New York.
- [11] Spanos, P. D., Chevallier, A. M., Politis, N. P., and Payne, M. L. (2003). "Oil and Gas Well Drilling: A Vibrations Perspective," *Shock and Vibration Digest* Vol. 35(2), pp. 85-103.
- [12] Short, J. A. "Introduction to Directional and Horizontal Drilling " Pennwell Pub, 1993.
- [13] Singh, S. P. and Balachandran B. (2009). "Rolling Rub Translations of a Flexibility Connected Disk," pre-print.
- [14] Vlajic, N., Liao, C.-M., Karki, H., & Balachandran, B. (2011) "Stick-Slip and Whirl Motions of Drill Strings: Numerical and Experimental Studies," 2011 ASME IDETC MSNDC Conference, Washington, D.C., submitted for publication.

Studies on Mobile Sensor Platforms

UMD Investigators: Balakumar Balachandran, Nikil Chopra

GRAs: Rubyca Jaai

PI Investigator: Hamad Karki, Sai Cheong Fok

GRAs: Hesham Ishmail (ADNOC Fellow)

Start Date: April 2009

1. Objective/Abstract

Mobile sensor platforms can be employed in a variety of operations including environmental and structural health monitoring operations in harsh and remote environments. In the proposed work, cooperating sensor platforms are to be studied for potential use in oil storage tanks, which are periodically tested for corrosion, cracks, and leaks. These platforms are envisioned for estimating geometrical profile parameters, such as the tank bottom thickness. To this end, simultaneous localization and mapping (SLAM) algorithms (also known in the literature as concurrent mapping and localization (CML) algorithms) for cooperating sensor platforms operating in harsh environments are being investigated. While many solutions have been suggested for the single-agent SLAM problem, multi-agent SLAM is still a difficult problem from an analytical and practical perspective. The use of multiple agents allows for greater and faster coverage in the exploration and searching tasks and provides a certain degree of redundancy in the completion of tasks. Additionally, map merging using overlapping information from different agents can possibly compensate for sensor uncertainty (Dudek *et al.*, 1996).

The overall objective of this project will be to carry out a combined analytical, numerical, and experimental effort to develop mobile sensor platforms and appropriate simultaneous localization and mapping (SLAM) algorithms for cooperative sensor platforms to operate in a harsh environment. Research objectives are the following: i) develop SLAM algorithm-based platforms taking into account system constraints such as constrained communication, the type of sensors considered, allowable dynamics, and factors such as sensor failures and reliability of the considered sensors and ii) carry out experimental and supporting simulation studies by using mobile platform test platforms at the University of Maryland and the Petroleum Institute.

In this report, a decentralized SLAM algorithm is proposed to address the problem of multi-robot SLAM in a dynamic network by extending a multi-robot localization algorithm proposed by Leung *et al.* (2009). In Section 2, the basic issues in the SLAM problem are discussed, followed by the work schedule in Section 3. The main results are presented in Section 4, and future work is outlined in Section 5.

2. Summary of Results

The results presented in this report are the completed analytical and numerical results obtained for the decentralized SLAM algorithm presented in the previous report. Work done to complete the experimental setup is also summarized.

2.1 Decentralized simultaneous localization and mapping for multi-agent networks

The various definitions and theorems required for the decentralized SLAM algorithm are

presented. Some of the definitions can also be found in (Leung *et al.*, 2010) and are repeated below for completeness.

(1) *Assumptions and problem setup*

Let $|N|$ represent the total number of agents being used in the mapping task. The set N is assumed to contain unique identifiers for each agent (indices ranging from 1 to $|N|$). $N_{i,k}$ is the set of agents known to agent i at a specific time step k .

A general discrete dynamic model for the agents is assumed as

$$x_{i,k} = g(x_{i,k-1}, u_{i,k}, \varepsilon_k)$$

$$y_{i,k} = h(x_{i,k}, x_{j,k}, \delta_k) \quad (\forall j) \quad (d_k \leq r_{obs})$$

where for the time step k , $x_{i,k}$ is the pose of agent i ; $u_{i,k}$ represents the odometry information of agent i ; $g(\cdot)$ is the state transition function (with process noise ε_k); $y_{i,k}$ represents the range, bearing of a landmark or another agent with respect to agent i ; $h(\cdot)$ is the measurement function (with measurement noise, δ_k); d_k is the distance between agent i and the observed landmark or agent; and r_{obs} is the measurement range limit. Landmarks are assumed to be stationary. Hence, the state transition function for the landmark j is given by

$$x_{j,k} = x_{j,k-1}$$

Agents within the communication range r_{comm} of each other are able to exchange and relay information. The information broadcast between agents at every communication stage includes all the knowledge the agent possesses, such as its own state estimates, state estimates of the other agents and landmarks as well as odometry and measurement data.

$X_k = \{x_{i,k}, L_{i,k}\} \quad (\forall i \in N)$ represents the set of all agent states and the landmark locations at time step k ,

$X_{Q,k} = \{x_{i,k}, L_{i,k}\} \quad (\forall i \in Q) \quad (Q \subseteq N)$ represents the set of states at time step k for the agents and landmarks in some subset Q of N .

Similarly, odometry data are represented by sets U_k and $U_{Q,k}$, which are represented as

$$U_k = \{u_{i,k}\} \quad (\forall i \in N) \quad \text{and}$$

$$U_{Q,k} = \{u_{i,k}\} \quad (\forall i \in Q) \quad (Q \subseteq N)$$

The measurement data are represented as follows:

$Y_k = \{y_{i,k}^j\} \quad (\forall i, j) \quad (d_{i,k}^j \leq r_{obs})$ is the set of all measurements between agents as well as landmarks made at time step k .

These measurements are characterized by white zero-mean Gaussian noise processes with variances $\sigma(\rho)^2$, $\sigma(\theta^j)^2$, and $\sigma(\theta^i)^2$ respectively. The landmarks (map features) are assumed to be stationary and the measurements of these landmarks by the agents are represented by the set L_k (within the set X_k , as this is needed for the estimation of the landmark positions in SLAM). The set L_k contains all the measurements made by the agents with respect to the landmarks.

(2) *Use of the Markov property*

As in the case of the single agent SLAM problems, the true state of the system in the presence of noise is represented by a probability density function (pdf). In this case, the pdf represents estimates for all agent states (beliefs) and is calculated using the Markov property from odometry and measurement data.

$$bel(X_k) := p(X_k | bel(X_0), U_{1:k}, Y_{1:k}, L_{1:k}) = p(X_k | bel(X_{k-1}), U_k, Y_k, L_k)$$

Let the knowledge set $S_{i,k}$ consist of all odometry and measurement data, as well as the previous state estimates known to agent i at time k . At the initial time (for $k=0$), it is assumed that $S_{i,0} = \{bel(x_{i,0})\}$ which is the belief of the agents' own pose at the initial time. Before communicating with any agent, $S_{i,k}^-$ is the knowledge set after state transition and observations.

$$S_{i,k}^- = S_{i,k-1} \cup \{u_{i,k}, Y_{i,k}, L_{i,k}\}$$

As mentioned earlier, the agents broadcast the information that they individually possess, making their knowledge sets the same at the time of communication. Therefore,

$$S_{i,k} = S_{j,k} = S_{i,k}^- \cup S_{j,k}^-$$

The application of the Markov property makes the belief over the current state of a system independent of all its past states and, by eliminating the requirement for previous odometry and measurement data, reduces the memory requirements, as is the case with single-agent SLAM problems. The complication in the multi-agent setting in dynamic networks arises because communications between agents can occur at different times, leading to out-of-sequence measurements. Application of the Markov property without considering the out-of-sequence measurements may lead to sub-optimal state estimates as compared to centralized estimators. Furthermore, the odometry and measurement data that may be needed by other agents for state estimation will be discarded once the Markov property is applied to that particular agent. Another complication that should be avoided is the reuse of data after state estimations have been updated, as it can lead to over-confident state estimates. The decentralized algorithm solves these problems while providing state estimates equivalent to centralized estimators whenever possible. This is accomplished by monitoring the information flow in the network and determining the right time at which to apply the Markov property for each agent. Events known as checkpoints and partial checkpoints for the multi-agent system provide the necessary framework for solving the aforementioned problem.

Theorem 1. In order for every robot to calculate estimates equivalent to the centralized estimate, the knowledge set of each robot must contain odometry and measurement data from itself and from every other robot until the current time step (please refer to Jaai *et al.*, 2010 for proof).

It is therefore necessary to determine an appropriate time to apply the Markov property so that the elimination of data from the knowledge set of one mobile agent does not affect any other mobile agent in calculating the centralized estimate. This can be determined using events known as checkpoints and partial checkpoints, which are defined as follows.

Definition 1: A checkpoint $C(k_c, k_e)$ is an event that occurs at the checkpoint time k_c that first comes into existence at k_e , ($k_c < k_e$) in which the set of knowledge for each agent i contains for all j : i) the previous state estimate of agent j at some time step $k_{s,j} \leq k_c$ and ii) all the odometry and measurement data of agent j from time step $k_{s,j}$ to k_c .

Therefore, a checkpoint occurs at time step k_c when $S_{i,k_e} \supseteq S_{j,k_c} (\forall i, j)$.

A checkpoint exists if and only if every mobile agent can calculate the centralized estimate $bel(X_{k_c})$ at the time of occurrence of the checkpoint, k_c (please refer to Jaai *et al.*, 2010 for proof).

The knowledge set provides a practical method to check for the existence of a checkpoint by verifying if the knowledge set contains $u_{j:k_c}$ or $bel(X_{j:k_c}) \forall j \in N$. The Markov property can be applied at the checkpoint as at time k_c ; all the mobile agents can obtain the centralized estimate. Replacing data from the knowledge set up to time k_c by the centralized belief does not affect any of the other mobile agents. But, the existence of a checkpoint can only be determined using a global perspective by an external observer. In order for a mobile agent to determine when it can

apply the Markov property, a partial checkpoint is defined in terms of the local perspective.

Definition 2: A partial checkpoint $C_p(k_{c,i}, k_{e,i})$ is an event that occurs for agent i at time $k_{c,i}$ that first comes into existence at $k_{e,i}$, in which the set of knowledge for agent i contains for all j : i) the previous state estimate of agent j at some time step $k_{s,j} \leq k_{c,i}$ and ii) all the odometry and measurement data of agent j from time step $k_{s,j}$ to $k_{c,i}$.

A partial checkpoint therefore occurs for agent i at time step $k_{c,i}$ when $S_{i,k_e} \supseteq S_{j,k_c} (\forall j)$.

This means that when a partial checkpoint exists for every agent at a given time step k_c , then a checkpoint exists for the system. Partial checkpoints for each agent can occur at different times.

Theorem 3. A partial checkpoint exists for mobile agent i if and only if it can calculate the centralized estimate $bel(X_{k_c,i})$ at the time of occurrence of the checkpoint, k_c .

Proof: The proof of this statement can be carried out along the same lines as for Theorem 2 (please refer to Jaai *et al.*, 2010 for proof).

The existence of the partial checkpoint can be determined by verifying whether the knowledge set of mobile agent i at time k_e contains u_{j,k_c} or $bel(X_{j,k_c}) \forall j \in N$. This means that the mobile agent i considers only its local knowledge in detecting the existence of a partial checkpoint. Application of the Markov property when a partial checkpoint is detected by mobile agent i does not affect the occurrence of partial checkpoints for any of the other mobile agents (Leung *et al.*, 2010).

The centralized estimate is obtained by all mobile agents at the checkpoint time if each of the mobile agents apply the Markov property at partial checkpoints. In the case of decentralized localization, before mobile agents encounter each other (measure or communicate), they can be treated as independent systems, and the state estimates of the mobile agents are statistically independent.

Therefore, before accounting for measurements between the independent systems, the state estimate of the combined system can be obtained by using

$$bel(X_{Q1,k}; X_{Q2,k}) = bel(X_{Q1,k})bel(X_{Q2,k})$$

where $Q1$ and $Q2$ are two sets of mobile agents that have not encountered each other.

The property of statistical independence ensured that each mobile agent did not initially need to know the total number of mobile agents in the network in order to calculate the centralized estimates. This is not possible in decentralized SLAM, as any mobile agents that observe the same landmark cannot be considered independent of each other.

The possibility of mobile agents not measuring the same landmarks cannot be guaranteed, and the above equation cannot be used to combine the individual estimates. Therefore, in the case of decentralized SLAM, it is necessary for each mobile agent to initially know the number of mobile agents in the network in order to be able to obtain the centralized estimate.

Therefore, the centralized estimate can be obtained only if the number of mobile agents in the network is known to each mobile agent. Furthermore, detecting checkpoints and partial checkpoints also requires knowledge of the total number of mobile agents in the network.

Theorem 4: The existence of a checkpoint can be detected if and only if the number of mobile agents in the network is known (please refer to Jaai *et al.*, 2010 for proof).

Theorem 5: The existence of a partial checkpoint is detectable by mobile agent i if and only if the number of mobile agents in the network is known to mobile agent i .

Proof: The existence of a partial checkpoint $C_p(k_{c,i}, k_{e,i})$ is detected by verifying that the knowledge set of the mobile agent i contains u_{j,k_c} or $bel(X_{j,k_c}) \forall j \in N$.

$$S_{i,k_e,i} \supseteq \{u_{j,k_c}\} \text{ or } \{bel(X_{j,k_c})\} \forall j \in N$$

Therefore, in order to verify that the knowledge set of mobile agent i contains the odometry information or centralized estimate of every mobile agent, it is necessary for mobile agent i to know the total number of mobile agents $|N|$ in the network. In order to prove the converse, assume that the number of mobile agents is known by mobile agent i . Then, it is possible to detect a checkpoint by using the above equation.

By using the knowledge of the total number of mobile agents in the network, each mobile agent can thus detect the existence of partial checkpoints within the knowledge set and apply the Markov property. The mobile agents can obtain an estimate equivalent to the centralized belief when partial checkpoints occur at the same time for all mobile agents.

(3) Algorithm

The algorithm proposed in this section is implemented on every mobile agent at each time step to provide a decentralized SLAM solution to a dynamic network of mobile agents. At each time step, the inputs required for the algorithm are the current time, k ; odometry data $u_{i,k}$; measurement data, $Y_{i,k}$; knowledge set from the previous time step, $S_{i,k-1}$; and the knowledge sets of all mobile agents that are within communication range (r_{comm}) at the current time step k .

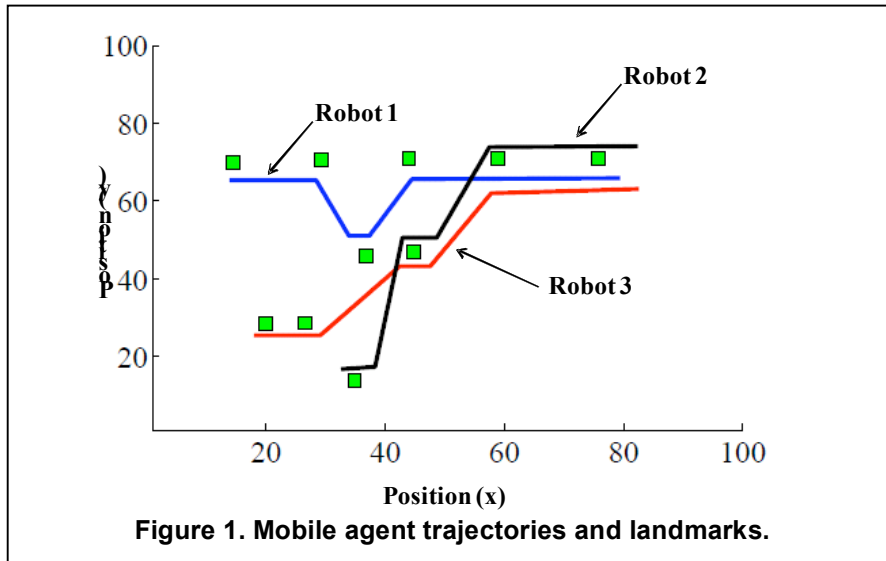
Algorithm: DecentralizedSLAM($k, u_{i,k}, Y_{i,k}, S_{i,k-1}, S_{j,k} \forall j, d_k^{i,j} < r_{comm}$)

- 1 $S_{i,k} \leftarrow S_{i,k-1} \cup \{u_{i,k}, Y_{i,k}\} \cup \{S_{j,k} (\forall j, d_k^{i,j} < r_{comm})\}$
- 2 $k_{c,i} \leftarrow \text{find largest } k_{c,i} \text{ such that } \{u_{j,k_c}\} \in S_{i,k} (\forall j \in N)$
- 3 $\bar{S}_{i,k_{c,i}} \leftarrow S_{i,k} - \{u_{j,k_r}, Y_{j,k_r}\} \forall k_r > k_{c,i}$
- 4 $bel^*(X_{k_{c,i}}) \leftarrow p(X_{k_{c,i}} | \bar{S}_{i,k_{c,i}})$
- 5 $S_{i,k} \leftarrow S_{i,k} \cup bel^*(X_{k_{c,i}})$
- 6 $S_{i,k} \leftarrow S_{i,k} - \{u_{j,k_r}, Y_{j,k_r}\} \forall k_r < k_c$
- 7 $bel(X_k) \leftarrow p(X_k | S_{i,k})$
- 8 return $\{bel(X_k), S_{i,k}\}$

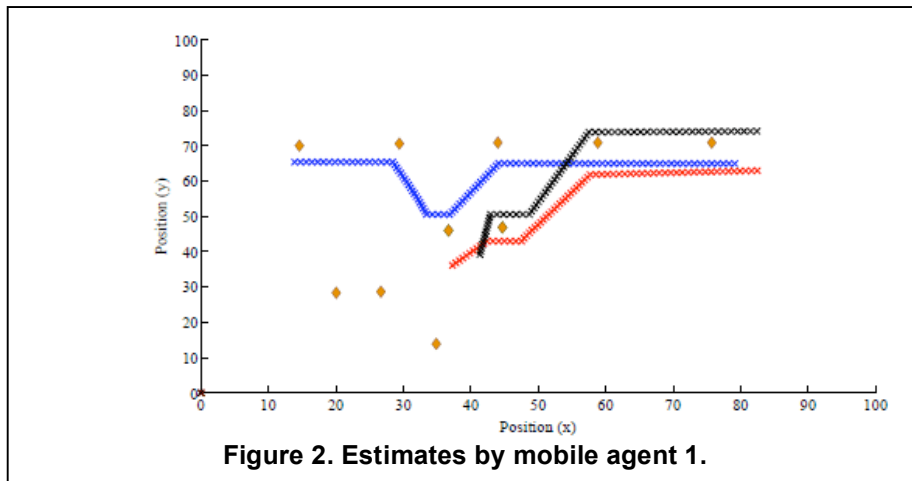
In line 1, the knowledge set of mobile agent i is updated with the current odometry and measurement data as well as with the knowledge sets of all the mobile agents within communication range. In line 2, the detection of the latest partial checkpoint is carried out by searching from the largest value of k_c for which $\{u_{j,k_c}\} \forall j \in N$ is contained in $S_{i,k}$. In line 3, the knowledge of mobile agent i up to the partial checkpoint is obtained for calculation of the centralized estimate in line 4. In lines 5 and 6, the knowledge set is updated with the current centralized belief (calculated in line 4) and by eliminating data from before the partial checkpoint. Finally, the current belief, which may not be equivalent to the centralized belief, is estimated and returned. The calculation of the current estimate is carried out using the last known velocity for mobile agents whose odometry data are not known since communication between them has not occurred.

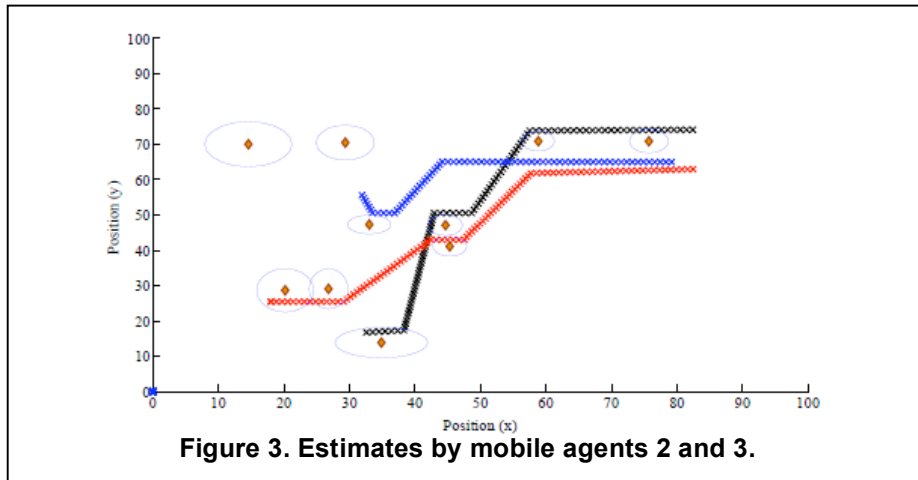
(4) Simulation results

In this section, results of simulation studies are conducted for the case of $N=3$ mobile agents with point landmarks. The communication range and the sensor measurement range were set at $25m^2$. The trajectory followed by the three mobile agents around the landmarks is shown in Figure 1.



The decentralized SLAM algorithm was then applied to each mobile agent at every time step, as explained in the previous section. The estimates of the three mobile agents' pose and the positions of the landmarks as calculated by mobile agent 1 are shown in Figure 2. The uncertainty estimates around the landmarks are those calculated by mobile agent 1 at the end of the trajectory. Similarly, estimates obtained by mobile agent 2 and 3 are also shown in Figure 3. In this case, since mobile agents 2 and 3 are always within communication range, the estimates calculated by them are the same. The estimates of mobile agent 1 pose remain zero until communication occurs. Therefore, the error in pose estimates grows between communications for those mobile agents that have not communicated.

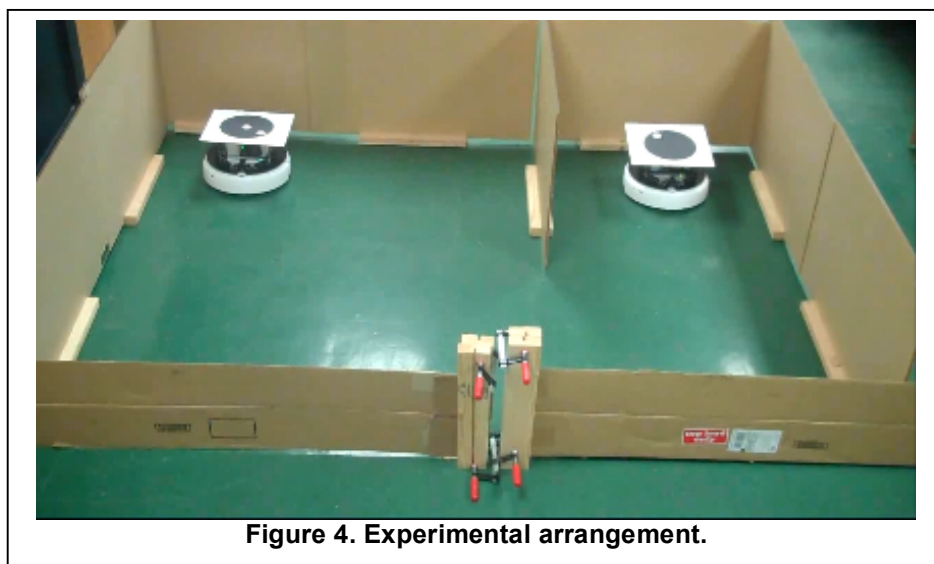




2.3 Experimental work

In order to test the decentralized multi-robot SLAM algorithm, it is necessary to set up mobile platforms that will contain the various sensors required for the localization and mapping as well as a feature-based environment.

Suitable ground-based mobile agents necessary to carry out the experimental measurements necessary for simultaneous localization and mapping have been acquired at the University of Maryland. The ground-based agent houses a microcontroller, two encoders to provide information regarding the location of the mobile agent, infrared sensors for obstacle avoidance, and ultrasonic sensors for range measurements of landmarks. The maze-like structure shown in the previous report was constructed from Plexiglass (see Figure 4). Cameras were added to the setup to provide ground truth data to compare the algorithm results for any experiments carried out with the actual positions of the mobile agents and the landmarks. The image processing code required for the cameras was written in Matlab. This code allows the user to calculate the positions of the mobile platforms over time as they traverse the maze collecting data.



The multi-robot decentralized SLAM algorithm presented in the report has been coded for experimental testing. Implementing the algorithm requires an additional data association algorithm to process the sensor data to extract features of the environment. The positions of

these features will then be estimated using the multi-robot decentralized SLAM algorithm. Data association algorithms will be investigated and added to the existing code in the next quarter.

3. Interactions

A paper entitled "Decentralized Simultaneous Localization and Mapping for Robotic Networks" was presented at the SPIE Smart Structures/NDE 2011.

4. Planned Project Activities for the Next Quarter

In order to test any SLAM algorithm experimentally, in particular with continuous landmarks such as walls, it is necessary to add data association algorithms and feature extraction algorithms that can identify and relate sensor readings to the walls or other features of the environment detected. The next goal is to add these algorithms so as to enable experimental testing of different SLAM algorithms. Once the data association algorithms have been added, the decentralized multi-agent SLAM algorithm presented previously in Section 4 will be tested with experiments. In addition, data association algorithms will also allow for extending the SLAM algorithms into other environments such as three-dimensional cylindrical pipes that are representative of oil pipelines.

Appendix

Approach

The basic aim of the SLAM algorithm is to make a mobile platform autonomous by providing the capability to navigate through an unknown environment from an initially unknown location. This is achieved by iteratively building a consistent map and by simultaneously determining its location within the map (Durrant-Whyte and Bailey, 2006). Therefore, simultaneous localization and mapping (SLAM) addresses the problem of using a mobile sensor platform to map an unknown environment while at the same time localizing itself relative to the growing map (Thrun, 2003). This ability is useful, in particular, in applications such as search and rescue operations, inspection and surveillance tasks, and exploration which require accurate localization within unknown environments. For example, in the inspection problem, by using SLAM techniques, the mobile sensor platform can determine locations of faults thereby providing an autonomous solution and reducing the need for external sensors to perform the same task.

In the SLAM problem, an agent or a mobile sensor platform uses relative sensing information between the agent and the surrounding environment in order to determine a map that constitutes the locations of landmarks or features in the surrounding environment as well as its own position within the map.

Well known solutions to the single robot SLAM problem include the use of extended Kalman filter (EKF) algorithm to estimate the position of landmarks and the pose (i.e., position and heading) of the mobile platform as Gaussian distributions or particle filters that allow for non-Gaussian representations or their combinations (known as FastSLAM) (Smith *et al.*, 1990, Montemerlo *et al.*, 2002). While many solutions for single robot SLAM exist, the problem of using multiple agents or robots for SLAM is still being studied in different settings. The use of multiple agents allows for greater coverage and speed in exploration and searching tasks, as well as providing a certain degree of redundancy in the completion of tasks. Additionally, in SLAM problems, map merging using overlapping information can help compensate for sensor uncertainty (Dudek *et al.*, 1996). Often studies in the area of multi-robot SLAM make use of certain simplifying assumptions regarding the communication network of the robots and the information that each robot possesses. Some examples of such assumptions are the network configuration of the mobile platforms remains static throughout, every mobile platform has knowledge of the initial positions of all the mobile platforms in the network. Some complications in the multi-robot SLAM problem include building maps when the relative initial positions of these systems are unknown, map merging when the overlap of the maps are unknown, complex correspondence problems related to the identification of individual systems, dealing with out of sequence information that is communicated to a mobile platform in a dynamic network.

Studies have been conducted to enable the map merging from multiple robots when the relative initial positions of the robots are unknown by calculating transformation matrices for the conversion from one robots reference frame to the other based on relative observations between the two (Howard, 2006, Zhou *et al.*, 2006). In this paper, a decentralized SLAM algorithm is proposed to address the problem of multi-robot SLAM in a dynamic network by extending earlier work by Leung *et al.* (2010). The work by Leung *et al.* provides a generalized algorithm for localization of multiple robots in a dynamic network. The decentralized localization algorithm does not require full network connectivity at all times and provides estimates that are equivalent to the centralized estimate whenever possible.

Three-Year Schedule

Phase II:

April 1, 2009 to December 31, 2009: Carry out analytical and numerical investigations into SLAM

algorithm based mobile platforms for representative geometrical profile measurements, and construction of experimental test platforms

January 1, 2010 to December 31, 2010: Continuation of analytical, experimental, and numerical efforts, with one of the focus areas to be development of appropriate communication and motion planning protocols for co-operative multi-agent platforms. Construction of experimental set-up for ground based mobile agents with attention to the environment

January 1, 2011 to December 31, 2011: Continuation of experimental and numerical studies and formulation of recommendations for appropriate sensor and mobile platform configurations for use in oil tanks and pipes.

January 1, 2012 to March 31, 2012: Continuation of experimental and numerical studies for proof of concept for appropriate sensor and mobile platform configurations for use in oil tanks and pipes.

References

- [1] Durrant-Whyte, H. and Bailey, T., 2006, "Simultaneous Localization and Mapping: Part I," IEEE Robotics & Automation Magazine, Vol.13, no.2, pp. 99-110, June.
- [2] Dudek, G., Jenkin, M., Milios, E. and Wilkes, D., "A Taxonomy for Multi-Agent Robotics," Autonomous Robots, 3(4), 1996.
- [3] Howard, A., "Multi-Robot Simultaneous Localization and Mapping using Particle Filters," International Journal of Robotics Research, 25(12), 1243–1256, 2006.
- [4] Leung, K, Barfoot, T.D., and Liu, H., "Decentralized Localization of Sparsely Communicating Robot Networks: A Centralized-Equivalent Approach," Robotics, IEEE Transactions on, 26(1), pp.62-77, 2010.
- [5] Montemerlo, M., Thrun, S., Koller, D., and Wegbreit, B., "FastSLAM: A Factored Solution to the Simultaneous Localization and Mapping Problem," in Proceedings of the AAAI National Conference on Artificial Intelligence, AAAI, (Edmonton, Canada), 2002.
- [6] Smith, R., Self, M. and Cheeseman, P., "Estimating Uncertain Spatial Relationships in Robotics", pp. 167-193, Springer-Verlag New York, Inc., New York, NY, USA, 1990.
- [7] Thrun, S., "Robotic Mapping: A Survey," in Exploring Artificial Intelligence in the New Millennium, G. Lakemeyer and B. Nebel, eds., pp. 1-35, Morgan Kaufmann Publishers Inc., San Francisco, CA, USA, 2003.
- [8] Thrun, S., Burgard, W., and Fox, D., 2006, "Probabilistic Robotics," MIT Press.
- [9] Zhou, X.S. and Roumeliotis, S.I., "Multi-Robot SLAM with Unknown Initial Correspondence: The Robot Rendezvous Case," In: 2006 IEEE/RSJ International Conference on Intelligent Robots and Systems, October 2006, pp. 1785–1792, 2006.
- [10] Jaai, R., Chopra, N., Balachandran, B., and Karki, H., "Decentralized Multi-robot Simultaneous Localization and Mapping," Proceedings of the SPIE Smart Structures/NDE 2011, San Diego, USA, 2011.

Development of a Probabilistic Model for Degradation Effects of Corrosion-Fatigue Cracking in Oil and Gas Pipelines

UMD Investigator: Mohammad Modarres

PI Investigators: Abdennour Seibi

GRA: Mohammad Nuhi

Start Date: Oct 2006

1. Objectives/Abstract

This research continues Phase I mechanistic modeling of the *corrosion-fatigue* phenomenon for applications to pipeline health, risk and reliability management. The objective of this study is to perform additional mechanistic-based probabilistic models derived from physics of failure studies and validate them using the state-of-the-art experimental laboratory being developed at the PI as part of the phase I of this study. Where possible, observed field data from ADNOC operating facilities will be used to supplement observations from the laboratory experiments based on the well-established Bayesian approach to mechanistic model updating and validation developed in Phase I. Uncertainties about the structure of the mechanistic models as well as their parameters will also be characterized and accounted for when such models are applied. The proposed models will allow the end users (e.g., maintenance analysts and Inspection crew) to integrate observed performance data from a wide range of pipelines and selected refinery equipment, such as pumps, compressors and motor-operated valves. Admitting the fact that modeling all degradation mechanisms would be a challenging undertaking, the proposed research will additionally address the following degradation phenomena related to the petroleum industry: creep, pitting corrosion, and stress cracking corrosion (SCC).

2. Deliverables for the Completed Quarter

The following tasks have been completed in the last three months:

- 3.1. Theoretical effort in support of model development
 - 3.1.1 Comparison of empirical model with literature (application of Akaike relation)
 - 3.1.2 Model uncertainty (Bayesian approach)
- 3.2 Experimental efforts in support of corrosion and creep model development.

3. Summary of Project Activities

3.1 Theoretical effort in support of model development

3.1.1 Comparison of the empirical model with literature (application of Akaike relation)

In order to show that the empirical model is an acceptable model for describing the creep-damage process, data from experimental and damage simulation of creep damage for duralumin alloy 2A12 (extracted from literature) [1] were used. The data was fitted by the empirical model and by several widely used models that have been used to predict creep damage and residual strength of different materials.

Models were compared with each other using Akaike's information criterion (AIC) [2-7]. The advantage of AIC over the maximum likelihood method is that it can compare different models at the same time to one another. The smaller the AIC value is, the better the chosen model is when

compared to others. This criterion is easy to use and contains the number of model parameters (variables) as part of its estimation.

In the special case of least squares estimation with normally distributed errors, AIC is described by [6]:

$$AIC = n \left[\ln \left(\frac{2\pi RSS}{n} \right) + 1 \right] + 2k, \quad \text{with } RSS = \sum_{i=1}^n e_i^2 \quad (1)$$

where e_i is the estimated residuals from the fitted models, n is number of data (observant), k is the number of model parameters (variables) and RSS is the residual sums of squares of the given data.

The following three creep-damage models: Kachanov–Rabotnov (K–R) creep-damage model [8-11], θ - projection model [12-17], and modified Theta-Omega model [8] were chosen.

- **Kachanov–Rabotnov (K–R) constitutive model**

$$\dot{\epsilon}_e = B \frac{(\sigma_e)^n}{(1-\omega)^m} \quad (2)$$

$$\dot{\omega} = D \frac{(\lambda\sigma_1 + (1-\lambda)\sigma_e)^\chi}{(1-\omega)^\phi} \quad (3)$$

where ϵ_e and σ_e are equivalent creep strain and stress. σ_1 is the maximum principal stress, ω is the damage variable which can be from 0 (no damage) to 1 (full damage). The terms D , B , n , ϕ , χ , and λ are material parameters which can be obtained from uniaxial tensile creep curves and the optimum method.

Experimental data and optimum fitted K-R creep curve for duralumin alloy 2A12 (by 2200N and 13mm² specimen cross section area) that were taken from the literature [1], are given in Figure 1.

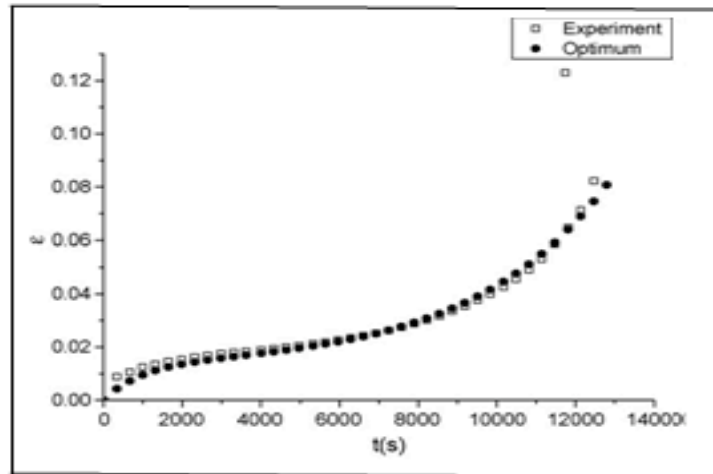


Figure 1. Comparison of optimum fitted curve based on K-R- model with the given experimental data.

The following three models were fitted to the above data.

- **Theta-projection model**

$$\varepsilon_c = \theta_1 \{1 - \exp(-\theta_2 t)\} + \theta_3 \{\exp(\theta_3 t) - 1\} \quad (4)$$

where t is the time, θ_1 , θ_2 , θ_3 , and θ_4 . are parameter constants determined by fitting the equation to experimental data.

- **Theta-omega model**

$$\varepsilon_c = X(1) \{1 - \exp(-X(2)t)\} + \left(\frac{-1}{X(3)}\right) \ln(1 - X(4)t) \quad (5)$$

where X(1), X(2), X(3) and X(4) are parameter constants characterizing creep curve shapes.

Proposed empirical model

We propose to use a power law model for the primary part of the creep curve; additionally, we use a combination of power law and exponential law to cover the secondary and tertiary parts of creep. The proposed combined parts can be written as:

$$\varepsilon_c = a t^n + c t^m \exp(p t) \quad (6)$$

where a, n, c, m and p are parameter constants describing the creep curve.

The results of this fitting (together with the experimental data) are given in Figure 2. Models were compared with each other by calculation of AIC values, and results are given in Table 1.

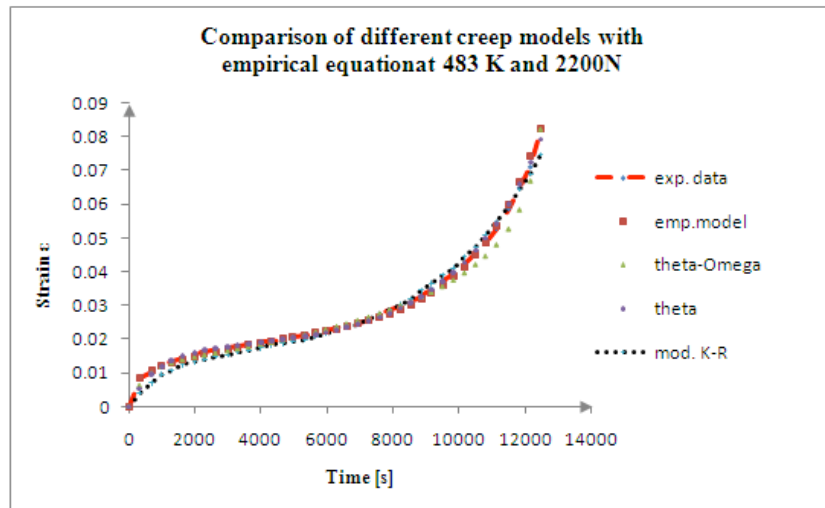


Figure 2. Comparison of different creep models with the given experimental data.

Table 1. AIC values from comparison of different creep models with the given experimental data

	Empirical-model	Theta-model	Theta-Omega-model	K-R-model
n	39	39	39	39
k	5	4	4	6
AIC	-432.3 <	-422 <	-363 <	-357

where n=number of observant (data), K= number of parameters in the fitted model, and AIC is values for different models.

As seen in Table 1, the AIC values can be ranked in ascending order as follows: empirical model, theta model, theta-omega model and the K-R model. This shows that the empirical model is an acceptable model for describing the creep-damage process. It should be mentioned that the K-R model had a higher number of parameters (variables) when compared to the other models, but according to the ranking the K-R model is the worst one.

3.1.2 Model uncertainty (Bayesian approach)

The model uncertainty approach was applied to compare the above models with the experimental strain data (extracted again from the literature for duralumin alloy 2A12, mentioned above [1]). In this approach Bayesian inference [18, 19] was used, and the 2.5% and 97.5% boundary confidence intervals were estimated to show how tight the confidence intervals were to the experimental data. The results are given in Figure 3.

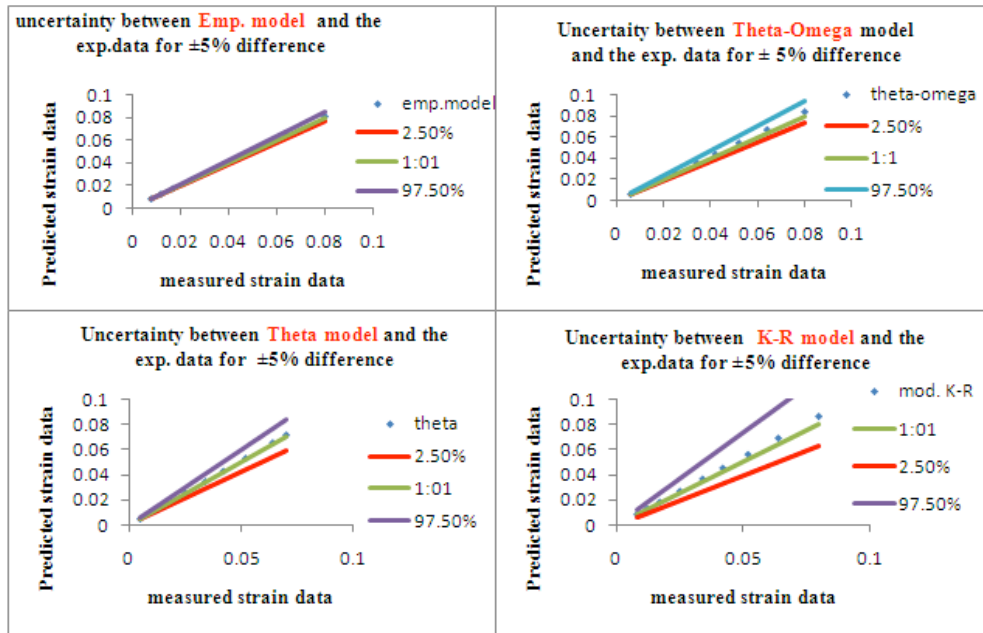


Figure 3. Comparison of different model data as predicted strain model data with the measured data.

It is clearly seen in Figure 2 that the empirical model is better than the other models. The uncertainty between the proposed empirical model and the experimental data was smaller than the other models with 95% confidence [18, 19].

3.2. Experimental effort in support of model development

Creep of materials is generally associated with time dependent plasticity of materials under a constant stress (below the yield stress of the material) at an elevated temperature, often greater than approximately $(0.4 \text{ to } 0.5) T_m$, where T_m is the absolute melting temperature. In the reported experiments two different materials were considered: Al 7075-T6 and X-70 carbon steel (both are used in oil refinery industry). First, creep experiments were done with Al-7075 samples because of its lower creep temperature requirement, and equipment reliability properties were checked under different load and displacement conditions at different temperatures. To estimate the amount of constant stress applied to the sample (for remaining in the elastic regime below the yield strength of the material), stress strain curve of these materials was used. The stress-strain curve for Al 7075 is given in Figure 4. In order to determine the appropriate displacement required for testing, stress vs. displacement curves were created as shown in Figure 5.

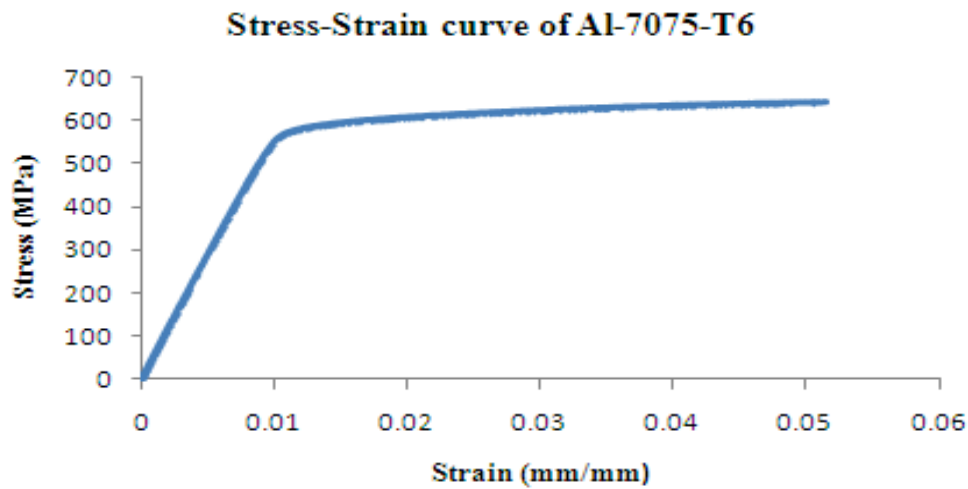


Figure 4. Stress- strain curve of Al-7075-T6 cladding alloy.

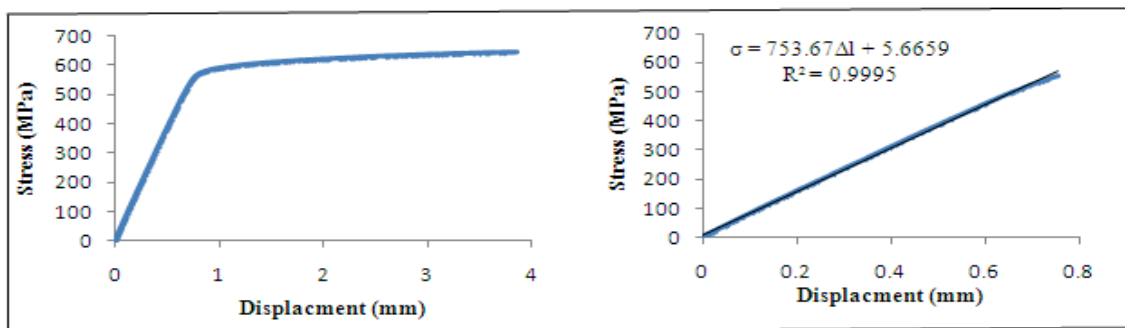


Figure 5. Stress-displacement curve for Al 7075-T6 (left), and stress-displacement curve for Al 7075-T6 (elastic region) (right).

Three different Al-7075-T6 samples were tested at different applied stresses of 100, 250, and 400 MPa, at 573 °K. The resulting displacement vs. time of these samples is given in Figure 6.

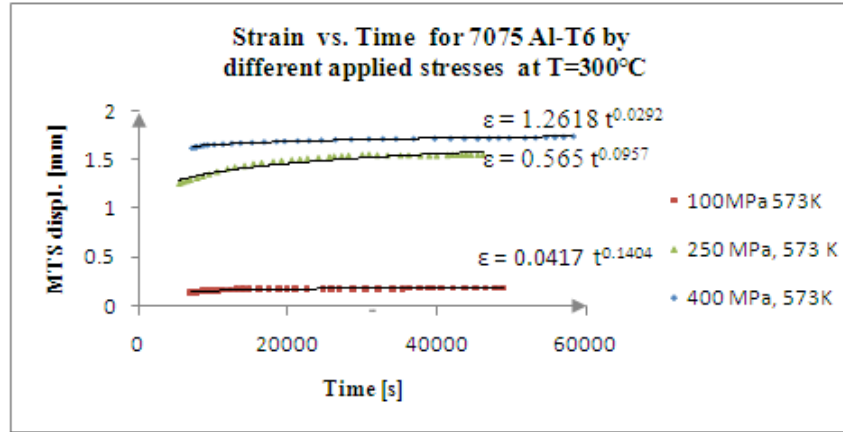


Figure 6. MTS displacement vs. time for different Al-7075-T5 alloys at different stresses.

The stress, σ , of the coefficient and exponent of the empirical Equation (6) for the primary part is given by the following relations and shown in numerical form in Figure 7:

$$a = \alpha \sigma^m \quad \text{and} \quad n = \beta \sigma + \gamma$$

where α , m , β , and γ are material parameters.

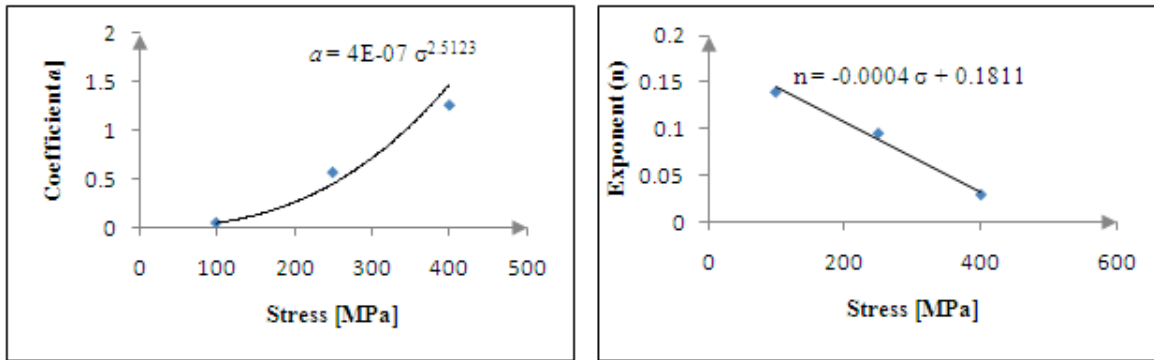


Figure 7. Stress dependency of coefficient, a (left), and exponent (right) of the creep equation.

So, the general form of the primary part of creep relation is:

$$\epsilon_c = \alpha \sigma^m t^{\alpha \sigma - \beta}$$

The stress dependency for the coefficients and time exponent are similar to the ones mentioned in previous reports.

In addition to these experiments two other Al 7075 samples were pulled at different displacement rates of 0.073 mm/hr and 0.0008 mm/hr to evaluate the Larson Miller relation [20]. The experimentally determined parameters will be compared to given literature values.

Creep experiments can be time consuming (a month to years); therefore, accelerated life testing was conducted on one sample. This sample was pulled until rupture by a constant force of 19,000 N (for average sample cross section of 10.25mm), while being kept at a temperature of 400 °C. This experiment should allow for the study of secondary and tertiary creep. The results of this creep experiment are shown in Figure 6 below.

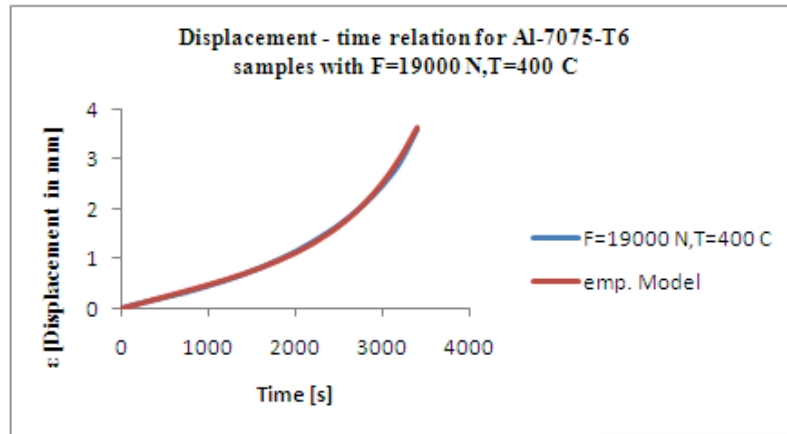


Figure 6. Displacement-time (creep curve) of Al-7075-T6 at 400°C.

The corresponding empirical relation for the creep curve shown above in Figure 6 has the following form:

$$\varepsilon = 0.000685 t^{1.939} + (1.695 \times 10^{-11}) t^{1.965} \exp(0.000795 t)$$

The temperature and stress dependencies of these parameters will be investigated.

Figure 7 shows the broken ductile sample (with the cup and cone form) after the creep experiment. The blurry effect of temperature on the Al-samples is clearly seen in the picture.



Figure 7. Broken ductile Al-7075-T6 samples (cup and cone form) after creep experiment at 400°C.

Creep experiments on dog bone X-70 carbon steel samples will be done in the near future and the results will be given in the next quarterly report.

4. Future work

The model verification and justification by performing creep experiments of Al 7075 dog-bone shaped specimens and X-70 carbon steel CT specimens will be the next phase of our study, followed by the statistical evaluation of the experimental data and nonlinear regression analysis by the Matlab program. Finally, we will compare our model with other empirical models according to AIC (Akaike Information Criterion) [2-7], and BIC (Bayesian Information Criterion) [21] with experimental data gathered for Al-7075-T6 and X70 carbon steel samples.

Near future plans:

1. Simulation and refinement of the stress and temperature dependency of creep parameters of mechanistic models (PoF models) for creep for Al-7075-T6 and X70 carbon steel samples will be performed. The related report will be submitted.
2. The corresponding simulation and statistical tool to help both model development and field applications will be done.
3. We are planning to realize Dr. Seibi's suggestion and design the related grips and extensometers. Material for making the appropriate grips is now available.

Appendix

Background

A number of deterministic models have been proposed to assess reliability and life-remaining assessment of pipelines. Among these models is the ASME B31G code, which is most widely used for the assessment of corroded pipelines. However, these models are highly conservative and lack the ability to estimate the true life of the pipelines and other equipment used in the oil industry. To address this shortcoming one needs to develop a best-estimate assessment of the life (to assess reliability and risk imposed) by these structures and equipment and assess the uncertainties surrounding such estimates. The proposed probabilistic mechanistic models, when fully developed, would integrate the physics of failure of some of the leading failure degradation mechanisms in the oil industry into the formal risk and reliability assessments. Such physical models will be validated using a state of the art reliability assessment laboratory (being developed at PI). Uncertainties about the model structures and parameters will also be quantified. Such models will incorporate inspection data (characterizing limited and uncertain evidences). The rate of degradation is influenced by many factors such as pipeline materials, process conditions, geometry and location. Based on these factors, a best estimate of the structure (pipeline) or equipment (primarily valves, pumps and compressors) service life (reliability and remaining life) is to be calculated and uncertainties associated with the service life quantified. This estimate would serve as a basis that guides decisions regarding maintenance and replacement practices.

Phase I of this research focused on developing a corrosion-fatigue model. It successfully proposed such a model and developed an advanced laboratory for testing this phenomenon at PI. The current research continues in the same line of research by investigating and developing additional degradation phenomena (SCC, pitting corrosion, and creep-fatigue) and integrates these phenomena with reliability and risk assessment through four different tasks. The long-term objective of this research is to develop a comprehensive library of probabilistic mechanistic models for all degradation phenomena pertinent to structures (piping, and pressure vessels) used in the oil industry.

Test Facilities

The test rig for this research exists at the University of Maryland. The rig is used to conduct experimental studies reflecting field conditions for model validation developed in EERC phase I & II. The equipment include MTS fatigue machine, heating furnace, corrosion test cells, autoclaves, multiphase flow loops, and testing machines for slow strain rate and crack growth testing. This activity also requires a complete line of monitoring equipment for evaluation of corrosion, scaling, and chemical treatment for field and laboratory. This test rig will be a useful tool for performing fatigue, corrosion, corrosion-fatigue, creep, and creep-fatigue, as well as teaching and possibly training field engineers from operating companies.

Two-Year Schedule

This project involves three distinct tasks. The first task is the development of the mechanistic models, development of a corresponding simulation tool to help both model development and field applications. The second task focuses on experimental activities to generate relevant data to validate the proposed models of Task 1. Finally, the third task involves the actual validation of the models proposed in Task 1 with the experimental results obtained in Task 2, including Bayesian estimation of the model parameters.

Task 1: Develop the best estimate mechanistic (physics of failure) empirical models for pitting corrosion, SCC, and fatigue-creep. The model development involves the following activities.

Task 1.1: Gather, review and select most promising physics of failure based methods and algorithms proposed in the literature.

- Literature surveys for creep and stress corrosion cracking (SCC) degradation mechanisms are almost completed and will be classified for finding the relevant models (100% done).

Task 1.2: Select, develop or adopt a detailed mechanistic model (one deterministic model for each phenomenon) that properly describes the degradation process.

- Development of the mechanistic models and of a corresponding simulation tool to help both model development and field applications after classifying the models and choosing the appropriate one should be done in the next future (85% complete).

Task 1.3: Develop a Monte-Carlo based mathematical simulation routine on Matlab depicting the detailed mechanistic model of each degradation phenomenon (far faster than real-time).

- This part was completed for the empirical model developed based on the works of the PI interns for pitting corrosion. After proposing the similar models for SCC and creep-fatigue, it will be repeated (80% completed).

Task 1.4: Based on the results of the simulation a simplified empirical model that best describes the results of simulation will be proposed. Such a model relates the degradation (e.g., depth of the pit or the crack growth rate) to applied loads such as pipeline internal pressure and chemical composition of the product inside the pipeline, as a function of time or cycle of load application.

- This part is completed for the pitting corrosion and corrosion-fatigue, but further work will be done for the other failure mechanisms (80% complete).

Task 2: A PoF reliability analysis laboratory has been designed and being developed at PI. The advanced corrosion-fatigue purchased by the PI that was installed at the University of Maryland (the Cortest Rig) has already been sent to Cortest to ship to PI.

Task 2.1: Completing the remaining corrosion-fatigue tests being conducted by Mr. Nuhi and Chookah. (100% Completed)

Task 2.2: Pitting Corrosion Experiments (develop test plan, prepare samples and the facility, perform the test, and evaluate the test results) (100% Completed).

Task 2.3 SCC Experiments (develop test plan, prepare samples and the facility, perform the test, and evaluate the test results). (Not started yet)

- This task will be done in the near future, but SCC specimen holders have already designed and made according to the recent patents and ASTM-Standard.

Task 2.4 Creep-Fatigue Experiments: The equipments and samples are completely ready (100% completed); the tests will be performed in future and the results will be evaluated.

- A small-scaled corrosion-fatigue (or creep) chamber has been designed (not as part of this project), made and tested for dog-bone specimens and checked its workability on the UMD MTS machines using an Aluminum alloy sample. Another more sophisticated one has been already designed and tested for CT-specimens and is tested. Moreover, another chamber has been made for long specimens.

- A heating chamber has been designed and tested for creep experiments.
- New dial gauges with stand are prepared and tested in an experiment.

Task 3: This task involves modification, advancement and use of the WinBugs' Bayesian formalism for model validation using experimental data and integration of the field data and information including sensor-based data (acoustics and/or optical) to update the empirical models and estimate the remaining life of oil pipelines and structures. (80% Complete)

- The WinBugs' Bayesian formalism for model estimation and validation was developed as part of M. Chookah's work. This formalism is being updated and new applications of the formalism have been performed using past experimental data and new data of corrosion and fatigue obtained since departure of Dr. Chookah. Further work with this software for integration the experimental data has already be done.

Schedule/Milestones/Deliverables

Tasks 1.1-1.3 (5/1/09-12/15/09); Task 1.4 (12/15/09-3/1/10); Task 2.1 (completed 7/1/09); Task 2.2 (7/1/09-12/15/09); Task 2.3 (12/15/09 – 6/1/10); Task 2.4 (6/1/10-2/1/11); Task 3 (12/15/09-3/15/11).

The Cortest rig was boxed and shipped to the Cortest Corporation to test and send to **PI**.

The project is on schedules and there is no issue or delay at this point.

Dr. Seibi was appointed as a Co-Advisor of Mr. Nuhi.

Visits

- Dr. A.Seibi visited UMD in July 2009
- Dr. A.Seibi visited UMD in July 2010
- Two PI students Abdullah Al Tamimi, and Mohammad Abu Dagah took parts at summer internship (2009).
- A PI student Taher Abu Seer took parts at summer internship (2010).
- Prof. Modarres attended the 1st Annual PI Partner Schools Research Workshop. The Petroleum Institute, Abu Dhabi, U.A.E. January 6-7, 2010.

Papers Published and prepared for publishing by the Team

- 1- M. Chookah, M. Nuhi, and M. Modarres, "Assessment of Integrity of Oil Pipelines Subject to Corrosion-Fatigue and Pitting Corrosion", presented by Prof. Modarres at the International Conference of Integrity- Reliability-Failure (IRF) in Porto, Portugal, July 20-24 2009. (The cost of the conference and associated travels was not covered by EERC)
- 2- M. Chookah, M. Nuhi, and M. Modarres, A. Seibi "A Probabilistic Physics of Failure Model for Prognostic Health Monitoring of Piping Subject to Pitting and Corrosion –Fatigue" is sent for publication to the "Journal of Reliability Engineering and System Safety".
- 3- A paper on "Development of a Database of Mechanistic Models of Failure for Application to Pipeline and Equipment Risk, Reliability and Health Management (Pitting Corrosion- Pit Depth and Density), prepared for publication at a conference. We are studying the possibility that the PI interns present the paper.
- 4- Abstract: "Reliability Analysis for Degradation Effects of Pitting Corrosion in Carbon Steel Pipes" is prepared and sent it to a conference in Italy. This paper is acceptance and after some correction, it will be sent back to ICM.
- 5- Abstract: "Classification of Creep Models for Metallic Materials – A Comparative Study and Suggestions for Improvements is being prepared for publication.

References

- [1] BinZhao, et.al."experiment and of creep damage for duralumin alloy 2A12, Materials Science and Engineering A513-514 (2009) 91-96
- [2] K.P.Burnham and D.R. Anderson, " Kullback-Leibler information as a basis for strong inference in ecological studies", www.uvm.edu/rsenr/vtcfwru/spreadsheets/abundance/.../k-linfo.pdf
- [3] A.W.F. Edwards, Likelihood, Cambridge University Press,1972
- [4] D.R.Anderson, "Model Based Inference in the Life Science, Springer ,2008
- [5] Akaike, Wikipedia
- [6] [3] K.P.Burnham and D.R. Anderson," Model selection and multimodel inference, A practical Information-theoretic Approach, Spriger,2002
- [7] www.chichen6.tcu.edu.tw/teaching/謝紹陽等_2nd_BIC-AIC.ppt –
- [8] J. Lin, Z.L. Kowalewski and J. Cao, *Int. J. Mech. Sci.* **47** (2005), pp. 1038–1058. [Article](#) | [PDF \(322 K\)](#) | [View Record in Scopus](#) | [Cited By in Scopus \(6\)](#)
- [9] L.M. Kachanov, *Izv. AN SSSR, OTN* **8** (1958), pp. 26–31.
- [10] L.M. Kachanov, *The Theory of Creep*, British Library, Boston Sp, Wetnerley (1960).
- [11] Y.N. Rabotnov, *Creep Problems in Structural Members*, Amsterdam, North-Holland (1969).
- [12] R. Huang, *Turbine Technol.* **43** (2001), pp. 9–13. [View Record in Scopus](#) | [Cited By in Scopus \(4\)](#)
- [13] R.W. Evans and B. Wilshire, *Creep of Metals and Alloys*, The Institute of Metals, London (1985).
- [14] R.W. Evans and B. Wilshire, *Introduction to Creep*, The Institute of Materials, London (1993).
- [15] H. Burt and B. Wilshire, *Metall. Mater. Trans. A* **35A** (2004), pp. 1691–1701. [Full Text via CrossRef](#) | [View Record in Scopus](#) | [Cited By in Scopus \(16\)](#)
- [16] [H. Burt and B. Wilshire, *Metall. Mater. Trans. A* **36A** (2005), pp. 1219–1227. [View Record in Scopus](#) | [Cited By in Scopus \(5\)](#)
- [17] Ling, Y.Y. Zheng and Y.J. You, *Int. J. Pressure Vessels Piping* **84** (2007), pp. 304–309. [Article](#) | [PDF \(339 K\)](#) | [View Record in Scopus](#) | [Cited By in Scopus \(8\)](#)
- [18] M. Azarkhail, V. Ontiveros, M. Modarres. "A Bayesian Framework for Model Uncertainty Consideration in Fire Simulation Codes." 17th International Conference on Nuclear Engineering, Brussels, 2009
- [19] M. Azarkhail and M. Modarres, "A Novel Bayesian Framework for Uncertainty Management in Physics-Based Reliability Models", ASME International Mechanical Engineering Congress and Exposition, November 11-15, Seattle, Washington, USA., 2007
- [20] D.Y.LEE, et.al. "High-temperature properties of dispersion-strengthened 7075-T6 aluminium alloy", *Journal of materials science letters* **16** (1977) 158-160
- [21] Bayesian information criterion, en.wikipedia.org/wiki/Bayesian_information_criterion